THE UNIVERSITY *of* EDINBURGH

Measurement of Local and Microscale Behaviour in Dense Suspensions of Silica

S C Brown

Doctor of Philosophy
The University of Edinburgh
May 2023

”Yet one grows flowers because they are lovely - not because one wishes them to live forever.”

Abstract

Dense suspensions, which are ubiquitous in modern industrial applications including mine tailings, chocolate and cosmetics, consist of solid particles suspended in a viscous fluid at high volume fractions. Such suspensions, given a high enough volume fraction, behave as if solid over short time-scales but flow otherwise. At lower volume fractions these suspensions shear thicken, where the fluid resists deformation as the stress deforming it increases. Despite their ubiquity, the physics behind their behaviour is not fully understood and contains many gaps. Recent advances in suspension rheology have shown that direct frictional contacts between suspended particles play a central role governing their complex rheology, and thus it is critical to understand how such contacts form. While these advances provide an analytical mean field model for the bulk, steady-state flow of shear thickening suspensions, the understanding of time-dependent flow and local dynamics remains less developed.

In this thesis I present work which sheds light on some of the remaining open questions by linking particle interactions and the formation of frictional contacts, quantifying critical strain- and time-scales in unsteady time-dependent flow, and highlighting unexpected pitfalls in experimental techniques used by others to characterise local fluctuations.

Firstly, I investigate the steady state rheology of charge-stabilised silica suspensions, varying both the particle interactions (through the ionic strength of the suspending fluid) and particle size. I find a regime where the thickening onset stress scales inversely with the particle size, $\sigma^* \propto 1/R$, indicating a critical force that must be overcome to initiate frictional contact $F^* \propto R$. This scaling is consistent with the particle interactions obeying the Derjaguin approximation, but differs from previous results with sterically-stabilised particles. Such a result suggests that the DLVO theory breaks down at these small separations. Interestingly, this scaling breaks down at high ionic strengths, indicating a

breakdown of the Derjaguin approximation in this regime. Varying the fluid composition, I also examine how the thickening changes as I continuously transition from a charge-stabilised to a sterically-stabilised system.

Next I consider time-dependent flows. Building on previous work looking at shear rate oscillations in cornstarch suspensions (Richards et al. 2019), I apply the same proposed time-dependant model to oscillations in silica suspensions. I show that this proposed model successfully captures key features of the oscillation dynamics in the two disparate systems, in once case a sterically-stabilised system (cornstarch), and the other charge-stabilised (silica). Furthermore I show that the formation of contacts in $R = 2\,\mu\text{m}$ shear thickening silica is related to two strain-scales $\gamma_0 = 0.110(5)$ and $\gamma_1 = 0.61(1)$, found by fitting a double exponential curve, this compares to shear thickening cornstarch suspensions whose startup which can be well fit with a single exponential with strain-scale $\gamma_0 \approx 0.12$. Using model fits to the frequency of the shear rate oscillations a further time-scale t_r governing the relaxation to the steady-state was found for the silica suspensions. We find an order of magnitude shorter relaxation time in silica ($t_r \approx 0.03\,\text{s}$) compared to cornstarch ($t_r \approx 0.2\,\text{s}$), which might be a result of the significant differences in the particle shape, and stiffness. These results therefore help guide and narrow the search for the underlying micro-physics controlling time-dependent flows.

Finally I use a novel, recently developed measurement technique know as boundary stress microscopy to measure local stress fluctuations in suspensions during shear thickening. This method, which relies on imaging the deformation of an elastic substrate, has been previously employed by other groups. However, I show that this technique has an overlooked sensitivity to small plate misalignments, particularly when using the standard cone-plate tool geometry. I also qualitatively compare my boundary stress measurements for silica in glycerol/water suspensions to previous results of the same system and see the same local stress fluctuations below ϕ_M. We suggest that these fluctuations are related to the misalignment, due to the coupling of some of the fluctuations with the rheometer tool rotation rate.

Lay Abstract

A suspension is a system consisting of many solid particles mixed with a liquid. Suspensions are commonplace, examples include; toothpaste, cement, and even milk. When we say solid particles, here and throughout this work, we mean solid object which are on the edge of being visible to the human eye, but are significantly larger than the molecules of the liquid they are mixed with. An example very relevant to this work is a mixture of cornstarch (the solid particles) and water (the liquid). The cornstarch is a powder, with particles that can just about be individually distinguished by the naked eye. The water appears and behaves as a continuous medium, and it is impossible for the human eye to see the single molecules.

There are many different possible suspensions depending on the materials used and the ratios at which they are mixed. These different suspensions show different behaviours. In this work we focus on 'dense' suspensions, where the ratio of solid particles to the liquid is quite high (greater than 30% of the total volume). When cornstarch and water are mixed together at a ratio of 2:1 by weight they form a dense suspension. This mixture flows like a liquid, but can also be pushed against and resist motion like a solid

Current understanding of dense suspensions is that the liquid-solid behaviour is a result of the particles in the suspension moving into and out of contact depending on the external force applied. If we consider a powder like dry cornstarch, it does not behave just like a liquid, you may need to shake it to dislodge particles and pour it. Similarly if the particles were consistently separated, say by the presence of a thin layer of liquid between them, they would easily flow past one another. If some force squeezed this inter-particle layer out of the way the system would be like a powder again and would no longer flow as easily.

In this work we attempt to expand the understanding of dense suspensions

through experiment. This work tries to better understand several areas of the science around dense suspensions, these are; the forces involved in keeping the particles separated when in suspension, how quickly the particles can be pushed together and how quickly they separate, and validity of a novel experimental technique which could be used to measure forces with these suspensions at microscopic scales.

Declaration

I declare that this thesis was composed by myself, that the work contained herein is my own except where explicitly stated otherwise in the text, and that this work has not been submitted for any other degree or professional qualification except as specified.

(S C Brown, May 2023)

Acknowledgements

I would like to thank everyone who made this thesis possible. Firstly I would like to thank my supervisors John Royer and Wilson Poon for invaluable help with experimental problems and my scientific thinking. Secondly, a great thanks to my parents for encouraging me to keep going during a difficult period near the start of my PhD. Thank you James Richards for many enlightening conversations which have helped me better understand parts of my project.

It would be impossible not to thank my flatmates Veronica and Marie for many conversations and adventures, and all my other friends who have suffered through various stages of their studies alongside me. A big thanks to Holly for the many adventures we shared exploring Scotland on wheel and on foot. Thank you to my close friends in physics Elle, Joe, Leo, Martina and Jonathan, whose friendship although more recent than others has made the many painful months of writing my PhD significantly more bearable.

Finally, I would like to gratefully acknowledge the funding of my PhD studies by the EPSRC Centre for Doctoral Training in Soft Matter and Functional Interfaces

Contents

List of Figures

List of Tables

Chapter 1

Overview

Particles suspended in fluid are so commonplace as to be almost mundane, everyone has experienced them and understands their behaviour at some level. From high volume fraction pastes, which flow under enough force but can hold their shape; to paints, which can be easily spread onto surfaces but do not run when there, suspensions exhibit a wide range of behaviours. Understanding these fluids has clear benefits to industry, and can help to optimize and improve the manufacturing and performance of their products.

On a more fundamental level, people are also fascinated by the odd behaviour that results in these systems. The easily observable Non-Newtonian behaviour of shear thickening suspensions such as cornstarch-in-water, which is commonly used in science outreach, blurs the seemingly fundamental boundary between solid and fluid. Despite having intrigued so many people these materials are not fully understood, and within this thesis we add to the fundamental understanding of model shear thickening suspensions.

In chapter 2 we discuss the scientific background of colloids and suspensions, discussing in detail the nature of interactions between particles in suspensions. Recent advances in suspension rheology are discussed and open questions in current understanding are highlighted. In chapter 3, the materials and methods used throughout this work are outlined, with special attention given to how shear thickening samples were prepared.

There are three distinct results chapters. Chapter 4 focuses on the effect of particle size on suspensions behaviour and shows that one can use bulk rheology

to probe the particle-particle interactions in dense suspensions. In chapter 5 we look at how we can use the time-dependant behaviour observed in dense suspensions to measure intrinsic strain and time scales in suspensions. In chapter 6 we discuss a novel measurement technique, boundary stress microscopy (BSM), which has been used to measure local stresses in dense suspensions, and show that measurements taken using BSM are very sensitive to plate misalignment. Finally in chapter 7 we bring together and present the main results of this thesis.

Chapter 2

Suspension Rheology

Rheology is the study how materials flow and deform under an applied force. It is used to study the behaviour of soft materials; these materials often blur the boundary between solids and liquids. Some soft materials flow less easily as the force making them flow increases, whereas others appear solid until a minimum force is applied, and then flow plastically. Soft materials have inherent energy scales close to room temperature meaning they are often dominated by entropic effects, and therefore the rearrangement of local and global structures determines their behaviour. The constitutive relations between the force and the shear rate/strain (motion) of these soft materials are used to model the materials' flow. Ultimately the constitutive relation of a material can be linked to the behaviour of its constituent parts (fluid, particles, surfactants etc.).

Suspensions are materials comprised of solid particles suspended in some fluid. Understanding a single solid particle suspended in a fluid is relatively simple (assuming low speeds), but when we increase the number density of the particles in the fluid the behaviour becomes considerably more complex. Cornstarch-in-water suspensions are an example commonly used as part of physics outreach; they flow when poured, but at high enough particle concentration they become solid-like when a strong or sudden force is applied. In general, suspensions can show a wide range of rheological behaviours, which are often dependant on the size and interactions of the suspended particles.

Many suspensions used within industry exhibit complex behaviour, these include cement[29, 30], chocolate[31], and toothpaste [32, 33]. Although it is often possible to extract simple metrics using rheology, any scientific study of these

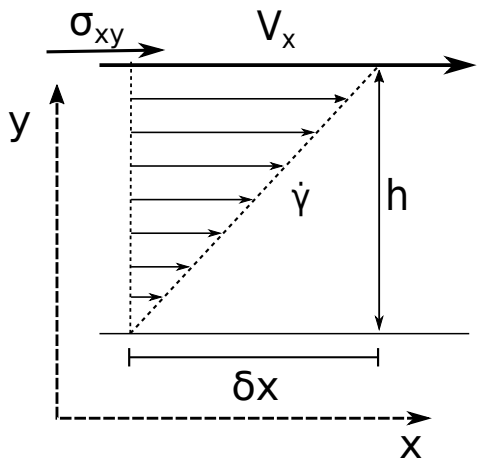

Figure 2.1 A 2D Schematic of a sheared material. V_x is the speed of the top surface relative to the bottom surface, and σ_x is the force per unit area applied parallel to the top surface.

systems requires a deeper understanding of rheology to extract meaningful results. Unfortunately the rich rheology of these suspensions often translates into difficulties in processing. As such, being able to better understand, and therefore control, the behaviour of these fluids is important to industry. Despite the ubiquity of suspensions, we have only recently developed physics-based rheological models capable of capturing their complex behaviour.

In this chapter we will introduce rheological terms and concepts necessary for understanding the work discussed within the thesis. We will explain the current understanding of shear thickening and then go on to discuss recent work, highlighting areas where understanding is still lacking. These later sections will discuss the effects of local particle dynamics on bulk rheology, as well as looking at local and time dependent behaviour in shear thickening suspensions.

2.1 Basics of Rheology

We begin by considering the behaviour of a material under simple shear, as illustrated in figure 2.1. The shear strain γ is the ratio between the lateral displacement along the shear axis δx and the height h,

$$\gamma = \frac{\delta x}{h}. \tag{2.1}$$

The shear rate is generally given by the velocity gradient, which for the case of the simple shear considered is constant across the sheared material

$$\dot{\gamma} = \frac{\mathrm{d}\gamma}{\mathrm{d}t} = \frac{V_x}{h}, \tag{2.2}$$

independent of the height y, where V_x is the velocity of the top surface $y = h$.

Since rheology generally concerns the resistance of a material to deformation, we must consider the forces required to drive such a shear flow. If we imagine the simple shear sketched in figure 2.1 being driven by pushing a plate with contact area A and force F along the flow direction, the material reaction defines the shear stress $\sigma = F/A$. A complete description of the stress state of a material actually involves the stress tensor σ_{ij} (with components σ_{ij} where $i \neq j$ describing the shear stresses and the components σ_{ij} where $i = j$ termed normal stresses). However when describing materials under simple shear we are primarily concerned with the xy component, and so simply denote $\sigma = \sigma_{xy} = \sigma_{yx}$ throughout the remainder of this thesis unless otherwise specified.

For a purely elastic solid the shear strain γ is related to the applied stress σ by the shear modulus of the solid G:

$$\sigma = G\gamma. \tag{2.3}$$

For a Hookean solid, G is constant for all values of γ and σ. Similarly for a purely viscous fluid the shear rate $\dot{\gamma}$, is related to the applied shear stress σ by the viscosity of the fluid η:

$$\sigma = \eta\dot{\gamma}. \tag{2.4}$$

For a Newtonian fluid, η is a constant for all values of $\dot{\gamma}$ and σ. Complex fluids can exhibit a wide range of behaviours, and within this work we will consider complex fluids which appear to show variation in η with σ, $\dot{\gamma}$, and time. Complex fluids can also be viscoelastic, exhibiting both viscous and elastic behaviour depending on the nature of the applied deformation or stress.

2.2 Suspensions and Particle Interactions

In this section we will discuss different particle interactions and their effect on the rheology of particulate suspensions. To begin we will consider the suspending

fluid, and simplifying assumptions about its behaviour. We will then go on to discuss idealised models of non-Brownian and then Brownian hard sphere systems, before introducing additional finite-ranged interactions (e.g. van der Waals and electrostatic forces).

2.2.1 The Suspending Fluid

First we consider the the behaviour of the suspending fluid. The flows of Newtonian fluids are governed by the Navier-Stokes equations which considering an incompressible fluid

$$\nabla \cdot \mathbf{u} = 0, \tag{2.5}$$

here $\mathbf{u}$ is the velocity field of the fluid. Conservation of momentum in the fluid is described by

$$\rho \left[\frac{\partial \mathbf{u}}{\partial t} + (\mathbf{u} \cdot \nabla)\mathbf{u} \right] = \mathbf{f} + \nabla \cdot \sigma^a, \tag{2.6}$$

here ρ is the fluid density, (f) is the body force per unit volume (usually just gravity for fluids), and σ^a is the symmetric stress tensor (which includes the pressure). For many applications relevant to the research discussed herein, the flow of the suspending fluid on the particle scale is such that inertial terms $(\rho \left[\frac{\partial u}{\partial t} + (\mathbf{u} \cdot \nabla)\mathbf{u} \right])$ can be ignored. We justify this assumption by considering the Reynolds number Re at the particle scale:

$$Re = \frac{\rho U R}{\eta_f}, \tag{2.7}$$

where ρ is the fluid density, U is the speed of the flow, R is the particle radius, and η_f is the fluid viscosity. We can safely ignore the inertial terms in equation 2.6 when $Re << 1$. As a rough approximation for the maximum Re obtained in a sheared suspension in a typical rheology experiment, we take a 1 µm radius particle moving at a speed $1 \times 10^{-3}\,\mathrm{m\,s^{-1}}$ (using $U = \dot{\gamma}R$, this corresponds to a shear rate $1000\,\mathrm{s^{-1}}$ a relatively high rate in typical rheology experiments) in a fluid of viscosity $1 \times 10^{-2}\,\mathrm{Pa\,s}$ with density $1000\,\mathrm{kg\,m^{-3}}$, this gives $Re = \mathcal{O}(10^{-4})$, which is clearly below 1 and we are therefore safe in assuming inertial effects can be ignored.

2.2.2 Non-Brownian Hard Spheres

The first system we will consider is that of a suspension of idealised non-Brownian hard spheres in a Newtonian liquid. The ideal non-Brownian hard sphere is undeformable, perfectly smooth and spherical, does not interact with other particles directly except by contact so they do not overlap, and does not move due to Brownian motion [1]

For non-Brownian spheres at low Reynolds number we are left with a single time-scale ($1/\dot{\gamma}$), and a single stress scale ($\eta_F/\dot{\gamma}$) to describe the flow. Without an additional time-scale beyond the inverse shear rate, and without a stress scale beyond the hydrodynamic one, the resulting flow must be rate independent, so that the suspension viscosity is simply constant (Newtonian) [10, 11, 34, 35].

The only variable relating to the particles that will affect the flow of the fluid in our hard-sphere system is the number density of particles in the suspension. We therefore define the particle volume fraction,

$$\phi = \frac{V_p}{V_p + V_f} \tag{2.8}$$

here V_p is the total volume of particles, and V_f is the volume of the fluid. In more complex systems, particle volume fraction is one of multiple conditions that affect the behaviour of a particulate suspension. For a simple system of spherical particles suspended in a Newtonian fluid increasing the volume fraction increases the viscosity.

At low particle volume fractions the increase in viscosity is predicted by the simple relation:

$$\frac{\eta}{\eta_f} = \eta_r = \left(1 + \frac{5}{2}\phi\right) \tag{2.9}$$

here η is the suspension viscosity, and η_r is the relative viscosity [10, 11]. This expression captures the hydrodynamic stress induced by the addition of single isolated particles to the suspension. Obviously it does not take a large increase in the volume fraction before higher order particle interactions become important.

[1] Although all particles suspended in a fluid will experience Brownian motion to some extent, Brownian motion can still be ignored in many systems and for practical rheology Brownian effects can be ignored at particle radii $\gtrsim 5\,\mu m$. For such large particles Brownian forces become small enough compared to shear forces such that they can generally be ignored 2.12.

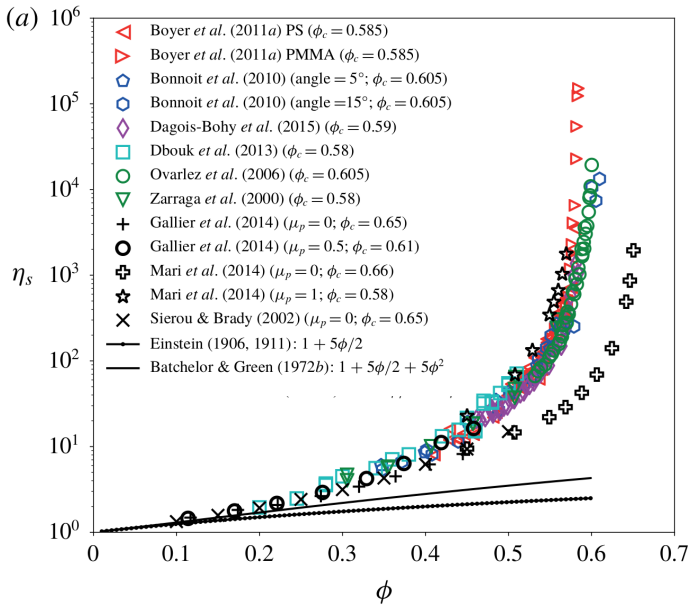

Figure 2.2 Relative viscosity (η_r) vs volume fraction for various suspension systems Boyer et al. (2011) [1], Bonnoit et al. (2010) [2], Dagois-Bohy et al. (2015) [3], Dboul et al. (2013) [4], Ovarelez et al. (2006) [5], Zarraga et al. (2000) [6], Gallier et al. (2014) [7], Mari et al. (2014) [8], Sierou and Brady (2002) [9], Einstein (1906, 1911) [10, 11], and Batchelor and Green (1972b) [12]. Critical volume fractions $\phi_c = \phi_J$ are marked in the legend.

To account for this, higher order terms can be derived:

$$\eta_r = 1 + \frac{5}{2}\phi + B_1\phi^2 + ... \tag{2.10}$$

where B_1 is a the second order coefficient, which can be numerically calculated. There is still some debate about the exact value of B_1, but it is understood to be in the range $7.35 < B_1 < 7.6$ [12, 36].

The calculation of these higher order terms quickly becomes intractable at even moderate concentrations. As such equation 2.10 is only accurate up to $\phi \approx 0.15$ (Fig. 2.2).

The measured viscosity of the suspensions shown Fig. 2.2 shows a clear divergence at high volume fractions, this is ubiquitous of particle suspensions and is called jamming. The viscosity of dense suspensions diverges as $\phi \to \phi_J$, and the system becomes jammed above ϕ_J. In dense non-Brownian suspensions, the viscosity scales as

$$\eta_r = A\left(1 - \frac{\phi}{\phi_J}\right)^{\alpha} \tag{2.11}$$

where η_r is the relative viscosity, $A \approx 1$, and $\alpha \approx -2$ [1, 37]. This is an empirical relation, and many different variations exist depending on the system being looked at. We might expect ϕ_J to coincide with the hard-sphere random close packing limit $\phi_{\mathrm{RCP}} \approx 0.64$ for mono-disperse spheres in $3D$. However, as shown in figure 2.2 (where ϕ_c varies between 0.58 and 0.66), other micro-physical effects can bring ϕ_J significantly below this value.

2.2.3 Brownian Hard Spheres

Previously we considered systems where Brownian motion can be ignored, but for smaller ($R \lesssim 1\,\mu\mathrm{m}$) particles it must be taken into account. Brownian motion is the random movement of suspended particles resulting from thermally driven collisions with the surrounding fluid molecules.

Some systems exhibit a transition between Brownian dominated motion, and shear dominated motion. For these systems, where the Brownian diffusion time-scale is similar to the experimental time-scale, we can consider the relative strength of Brownian and shear effects using the Péclet number:

$$Pe = \frac{\dot{\gamma} R^2}{D_0} = \frac{6\pi\eta_f \dot{\gamma} R^3}{k_B T} \tag{2.12}$$

where D_0 is the diffusion coefficient, and T is the temperature. The Péclet number is the ratio between the shear time-scale ($1/\dot{\gamma}$) and the time taken for a particle to diffuse its own radius D_0/R^2. At low $Pe \lesssim 1$ Brownian motion plays a significant role in the suspension dynamics, whereas at a high $Pe >> 1$, the shear dominates. The Péclet number increases as R^3, meaning that as particle size increases Brownian motion becomes less relevant.

Brownian colloids exhibit a glass transition at a volume fraction $\phi_g \sim 0.58$ [38–40], which can be seen as a yield stress in rheology experiments [17]. Studying the behaviour of Brownian colloids at volume fractions above the glass transitions has shown that it is a result of the caging of particles by their neighbours limiting their ability to rearrange and flow. Increasing the shear rate increases the frequency of cage breaking events allowing the particles, and therefore the colloid, to flow more easily [41].

Below ϕ_g Brownian colloids exhibit shear thinning, and the degree of shear thinning is dependent on the volume fraction of the suspension. Figure 2.3

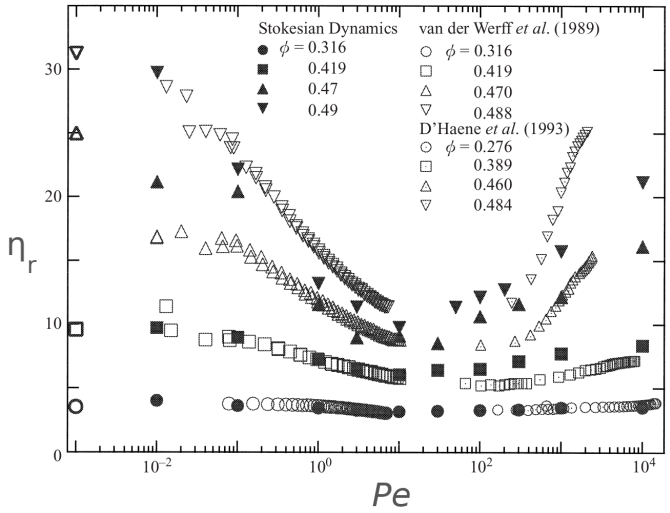

Figure 2.3 Viscosity against Péclet number calculated using Stokesian dynamics (filled symbols) and measured (empty symbols) at various volume fractions(legend). Taken from Foss et al. [13] with data from D'haene et al. [14] and van der Werff et al. [15].

shows the decrease in relative viscosity as the Péclet number increases and shear dominates the suspensions behaviour.

2.2.4 Particle Interactions: The Derjaguin Approximation

In the next section we will consider finite ranged interactions between particles in solution. When computing the interactions between macroscopic bodies, it is possible to makes use of the Derjaguin approximation, which allows the force between the finite objects (e.g. two spheres, a sphere and a wall, etc.) to be expressed in terms of the free energy density between two infinite flat plates. The Derjaguin approximation is only correct under specific geometric constraints[2].

We first want to consider $W(D)$, which is the potential per unit area for two infinite flat plates at a separation D (this is significantly easier to calculate for electrostatic repulsion). By considering rings of the spheres at separation Z (Fig. 2.4) and integrating over the surface of the sphere we can calculate the potential

[2]This approximation should apply at small separations d (where $d << R$) for any interaction force arising from the potential $U(d)$, provided $U(d)$ is short ranged compared to the size of the macroscopic objects. The constraint that the range of the interaction is much smaller than the particle radius may depend on precisely how one defines the range of the interaction.

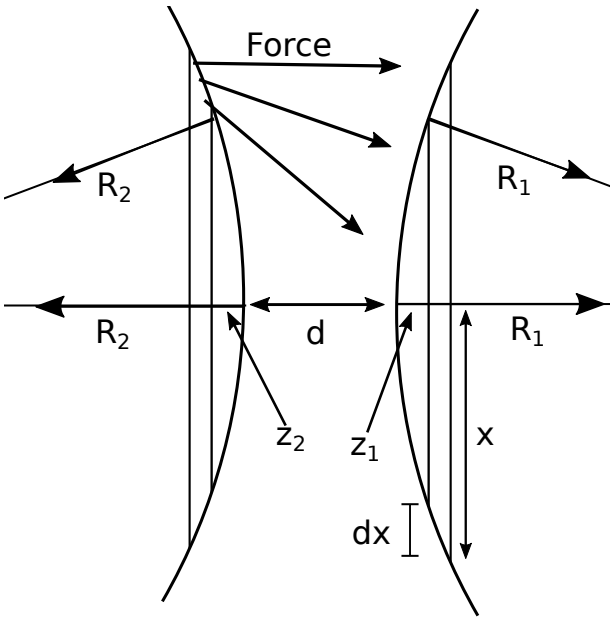

Figure 2.4 Diagram of the Derjaguin approximation which relates the force between two spheres $F(h)$ to the energy per unit area of two flat surfaces $W(h)$.

between the two spheres $U(d)$ as

$$U(d) = \int_{Z=d}^{Z=\infty} 2\pi x W(Z) dx. \tag{2.13}$$

The rings of the spheres are separated by a distance $Z = d + z_1 + z_2$, where d is the surface-to-surface separation and Z can be approximated to

$$Z = d + \frac{x^2}{2}\left(\frac{1}{R_1} + \frac{1}{R_2}\right), \tag{2.14}$$

assuming $d << R_1, R_2$ (Fig. 2.4). This gives

$$dx = \frac{1}{x}\left(\frac{R_1 R_2}{R_1 + R_2}\right) dZ, \tag{2.15}$$

which when substituted into equation 2.13 gives,

$$U(d) \approx 2\pi \left(\frac{R_1 R_2}{R_1 + R_2}\right) \int_d^\infty W(Z) dZ. \tag{2.16}$$

Using the relation $F(Z) \approx -\mathrm{d}U(Z)/\mathrm{d}Z$ we get

$$F(d) \approx 2\pi R_{\text{eff}} W(d). \tag{2.17}$$

where $R_{\text{eff}} = \left(\frac{R_1 R_2}{R_1+R_2}\right)$ is the effective radius ($R_{\text{eff}} = R/2$ for two identical spheres).

2.2.5 Stability and Repulsion

Although hard spheres were a useful starting point for understanding suspensions in practice, true hard spheres remain elusive [42]. In real suspensions finite-ranged interparticle interactions cannot always be ignored. In particular, van der Waals forces resulting from dipole fluctuations are ubiquitous to particle suspensions. The result of these dipole fluctuations is an attractive force, which for two particles of radius R at a surface-to-surface separation d is given by,

$$F = -AR/12d^2, \tag{2.18}$$

where A is the non-retarded Hamamker constant. A is determined by the relative dielectric properties of the particles and the suspending fluid. The non-retarded Hamaker constant for identical particles (p) suspended in fluid (f) is calculated from their relative dielectric constants (ϵ_p, ϵ_f) and their refractive indices (n_p, n_f), using the Lifshitz equation [43],

$$A = \frac{3}{4} k_B T \left(\frac{\epsilon_p - \epsilon_f}{\epsilon_p + \epsilon_f}\right)^2 + \frac{3h\nu_e}{16\sqrt{2}} \frac{(n_p^2 - n_f^2)^2}{(n_p^2 + n_f^2)^{3/2}} \tag{2.19}$$

where ν_e is the electron UV absorption frequency, and h is the Planck constant. By minimising the difference between the refractive indices and the dielectric constants one can minimize the Hamaker constant and therefore the attractive van der Waals force. Minimising the attractive force is useful for maintaining dispersion in colloidal suspensions.

The van der Waals force, given by equation 2.18, diverges at $d \to 0$, however it can be modified by introducing a finite offset ($d + \delta$) such that it does not diverge [16]. Surface roughness can also affect the van der Waals force; this can be incorporated by using a modified value of he Hamaker constant [16, 44, 45]. Increasing the surface roughness is generally understood to decrease the value of the Hamaker constant [16].

As the van der Waals attractive force can never be completely eliminated, we are left with an attractive suspension. To make the suspension stable an additional repulsive force needs to be present. There are two main mechanisms for this stabilising repulsive force in particle suspensions, steric repulsion, and electrostatic repulsion.

Steric repulsion is the result of the presence of polymer chains on the particle surface. The repulsive force originates from the increase in polymer concentration, and therefore osmotic pressure, as the particle surfaces approach one another [46]. Steric stabilisation is present in many well studied 'model' shear thickening suspensions, including PHSA-stabilised PMMA [20], and aqueous cornstarch suspensions [47]. In this thesis we will largely look at electrostatically stabilized systems.

To understand electrostatic repulsion, we must first consider the particle surface. Although we often assume suspended particles to be chemically inert, neutral solid particles can obtain a surface charge by the disassociation of ions from the particle surface. The surfaces of silica particles suspended in an aqueous fluid become charged by the disassociation of silanol groups $\mathrm{SiOH} \rightleftharpoons \mathrm{SiO^-} + \mathrm{H^+}$. This results in a negatively charged particle surface for a fluid with $pH > 3$ (the isoelectric point for silica) [48, 49], which alters the distribution of ions in the surrounding solution. Although referred to as electrostatic repulsion throughout this thesis, and only being possible as a result of the charged surface of the particles leading to the distribution of ions around the particle surface, the mechanism of electrostatic repulsion is actually osmotic in nature. The repulsion comes from the concentration of ions increasing in regions where particle separation is small. While there is debate about the exact microstructure and ion distribution, the general 'double layer' picture consists of a very thin layer of counter-ions bound near the charged surface (known as the Stern layer), with a second outer diffuse layer of mobile ions at extended distances from the charged surface [43, 46]. The form and strength of the electrostatic repulsion is determined by the distribution of ions in solution, which is in turn related to the electrostatic potential ψ. ψ is governed by the equation:

$$\nabla^2\psi = -\rho/\epsilon\epsilon_0. \tag{2.20}$$

where ρ is the charge density, ϵ is the relative dielectric constant, and ϵ_0 is the permittivity of free space.

However in contrast to conventional electrostatic problems We also have to consider how ρ depends on the distribution of ions within the solution. For an ionic species with valency z_i and bulk concentration c_i, their local distribution is given by the Boltzmann distribution

$$c_i(\vec{x}) = c_i e^{-qz_i\psi(\vec{x})/k_BT} \tag{2.21}$$

where q (1.6×10^{-19} C) is the elementary charge. The net free charge density is the sum over all ionic species in the solution,

$$\nabla^2\psi = -\frac{q}{\epsilon_0\epsilon}\sum_i z_i c_i e^{-z_i e\psi/k_BT}. \tag{2.22}$$

It is common to consider this equation for the case of two infinite flat plates, this means replacing the Laplacian with a second derivative, $\nabla^2\psi \to \frac{d^2\psi}{dx^2}$. The boundary conditions must be chosen carefully as neither the surface charge density nor the surface potential stay constant as the surfaces are brought together. It is possible to choose an 'intermediate' boundary condition, which uses a charge regulation parameter P, which is neither a constant potential nor a constant charge boundary condition [16, 50].

To calculate the force between two plates we consider the osmotic pressure Π, which can be expressed in terms of the mid-plane potential ψ_m,

$$\Pi = k_BT\sum_i c_i\left[e^{-qz_i\psi_m/k_BT} - 1\right]. \tag{2.23}$$

Although ψ_m can be found by solving 2.22 numerically for given boundary conditions [16, 51–53], it is often helpful to consider the case of small potentials ($q\psi/k_BT << 1$ or $\psi \leq 25\,\text{mV}$), where equation 2.22 can be linearised and solved analytically giving

$$\psi_x \approx \psi_0 e^{-\kappa x}, \tag{2.24}$$

where ψ_0 is the potential at the charged surface. This approximation, known as the Debye-Hückel approximation, describes the exponential decay of the potential away from the surface with a decay length

$$\lambda_h = 1/\kappa = \left(\frac{\epsilon\epsilon_0 k_BT}{\sum_i c_i z_i^2 q^2}\right)^{1/2}. \tag{2.25}$$

Equation 2.25 does not consider the difference in effect between asymmetric

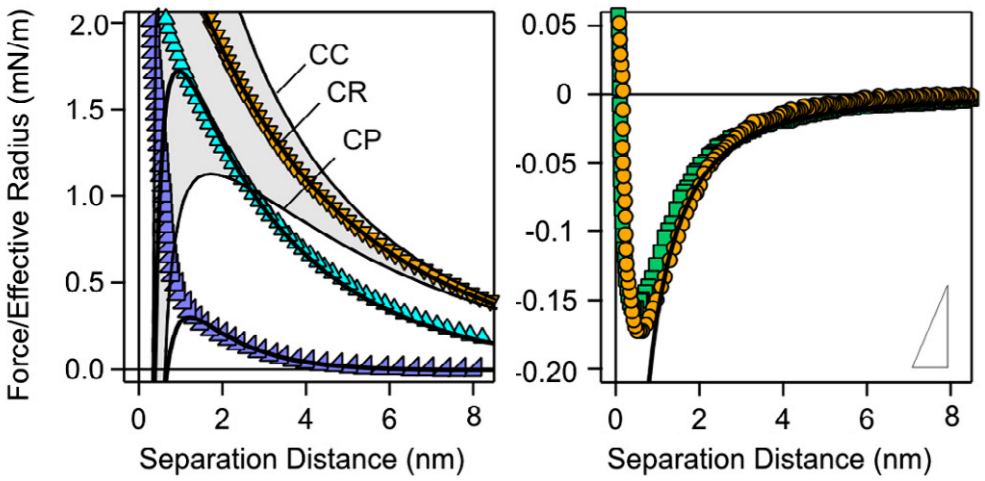

Figure 2.5 Force profile measurements between spherical silica particles at various KCl concentrations [16], the solid lines are fits by solving the Poisson-Boltzmann equation using a modified particle surface boundary condition, called charge regulation (CR). The DLVO graphs are fit using standard DLVO theory. The left figure shows a range of results between two special cases of charge regulation, constant charge (CC) and constant potential (CP).

multivalent ions of different charges, so that a $2:1$ salt gives the same κ as a $1:2$ salt.

In the low potential limit the surface potential ψ_0 and the surface charge density σ_0 are related by $\sigma_0 \approx \epsilon\epsilon_0\kappa\psi_0$, and the free energy density between two infinite plates separated by a gap d is given by

$$W(d) \approx 2\epsilon\epsilon_0\kappa\psi_0^2 e^{-\kappa d} = 2\sigma_0^2 e^{-\kappa d}/\kappa\epsilon\epsilon_0. \tag{2.26}$$

From the above Derjaguin approximation we know that $F(d) = \pi R W(d)$ for identical spheres of radius R, therefore

$$F(d) \approx 2\pi R\epsilon\epsilon_0\kappa\psi_0^2 e^{-\kappa d} = 2\pi R\sigma_0^2 e^{-\kappa d}/\kappa\epsilon\epsilon_0. \tag{2.27}$$

The Debye-Hückel approximation is still useful for understanding the effect of ionic strength on the interparticle forces. The ionic strength I allows us to gauge how the Debye length (Eq.2.25) scales with ion concentration,

$$I \equiv \frac{1}{2}\sum_i c_i z_i^2. \tag{2.28}$$

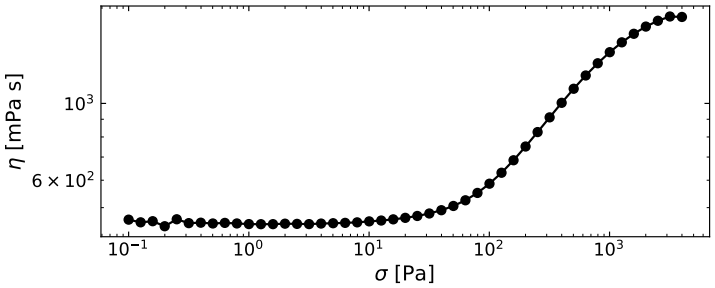

Figure 2.6 Flow curve of a 0.75 µm radius silica suspended in 80 wt.% glycerol/water with 47 mM LiCl salt and 0.2 mM sodium fluoroscein salt.

From the equations in 2.26 and 2.27 we know that the force decreases as $\kappa e^{-\kappa d}$ for the limit of constant ψ_0 and as $\frac{1}{\kappa}e^{-\kappa d}$ in the limit of constant σ_0. The relation between ψ_0, σ_0, and I depends on the specific surface chemistry. For the case of silica in aqueous solution, it is generally well established that while σ_0 is not strictly constant, the surface potential ψ_0 decreases with increasing I, resulting in a weaker electrostatic repulsive force [54–56].

In general it is assumed that the attractive van der Waals forces and repulsive electrostatic double layer forces can be linearly added to give the net force between two surfaces in solution. This theory is referred to as the Derjaguin-Landau-Verwey-Overbeek or DLVO theory. From figure 2.5 the theoretical predictions (solid lines) for the repulsive double layer force clearly dominates at large separations, whereas the attractive van der Waals force dominates at small separations. The experimental results show a strong repulsive force at small separations, this mismatch suggests an interaction present that is not within the DLVO theory. In the following section we will see that short range interactions have a strong effect on dense suspension rheology. There are many explanations for the short range repulsion seen in figure 2.5 including: bound surface ions, polysilic acid, or hydration forces [57–61], and there are clear contradictions between some of the conclusions. Some work appears to show that silanol groups do effect the short range repulsion [57], and other work shows that the number of silanol groups does not effect the short range repulsion [60]. Some of the results are unclear and compare results at different pH [60], making them slightly dubious.

2.2.6 Shear Thickening in Stable Repulsive Suspensions

Shear thickening suspensions have stress dependent viscosities; their defining feature being that the viscosity increases with increasing applied stress [62]. The flow curve in figure 2.6 shows a standard shear thickening curve; there is a clear transition from a low stress Newtonian plateau to a high stress Newtonian plateau, with a shear thickening region in between. The high viscosity plateau is often hard to measure due to particle migration effects leading to shear thinning and hysteresis, as well as limits to the maximum shear rate that can be applied to the sample. The example in figure 2.6 is for data taken using silica, but almost identical flow curves are seen in a variety of model systems including polymer spheres [20, 28], cornstarch [63, 64], and calcite [25].

The low stress plateau can be understood in terms of the non-Brownian hard sphere interactions discussed in section 2.2.2. In figure 2.7 we see the low stress viscosity diverges at a volume fractions close to random close packing ($\phi \approx 0.64$), whereas the high stress Newtonian plateau diverges at a value significantly lower than random close packing ($\phi_M \approx 0.55 < \phi_{\mathrm{RCP}}$). The lower value of ϕ at which the viscosity diverges at high stresses is a result of the transition of the particle contacts from lubricated to frictional [65]. From granular rheology we know that systems of particles with frictional contacts jam at a random loose packing volume fraction ($\phi_{\mathrm{RLP}} \approx 0.55$) [66, 67], which also decreases with increasing friction coefficient (μ) between the particles [8]. For experimental measurements the frictional coefficient is not necessarily known, but measurements show that the value of ϕ_M does change depending on the system measured [20, 62, 68], suggesting the friction coefficient varies between systems.

The Wyart-Cates Model

The high and low stress plateaus are therefore explicable in terms of the particle-particle interactions, they are either frictional or lubricated. But for the intermediate values of the viscosity, where some interactions are lubricated and some are frictional, we require a more detailed approach.

The Wyart-Cates model (WC-model) is the result of a phenomenological analysis of frictional particles with a finite repulsive force. Although referred to as a model, the ability of the Wyart-Cates model to predict the behaviour of dense suspensions is currently limited, and is more often used to simply

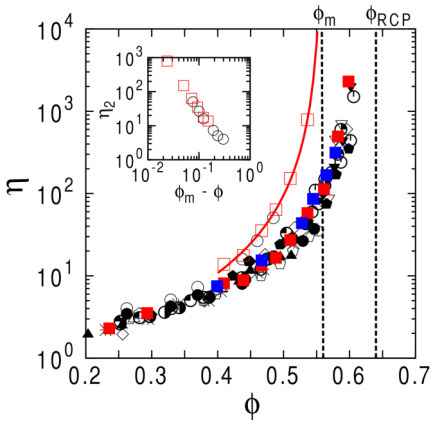

Figure 2.7 Least squares fits low viscosity plateau viscosity (filled), and high viscosity plateau viscosity (empty), the solid red line is a fit of $A(1-\phi/\phi_M)^{-\alpha}$ with $A = 0.20(9)$, $\phi_M = 0.558(5)$, and $\alpha = 2.2$. The work used PMMA spheres of various diameters ranging from stabilized by PHSA 'hairs'. The low stress data consists of various particle suspensions with diameters in the range 404 nm to 3770 nm including data from other work with the volume fraction shifted up by 5% [14, 17–19]. The high stress data consists solely of high stress viscosity measurements of $D = 3770$ nm particle suspensions. Figure adapted from Guy et al. [20].

extract characteristic parameters of a given suspension. From experiments and simulations we know there is a transition between two different viscosity plateaus in shear thickening dense particle suspensions (Fig. 2.6) [20, 62, 65, 68], furthermore we know that the viscosity of these stress plateaus diverge at different volume fractions (Fig. 2.7) [8, 20, 62, 65, 68]. In equation 2.11 we considered a jamming volume fraction which depended only on the particles themselves; for a shear thickening system the decrease in the jamming volume fraction at high stresses is described as a transition between two limits (ϕ_0 and ϕ_M) of the jamming volume fraction ϕ_J, which is related to the fraction of particle contacts that are frictional f. This transition is modelled as a linear interpolation between the two limits of ϕ_J as

$$\phi_J = f\phi_M + (1-f)\phi_0. \tag{2.29}$$

The transition to frictional contacts occurs because the shear on the system pushes the particles together; for this to create frictional contacts the force must exceed some critical interparticle repulsive force F^*. Using dimensional analysis, we can relate the critical stress σ^* (called the onset stress of shear thickening) to F^*:

$$\sigma^* \propto \frac{F^*}{R^2}. \tag{2.30}$$

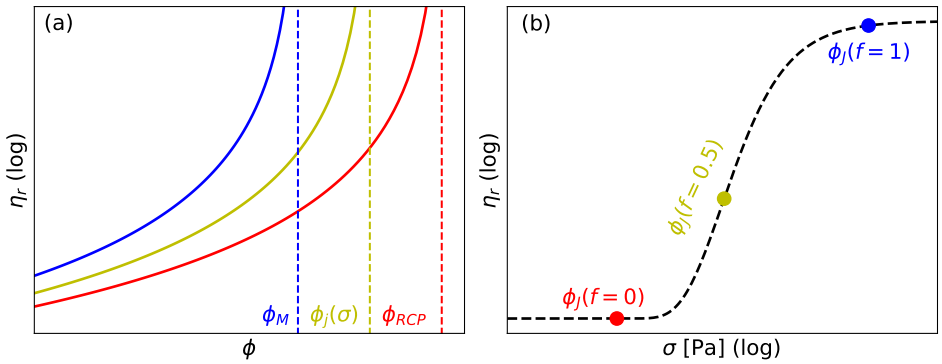

Figure 2.8 (a) Schematic of the change in the relation between the relative viscosity and the particle volume fraction, $\phi_0 = \phi_J(f = 0)$ and $\phi_M = \phi_J(f = 1)$, (b) Schematic of flow-curves, with regions relating to ϕ_M, ϕ_0, and an intermediate value $\phi_J(\sigma)$.

For a bulk applied stress σ_{App} there is a distribution of local forces F_L pushing the particles together. The fraction of particles forced into frictional contact at a given applied stress $f(\sigma)$ depends on the form of the local stress distribution. For a simple exponential force distribution, one can show that the fraction of frictional contacts takes the form[3] [20]

$$f = \exp\left(-\left(\frac{\sigma^*}{\sigma}\right)^{\beta}\right). \tag{2.31}$$

where β is called the spreading exponent. Inhomogeneities within a shear thickening suspension, including variations in size, surface chemistry, and surface roughness, can cause the distribution of particles in frictional contact at a given σ to spread out [69, 70]. This spreading is captured by β; for a relatively homogeneous suspension we should find $\beta \approx 1$.

To calculate the relative viscosity from this new jamming fraction we use equation 2.11. In general we use the same form for both the viscosity plateaus (i.e. α and A are the same for all ϕ_J). Within the WC-model, the increase in the fraction of frictional contacts f lowers the volume fraction at which the system will jam (Fig. 2.8). The exact nature of the transition is dependant on the form of equation 2.31 chosen.

The WC-model shows good agreement with simulated data of shear thickening suspensions, which exhibits continuous (CST) and discontinuous (DST) shear thickening suspensions (Fig. 2.9(a,b)). Where CST is characterised by a

[3]Equation 2.31 is simply one form of the possible distributions of particles with $F_L > F^*$.

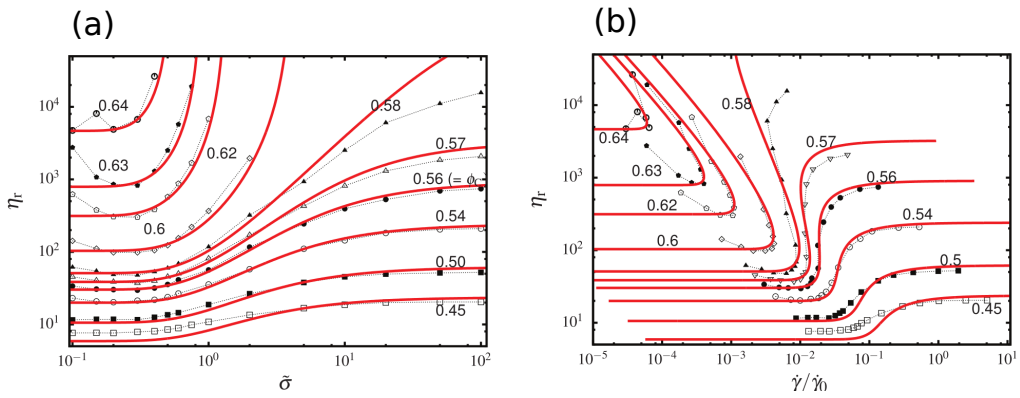

Figure 2.9 Results of simulations at various volume fractions (labelled) of frictional particles with $\mu = 1$. The red lines are fits to the data usuing a Wyart-Cats type model. (a) is $\eta_r(\dot{\gamma}/\dot{\gamma}_0$ where $\dot{\gamma}/\dot{\gamma}_0$ is the dimensionless shear rate. (b) $\eta_r(\tilde{\sigma})$ where $\tilde{\sigma}$ is the dimensionless stress (σ/σ^*). Adapted from Singh et al. [21].

continuous increase in the viscosity with shear rate, and DST a discontinuous increase in viscosity with shear rate [62]. For practical rheology, where stress controlled measurements are possible, DST can be observed as a continuous increase in viscosity with applied stress.

For $\phi > \phi_M$ shear thickening suspensions shear jam, which is seen as a divergence in the viscosity with increasing applied stress [62, 63], which leads to the cessation of flow [71]. Numerical simulations show good agreement with the WC-model for shear jammed states, and show clear divergence in the viscosity (Fig. 2.9(a)) [21, 23]. For practical rheology such a divergence is rarely observed [20, 26, 72], and instead we observe materials that still flow under shear. This may be a result of the continuous breakdown and formation of the system spanning structures that cause shear jamming [73], as well as the difficulty in maintaining uniform strain field in practical experiments [74]. In the Wyart-Cates model the viscosity diverges as the jamming volume fraction $\phi_J(\sigma)$ approaches the volume fraction of the suspension.

Both CST and DST are observed below ϕ_M. DST below ϕ_M is characterised by 's' shaped flow curves, which can show backwards bending in simulations (Fig. 2.9(b)), and in the WC-model. For practical experiments, DST below ϕ_M is seen as an increase in the viscosity with constant shear rate [71]. CST occurs at lower volume fractions than DST. Often the transition between CST and DST can be observed as a transition from negative to positive first normal stress difference [68].

2.3 Current Challenges in Suspension Rheology

The Wyart-Cates model describes the bulk steady state rheology of many different suspensions, but the model is limited for a number of reasons. Firstly there is no way to predict the parameters required to fit the model, secondly the model is only applicable to bulk rheology and sheds no light on the small scale or 'local' behaviour of dense suspensions [27, 28, 75, 76], and finally it does not tell us anything about the non-steady-state rheology of dense suspensions [26, 63, 72, 75, 77–79].

2.3.1 What do we mean by friction?

There is still some debate over what the frictional nature of the interparticle contacts described by the WC-model are [80–83]. Conventional static friction imposes a condition relating the normal and tangential contact forces (F_N and F_T, respectively)

$$|F_T| \leq \mu |F_N|, \tag{2.32}$$

where μ is the static friction coefficient. This inequality, known as the Coulomb yield criteria, allows the tangential contact force to take on any value required to prevent sliding motion up to a limit $\mu|F_N|$, so that sliding is only possible once this threshold is exceeded.

Simulation implementing the frictional contact model can reproduce the shear thickening rheology typically observed in experiments, with continuous shear thickening exhibiting well-defined low and high-stress plateaus below a μ-dependant ϕ_M, alongside the backwards bending flow curves and shear jammed states above ϕ_M [84, 85].

While the success of these numerical models and the analytic Wyart-Cates model demonstrate the utility of this lubricated-to-frictional picture in describing shear thickening, the detailed particle contact tribology remains unresolved. Conventional smooth-sphere 'Stokesian dynamics' simulations, which lack static friction and only consider hydrodynamic interactions, cannot reproduce the shear thickening observed in experiments [86, 87]. Modified schemes, which either alter the tangential lubrication forces at small separations [88] or introduce asperities on the particle surface show that hydrodynamic interactions can

produce constraining interactions similar to the frictional Coulomb yield criteria (Eq. 2.32).

2.3.2 Shear Thickening and Interparticle Forces

The onset stress of shear thickening is a characteristic stress of shear thickening suspensions. Previously the onset of shear thickening was ill-defined, with both critical shear stresses σ_c and critical shear rates $\dot{\gamma}_c$ being used. The Wyart-Cates model introduces a fitting parameter σ^*, which can be used as a consistent measure of the onset of shear thickening.

Previous work on size scaling of the parameter σ^* has shown that for sterically stabilised suspensions there is a clear $1/R^2$ scaling [20]. This result would suggest a critical repulsive force between particles which is independent of particle size.

The size dependence of σ^* (and therefore F^*) is not well established in charge stabilised systems. One way to study the behaviour of many systems of a similar compositions is to aggregate experimental results look at charge stabilized systems of aqueous silica and glass suggest $\sigma^* \sim R^{-1.6}$ [70]. These results could be affected by differences between the different experimental samples in surface chemistry, dispersion methods, or suspending fluid properties. For an electrostatically stabilized system we would expect the scaling of the onset stress of shear thickening to be $1/R$ [20]. This scaling is found by combing equations 2.30 and 2.16.

Previous results measuring the size dependence of the onset of shear thickening in electrostatically stabilised dense suspensions show a clear downwards trend in the onset stress with increasing particle size with a slope of -2.11 in the log-log scaling (Fig. 2.10); this result is inconsistent with the $1/R$ scaling predicted. The termination of the manufacturing process used by Maranzano et al. [22] uses a silane coupling agent in a departure from standard Stöber synthesis. The coupling agent, which is used to more accurately to control size, neutralizes nearly all of the surface charge groups. The surface charge is the basis of electrostatic stabilisation, therefore this will have strongly affected the interparticle forces. The coupling agent may even act as a steric stabiliser, which may explain the similar scaling to steric systems [20].

It is possible to control the behaviour of dense suspensions by increasing the

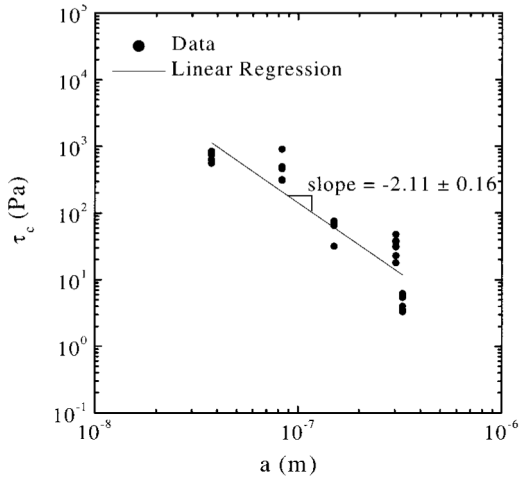

Figure 2.10 Scaling of the critical shear stress τ_c with increasing particle radius a, equivalent to the onset stress σ^*, of silica suspensions with size. The silica is dispersed in tetrahydrofurfuryl alcohol, and a silane coupling agent was added to remove all surface charge. The data was taken for a range of volume fractions, reproduced from the work of Maranzano et al. [22]

attractive force between the particles. Simulations and experiments have shown that increasing the strength of the attractive force in dense suspensions leads to yield stress behaviour [23, 89]. Attractive dense suspensions show frictional behaviour, and with sufficient measurements can be shown to form adhesive contacts [90]. Adhesive contacts are understood to be a separate additional constraint to motion when particles are in close contact [90, 91]. This constraint is an attractive force at contact such that the particles cannot roll past one another when in frictional contact.

Shear Thinning in Brownian and non-Brownian Suspensions

Many shear thickening suspensions also exhibit shear thinning behaviour. This shear thinning can come in different forms depending on the nature of the suspension. For repulsive particles we see shear thinning commonly seen in suspensions where no shear thickening is observed (Fig. 2.11 (a,c)) [20, 24, 92, 93]. We see a clear decrease in the severity of shear thinning with decreasing volume fraction (Fig. 2.11). Decreasing the range of the repulsive force in shear thickening suspensions has also be shown in simulations to decrease the severity of the shear thinning observed (Fig. 2.11(c)).

Though we generally consider volume fraction as relating to the hard-sphere

particle radius, for the case of the effect of nearest neighbours on motion it is better to consider the extended radius R_{ext}. For a particle with some repulsive interaction, R_{ext} takes the range of the repulsive forces into account. For a higher R_{ext} we have a higher effective volume fraction $\phi_{\text{ext}} > \phi$ [24, 94].

In attractive non-Brownian suspensions we see shear thinning results from the overcoming of the finite ranged attraction between the particles (Fig. 2.11(c)). As the strength of the attractive force increases the strength of the shear thinning increases [23, 89]. This behaviour is qualitatively to the behaviour systems where the formation of adhesive contacts constrain particle motion [25, 90, 93]. The qualitative similarity between the behaviours of suspensions with finite attraction and adhesion means that in-depth measurements and understanding of the particle interactions themselves are necessary to distinguish the two conclusively.

2.3.3 Time-scales in Shear Thickening Systems

The Wyart-Cates model only describes steady state behaviour, but dense suspensions can show time dependent behaviour [26, 72, 77, 95, 96]. This time dependent behaviour is thought to relate to time-scales in shear thickening such as frictional contact formation and relaxation, and contact network formation.

Repulsive suspensions with volume fractions close to and above ϕ_M show shear rate oscillations [26, 75]. The resulting oscillations were shown to increase in frequency with increasing applied stress (Figs. 2.12(a,b)). Although these oscillations are a result of the interplay between the suspensions and the rheometer tool inertia, they can be used to extract characteristic time-scales and strain-scales for shear thickening cornstarch suspensions.

The model used by Richards et al. [26] to describe the observed shear rate oscillations gives two characteristic scales, the first γ_0 is the characteristic strain, and the second t_r the relaxation time. For cornstarch in glycerol/water the values $t_r \approx 0.24\,\text{s}$ and $\gamma_0 \sim \mathcal{O}(10^{-1})$ were found. γ_0 can be converted to a time-scale t_0 using the equation

$$t_0 = \frac{\eta_f \gamma_0}{\sigma^*}. \tag{2.33}$$

This gives $t_0 \sim 10^{-4}\,\text{s}$, which is several of orders of magnitude quicker than the relaxation time t_r, which would be necessary for the fraction of frictional contacts to increase with time.

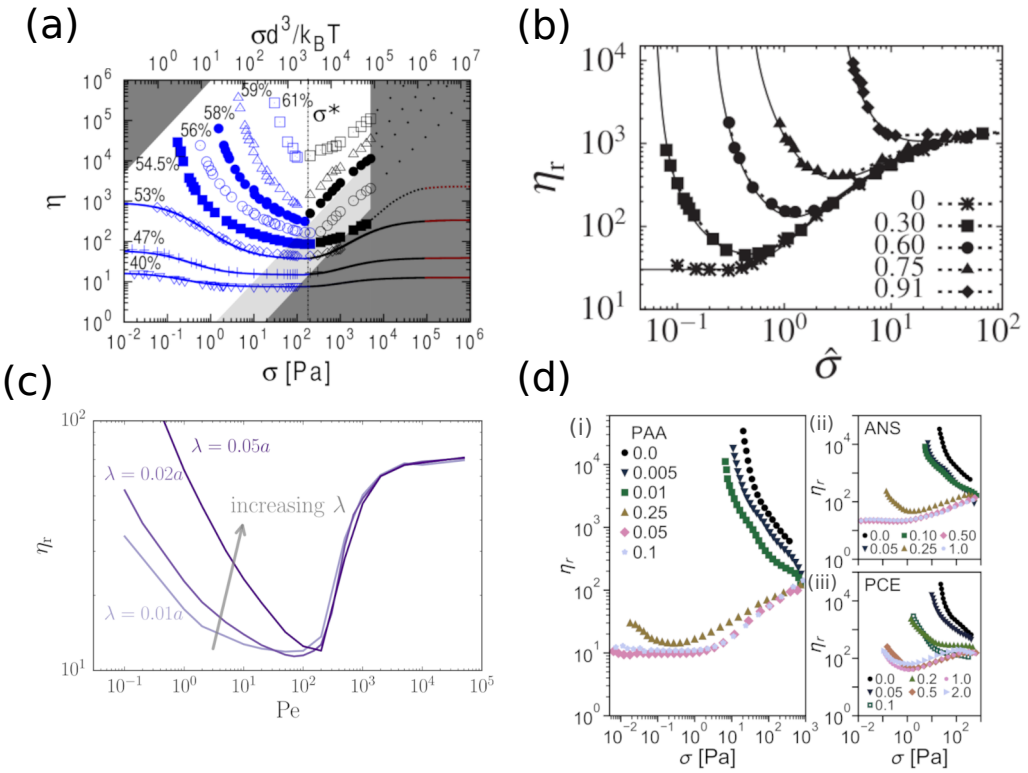

Figure 2.11 Graphs showing suspensions which exhibit both shear thinning and shear thickening behaviour despite different dominant particle-particle interaction mechanisms. (a) Relative viscosity η vs stress in units of σ and of $\sigma d^3/k_bT$ of 202 nm, radius PHSA coated PMMA (sterically stabilized) spheres at various volume fractions [20]. (b) Relative viscosity η_r vs scaled stress σ/σ^{RA} of simulated frictional non-Brownian particles with an increasingly strong finite ranged attractive force (legend) [23]. (c) Relative viscosity η_r vs Péclet number of Brownian particles with a finite ranged repulsive force of the form $|F_R| = F^* \exp -d/\lambda$ [24]. (d) Relative viscosity η_r vs stress σ for 'adhesive' calcite with increasing surfactant concentrations (d)(i) Polyacrylic Acid (PAA) (d)(ii) Alkyl-naphthalene sulphonate condensate sodium salt (ANS) (d)(iii) Polycarboxylate ether (PCE) [25].

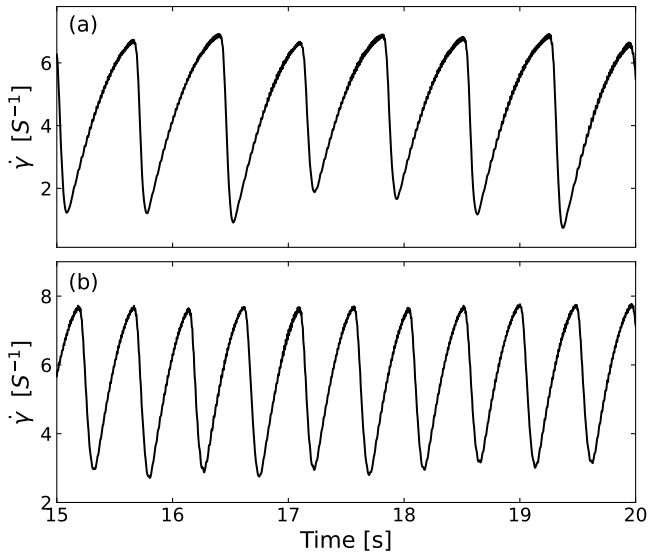

Figure 2.12 Shear rate oscillations for cornstarch suspended in 50wt.% glycerol/water at (a) 4.8Pa and (b) 7.2Pa [26].

Barik et al. [97] used strain controlled measurements of shear thickening polystyrene in poly-ethylene glycol (PEG) in the shear jamming regime ($0.57 < \phi < 0.61$), to measure the relaxation of the system after the application of a shear strain. Two different time-scales were observed, the time taken for the system to go through a discontinuous relaxation, and an exponential relaxation time. The discontinuous relaxation called τ_f, is only present for high shear strains and volume fractions in the shear jamming regime. The lack of short time-scale for low ϕ values is consistent with there being a change in the nature of the frictional contacts above ϕ_M. As this short relaxation is only present above ϕ_M it is likely a time-scale related to the formation of system spanning networks.

The two systems discussed above, that of cornstarch in glycerol/water and polystyrene in (PEG) show contact relaxation time-scales $O(10^{-1})$s much larger than contact formation time-scales $O(10^{-4})$s. It is likely that the relaxation time-scale must be significantly slower for thatn the contact formation time-scale for shear thickening to occur.

2.3.4 Local Behaviour

Advancements in measurement techniques have allowed for the measurement of local behaviour in dense suspensions, and suggest that dense shear thickening suspensions under shear are not always homogeneous [27, 28, 75, 76].

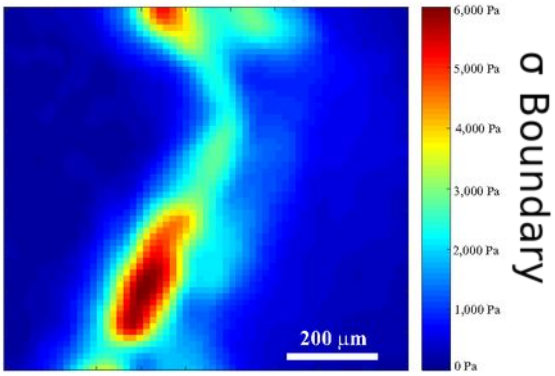

Figure 2.13 Still image the boundary stress in the velocity direction of a suspensions of 0.48 µm radius silica particles suspended in 80 wt.% glycerol/water at $\phi = 0.56$ taken at a fixed applied stress 1000 Pa [27].

Silica suspended in glycerol/water has been shown to form transient high stress regions when sheared above its critical shear stress (Fig. 2.13) [27, 75]. These regions move in the flow direction at a speed between that of the top and bottom plates, and appear at volume fractions which are within the CST regime. Similar results have been produced for cornstarch in glycerol/water suspensions [76]. This suggests that even below the DST regime, system spanning high stress regions still form and propagate, which is consistent with simulations data suggesting the formaton of force chains in the CST regime [8]. These measurements were taken using boundary stress microscopy, a novel technique that allows for the measurement of local stress at the lower boundary of a sheared suspension.

Current understanding of shear thickening suspensions only predicts the existence of system spanning networks at volume fractions above or close to ϕ_M [68]. This understanding of shear thickening raises questions about the ubiquity of the fluctuations observed by Rathee et al. [27], which were observed in the CST region. Later results give a full picture of the local stress around the whole tool [75], and show both a transient time dependent shear rate, as well as boundary stress fluctuations. The boundary stress fluctuations become more frequent with increasing applied stress, increasing the volume averaged viscosity.

Fluctuations have also been observed in the local volume fraction of shear thickening samples [28]. High volume fraction regions appear periodically in a couette geometry and can be measured using X-ray absorption (Fig. 2.14). The suspensions, comprising of PVC particles suspended in DINCH, exhibit higher than average volume fraction regions for applied stresses above the shear thickening onset. Some of the high volume fraction regions are at the jamming

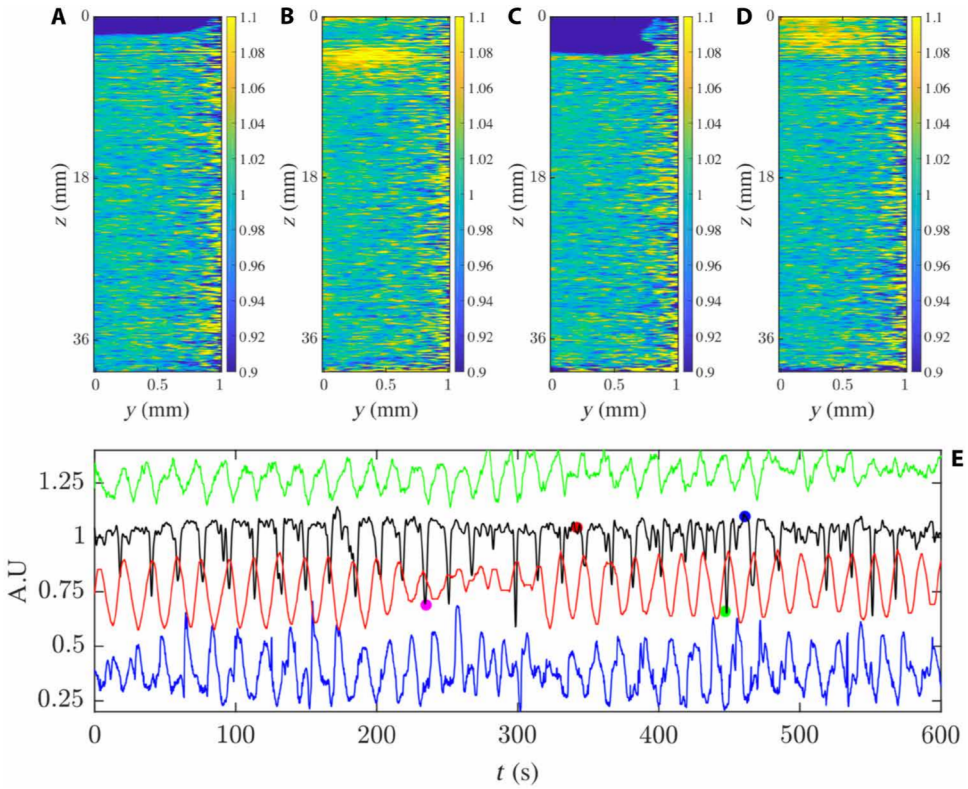

Figure 2.14 Fluctuations in the particle density measured by X-ray absorption. (A) is the particle density map at ● , (B) is the same at ● , (C) the same at ● , (D) the same at ● (E), from top to bottom, green line is the macroscopic shear rate measured as $\dot{\gamma}/10-0.7$; black line is the solid fraction measured from the average 1 cm below the interface; red line is the normalized rotor displacement ($d_N^R = d^R \times 6.89 + 0.75$ where d^R is the rotor displacement in mm ; and the blue line is the normalized interface displacement ($p_N = p/5 + 0.4$) where p is the interface displacement in mm. Taken from Overlez et al. [28]

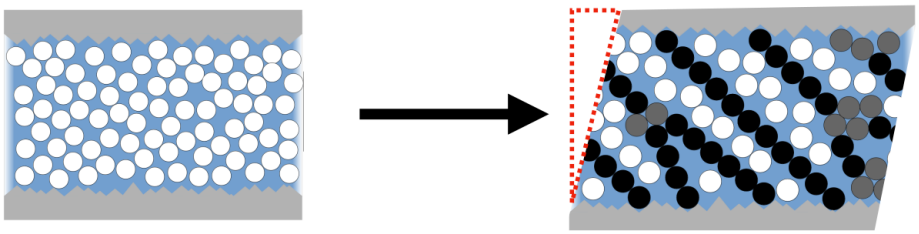

Figure 2.15 Diagram of the formation of force chains under applied shear stress.

volume fraction, and are presumably jammed and solid-like. These high volume fraction regions will therefore carry a higher than average stress. These regions will also presumably be at a higher stress than lower volume fraction regions. The stress fluctuations observed were also related to the geometry; the high stress regions produced a normal force which pushed the central rotor slightly out of alignment.

Cornstarch suspensions show large propagating regions of high boundary stress [76], which may also appear as a local oscillating normal force [98], or as oscillating high volume fraction regions [28]. These large-scale fluctuations are measured on plate-plate [76, 98] or couette [28] geometries which have stress gradients and although such large-scale fluctuations may be intrinsic to dense suspensions, they may also be strongly related to the tool geometry. These large-scale fluctuations suggest something qualitatively different to those of Rathee et al. [27] which show very local, smaller-scale fluctuations. These were measured on a cone-plate rheometer, where one would assume relatively homogeneous shear, though effects of the geometry cannot necessarily be ignored. Large-scale fluctuations, although not predicted by the Wyart-Cates model, seem more consistent with an inhomogeneous distribution of frictional contacts f.

Local behaviour in dense suspensions can also relate to the formation of system spanning structures called force chains (Fig. 2.15). Such structures can be described as fragile as they are maintained by the action of shear on the system [99], and can be broken by the reversal of shear [90]. Such structures have been observed in simulations of both wet and dry granular suspensions [8, 44, 69]. With results showing the formation of force chains in the DST regime in wet suspensions [8]. Experimental results show what could be a signature of force chains in the form of a positive normal stress difference at high volume fractions [4, 68]. Negative first normal stress differences have also been observed for lower volume fractions, which is expected for hydrodynamic interactions suggesting that more understanding is needed of the contribution of force chains to the normal

stress differences [68].

2.4 Conclusions

In this chapter we have outlined the basic rheological terms and concepts needed to describe suspension flow and discussed recent advances linking particle interactions to the rich rheology that suspensions can exhibit. We now have a framework to quantitatively capture bulk, steady-state flow, even though the precise nature of the interactions at small separations remains ambiguous. These contact details may prove relevant in extending these bulk models to describe time-dependent and local dynamics, where seemingly contradictory results leave a host of unanswered questions. In the next chapter we detail the experimental methods and rheological techniques employed in this work to tackle these outstanding challenges.

Chapter 3

Methods

This chapter describes the silica spheres and the suspensions preparation procedures and general rheological protocols used throughout the thesis. Specialised rheological techniques for characterising unstable time-dependent flows (Ch. 5) and local stresses (Ch. 6) are detailed within the relevant chapters. The bulk quantities of dry silica spheres purchased from Blue Helix Ltd. enabled us to carry out the work in this thesis (varying solvent composition, flow conditions etc.) using single batches of spheres with a given size. While this allowed us to avoid inherent batch-to-batch variation with repeated (smaller scale) in-house synthesis procedures, consistent protocals to thoroughly disperse the dry powder were essential.

3.1 Particle Sizing

Different methods were used to size the particles discussed in this thesis, this was especially important as part of the work in chapter 4 considers the variation of suspensions behaviour with particle size. SEM measurements were performed on a Zeiss Crossbeam 550 FIB-SEM, differential dynamics microscopy measurements were performed on were performed on a standard optical microscope with the data analysed using home-built code, and static light scattering measurements were made using a Beckman Coulter LS 13 320 Particle Size Analyzer.

SEM images show that our particles are spherical for all sizes, and by collating many images we were able to measure the average size and dispersity, which we

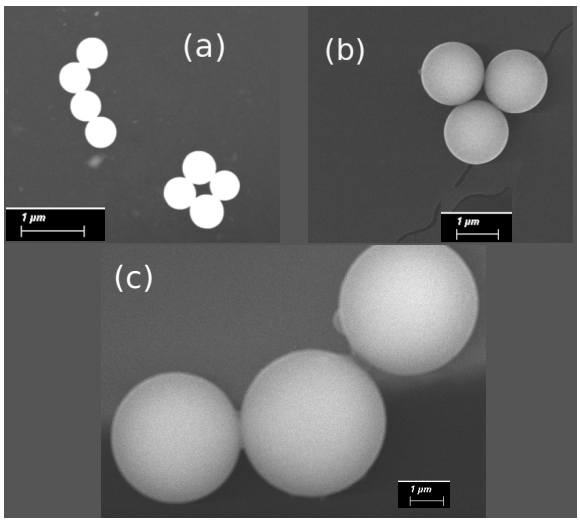

Figure 3.1 Images of different particles from batches with quoted radii 0.25 µm, 0.75 µm and 2 µm (figures (a), (b) and (c) respectively) taken using SEM.

represent as an error on the mean particle radius. We compare the radii measured from SEM to optical measurements (DDM and laser diffraction), where we find clear differences between the measurements using different methods (Fig. 3.1). The measurements of the sizes are generally consistent with the quoted values. The optical measurements deviate more from the quoted values especially for the two larger radii particles. For the case of DDM measurements of the diffusion for the $R = 0.75\,\mu\text{m}$ particles were performed close to a wall due to sedimentation leading to lower values of the diffusion coefficient and therefore larger estimates of the particle radius [100]. We note that the first value of R measured for the $R = 0.75\,\mu\text{m}$ particles, which will have been taken before sedimentation moved particles close to a wall, has a value $R \approx 0.75\,\mu\text{m}$. Conversely sedimentation in diffraction measurements of the particles referred to as $R = 2\,\mu\text{m}$ radius are likely underestimated as the larger particles sediment quicker and are therefore not measured. Therefore, we use our SEM measurements for the radius as the most accurate, although the estimation of error and therefore the polydispersity is limited due to the smaller sample size when using SEM.

Quoted R [µm]	SEM R [µm]	Optical R [µm]
0.25	0.25(2)	0.20(5) †
0.75	0.7(1)	1.0(1) †
2	2.1(1)	1.80(5) ††

Table 3.1 Mean particle size and errors measured using SEM images and optical methods along with the sizes quoted by the manufacturer. Optical measurements were done using microscopy and differential dynamic microscopy †, or light diffraction ††.

3.2 Cleaning, Dispersion, and Volume Fraction Measurement

Silica particles of three sizes (0.25 µm, 0.75 µm and 2 µm radius) were used in this work. The silica was washed repeatedly in distilled water adjusted to pH = 9 using NaOH. The elevated pH levels aid dispersion by increasing the surface charge on the silica and should also help remove residual surface contamination from the manufacturing process. To do this, dry silica powder was dispersed in the sodium hydroxide solution using hand mixing and probe sonication, the suspension was then allowed to sediment by centrifugation, then the supernatent was removed and the process was repeated.

The washed particles were then dispersed in 80 wt.% glycerol/water (G/W) solution with 0.2 mM Sodium fluoroscein salt for chapters 4 and 6 or 80 wt.% dimethyl sulfoxide/water (DMSO/W) solution for chapter 5. The fluoroscein sodium salt was added to give the potential for imaging of the suspensions using confocal microscopy, especially whilst performing BSM. Unfortunately we found that such 'dual imaging' did not give enough contrast for the particles to be seen, and the potential for imaging was unused otherwise. The two mixtures (DMSO/W and G/W) were used because the refractive indices (n = 1.441) matched that of the three silica sizes well, therefore reducing attractive forces. The addition of 0.2 mM sodium fluoroscein salt introduced a known minimum salt concentration to all suspensions.

Exchanging the solvent from the initial distilled water to the index matched G/W or DMSO/W fluids was achieved by repeated centrifugation and redispersion. The redispersion involved bath sonication, the use of a roller mixer, and hand mixing the sample with a metal spatula. Hand mixing with a metal spatula introduced very high local stress/shear to the sample, therefore breaking down

aggregates better. In general the larger particle suspensions were easier to disperse after centrifugation and also required less time to centrifuge down. This process was repeated at least 3 times, until good index matching was observed and no aggregates were visible. Good index matching indicated that the fluid used for washing had been completely replaced by the suspending fluid.

The $R = 2\,\mu m$ particle suspensions could be mostly dispersed using bath sonication and roller mixing, whereas the $R = 0.25\,\mu m$ particle suspensions required strong hand mixing with a metal spatula. The $R = 2\,\mu m$ particle suspensions sedimented quickly (on the order of hrs) which could lead to inaccurate volume fraction measurements if not properly redispersed before samples were prepared. The $R = 0.25\,\mu m$ particle suspensions showed almost no sedimentation, and measurements of samples taken months apart were found to be consistent with minimal redispersion.

The above methods were used to create stock samples containing $\approx 30\,mL$ of suspension. The volume fractions of these stock samples were measured by taking a small sample $\approx 3\,mL$ and weighing it, then repeatedly washing with distilled water (minimum 3 times) and then ethanol (minimum 3 times) and finally drying to obtain the dry particle weight. Care was taken to make sure the stock sample was properly dispersed before a sample was taken, and to not lose any particle mass in the process of cleaning. The repeated washing steps are necessary to remove the glycerol from the solvent before drying, as its low vapor pressure makes it difficult to remove via evaporation. By replacing the solvent with ethanol drying was significantly quicker and more complete. The samples were then dried in a vacuum oven at $40\,^{\circ}C$ for $4\,h$ and then weighed, to check the sample was dry, drying was repeated until the weight measurements were consistent to within $0.01\,g$. Though care was taken to measure the volume fraction of our stock samples, it is likely that unavoidable variation was introduced between stock samples [101].

Samples were prepared by mixing the stock solutions and the suspending fluid (or fluids) in calculated ratios to produce the desired volume fraction of particles and suspending fluid composition. The mixing ratios were calculated by weighing the sample taken from the stock sample, and calculating the fluid and solid volumes from the weight and the measured volume fraction. To accurately measure the volumes of the solid and fluid components we measured the densities of the fluids and solids. The density of the G/W and DMSO/W solutions were measured using a densitometer giving density values of $1.20\,g\,cm^{-3}$ and $1.09\,g\,cm^{-3}$ respectively.

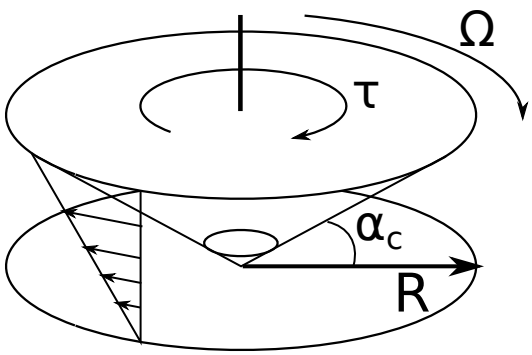

Figure 3.2 Cone-plate rheometer geometry. Cone radius R, rotation rate Ω, $\alpha_c = 1°$ is the cone angle (the angle is exaggerated in the schematic), and τ is the torque. The truncation gap is marked by the smaller ellipse.

The densities of the particles were found by measuring the density of samples of dilute suspensions of known mass fraction of silica with a value of $1.97\,\mathrm{g\,cm^{-3}}$, $2.00\,\mathrm{g\,cm^{-3}}$ and $2.07\,\mathrm{g\,cm^{-3}}$ for the 0.25 µm, 0.75 µm and 2 µm radius particles respectively.

3.3 Rheological Measurements

In chapter 2 we outlined the basic principles of rheology considering an idealised simple shear flow between infinite flat plates. In practice, rheological characterisation is typically done with a rheometer, where rotational motion in some set geometry can at least achieve a close approximation of simple shear flow. A rotational rheometer accesses the torque τ and the rotation rate Ω. From these two quantities the shear rate $\dot{\gamma}$ and stress σ can be calculated using the flow geometry. Rotational rheometers are conventionally known as stress-controlled or rate-controlled, depending on which quantity is applied and which is measured, though modern rheometers offer to operate in either mode using a fast feedback loop to set the measured variable.

In this work we generally use a stress-controlled rheometer (Anton Paar MCR301) with a cone-plate geometry unless otherwise specified. The key feature of the cone plate sketched in figure 3.2, is that the linear increase in gap height with radius r cancels the linear velocity increase

$$\dot{\gamma} = \frac{\Omega r}{h} = \frac{\Omega r}{r \tan \alpha_c}, \tag{3.1}$$

so both the shear rate and shear stress are constant across the tool independent of position. Though in reality cone-plate tools include a truncation gap, to avoid contact between the tool and the bottom plate, where the shear rate and shear stress vary radially. Truncation gaps are very small, and have a negligible affect on the rheology. The size of particles measured in suspensions is limited by the small truncation gap, obviously the particles must be smaller than the truncation gap, and in general more than ≈ 10 particles should be able to fit in the truncation gap. The truncation gap in our setup is $h_t = 48\,\mu\text{m}$, which for our $R = 2\,\mu\text{m}$ particles is pushing the limit of the geometry. For our work on shear thickening suspensions there are added benefits to using a cone-plate rheometer tool of this geometry (12.5 mm radius) as it allows for better comparison to prior work on similar systems [20, 27, 68], and requires relatively small sample volumes ($\approx 0.1\,\text{mL}$). The absence of significant stress/shear rate gradients should also prevent shear-induced particles migration, which could distort our measured rheology.

The MCR301 rheometer works by rotating the cone-tool, which is positioned on top of the sample. The apparent stress σ can be calculated from the torque τ and the area of the plates as

$$\sigma = \frac{3\tau}{2\pi R^3}. \tag{3.2}$$

From equation 3.1, we calculate the shear rate of the system as

$$\dot{\gamma} = \frac{\Omega}{\tan(\alpha_c)}. \tag{3.3}$$

The analysis here considers a perfectly aligned cone and plate, though in practice there will be a small degree of misalignment. We will discuss the effect of misalignment of the cone-tool in Ch. 6, but note that for a misaligned system the stress and shear rate given by equations 3.2 and 3.3 (and reported by the rheometer) should be considered 'apparent' quantities σ_{App} and $\dot{\gamma}_{\text{App}}$. In reality the stress and shear rate vary spatially across the geometry for a misaligned system [102]. The viscosity is then given by $\eta = \sigma/\dot{\gamma}$. Measurement of the viscosity η can be done by either controlling the shear rate $\dot{\gamma}$ or the applied shear stress σ. Although this distinction does not matter for Newtonian fluids (where η is independent of both σ and $\dot{\gamma}$), it is important for fluids which have a stress or shear rate dependent viscosities.

3.3.1 Measurement Protocols and Conditions

To measure different properties or different fluids, different measurement protocols were required. For shear thickening fluids a stress was applied, increasing logarithmically to capture the full range of shear thickening; the upper stress plateau was rarely fully observed either due to shear thinning effects at high stresses, or limits to the rotation rate of the rheometer tool due to sample ejection. For yield stress fluids a shear rate was applied, increasing logarithmically to capture the yield stress region, where there is a discontinuity in the stress. To allow the measurement to reach steady state we allow the accumulated strain to reach ≈ 1, though this value is not reached for measurements at particularly low shear rates. The steady state value is the measured by averaging over the last half of the measurement time.

The experiment protocol consisted first of levelling the bottom plate by adjusting the leveling screws whilst measuring the vertical displacement at a fixed radius from the centre. The sample was placed on the bottom plate of the rheometer by either pouring a small volume, or using a spatula if the sample was very viscous. The top rheometer tool was then lowered to slightly above the measuring position and the edge of the sample was trimmed using a plastic spatula. The top rheometer tool was then moved to the measuring position, where the gap height at the truncation gap was 48 µm. To limit drying of the sample the suspending fluid was pipetted around the sample, but not in contact with the sample. A temperature controlled casing was then lowered over the sample, and the tool lowered to the measuring position. To change samples the bottom plate was cleaned with distilled water and then ethanol to aid drying.

Chapter 4

Particle Interactions and the Shear Thickening Onset in Suspensions of Silica Particles

As discussed in chapter 2, the onset of shear thickening, where a suspension's viscosity begins to rise considerably, is related to a characteristic stress scale σ^*. In the current friction-driven understanding of shear thickening, σ^* is determined by the repulsive inter-particle forces (e.g. electrostatic or steric interactions) [80], which compete against the shear forces pushing particles into contact. Despite this level of understanding, it is still not possible to quantitatively predict σ^* for a given shear thickening suspension. This poses challenges in industrial suspensions, where even small changes in the suspending fluid or the particle properties can result in large unexpected changes in the suspension rheology.

In this chapter we examine the rheology of suspensions of silica particles, a standard model system for shear thickening. We vary both the particle size and fluid composition, and we focus particularly on silica suspended in aqueous fluid whilst varying the ionic strength of the fluid. Varying the ionic strength allows us to systematically vary the strength of the repulsive electrostatic forces.

4.1 Rheology of Aqueous Silica Suspensions

Here we investigate shear thickening in aqueous silica suspensions, varying both the particle size and the ionic strength to investigate the size dependence $\sigma^*(R)$, of a charge stabilized system using well characterised and consistently prepared suspensions (see Ch. 3 for details). In particular, we highlight that for each given size all the suspensions were prepared from a single (kilogram scale) batch of dry particles.

To systematically measure the scaling of the onset stress of shear thickening of silica suspensions we attempt to remove variation between samples. We do this by using particles from the same supplier (Blue Helix) suspended in 80 wt.% glycerol/water (G/W). The particles were characterised by AFM and SEM imaging, light scattering, and differential dynamic microscopy to determine their size dispersity and surface roughness (see Ch. 3 for sizing). The size dispersity was discussed in chapter 3, and the AFM measurements will be discussed later in this chapter.

4.1.1 Sample Preparation and Characterisation

The ionic strengths of samples were adjusted by diluting a stock sample to $\phi \approx 0.5$ with a mixture of the stock suspending fluid (G/W with 0.2 mM fluoroscein sodium salt), and a high ionic strength G/W solution (120 mM and 4000 mM LiCl). To characterise the rheology of a given suspension sample, we performed multiple (minimum of 6) ascending and descending sweeps varying the applied stress σ while measuring the viscosity $\eta = \sigma\dot{\gamma}$. The repeated stress sweeps enabled us to verify that the measured flow curves were reversible and reflected the steady-state suspension rheology.

Some samples showed time-dependant drift in the viscosity, appearing both in low-stress (un-thickened) and high-stress (shear-thickened) regions of the flow curves. Given that the viscosity of our G/W mixture is highly sensitive to small changes in the temperature and the precise glycerol content, we attribute this drift to slow evaporation/absorption and sample temperature changes. We found that this drift can be accounted for through empirical linear fits to $\eta(t) = \eta_{\min} + \dot{\eta}t$

for values of η on the low stress plateau (Fig. 4.1), which we normalise

$$\eta_n(t) = \frac{\eta(t)}{\eta_{\min}} = 1 + \frac{\dot{\eta}}{\eta_{\min}} t. \tag{4.1}$$

We use corrected values of $\eta(t)/\eta_n(t)$ for all t when reporting the relative suspensions viscosity $\eta_r = \eta/\eta_f$.

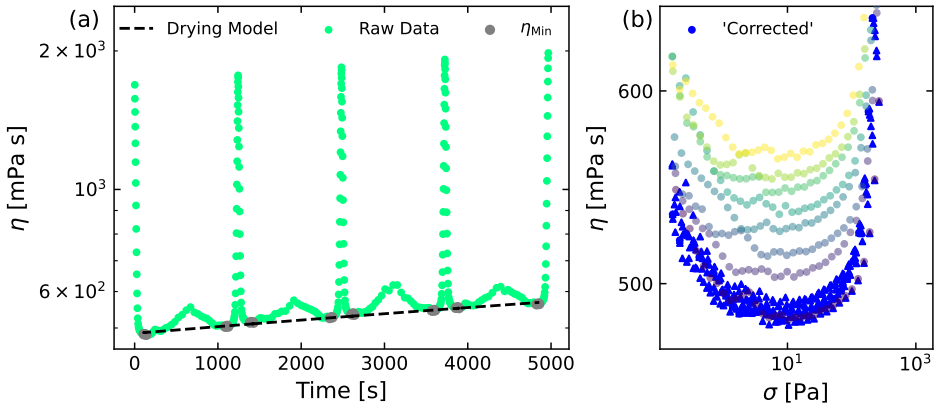

Figure 4.1 Repeated stress sweep measurements of $\eta(\sigma)$ against the time the measurement was taken. (a) A linear model to predict variation of the solvent viscosity with Data points used to fit the model (grey) and full data set (green). (b) time dependent data (multicolored circles) with 'fixed' data (blue triangles).

4.1.2 Defining the Shear Thickening Onset

To measure the onset stress of shear thickening we fit a WC-type model to our rheology data, which is described by equations 2.31, 2.29 and 2.11, which were introduced in Sec. 2.2.6. This was done as apposed to setting a simple subjective threshold for the viscosity increase [8, 103], to provide a consistent definition of σ^* that could be compared to other recent experimental work [20, 68] and numerical simulation results [21]. The equations used in our WC-type model are

$$f = \exp\left(-\left(\frac{\sigma^*}{\sigma}\right)^{\beta}\right), \tag{2.31}$$

$$\phi_J = f\phi_M + (1-f)\phi_0, \tag{2.29}$$

$$\eta_r = A\left(1 - \frac{\phi}{\phi_J}\right)^{-2}. \tag{2.11}$$

We fitted the the model to flow curves produced at various volume fractions (Fig.

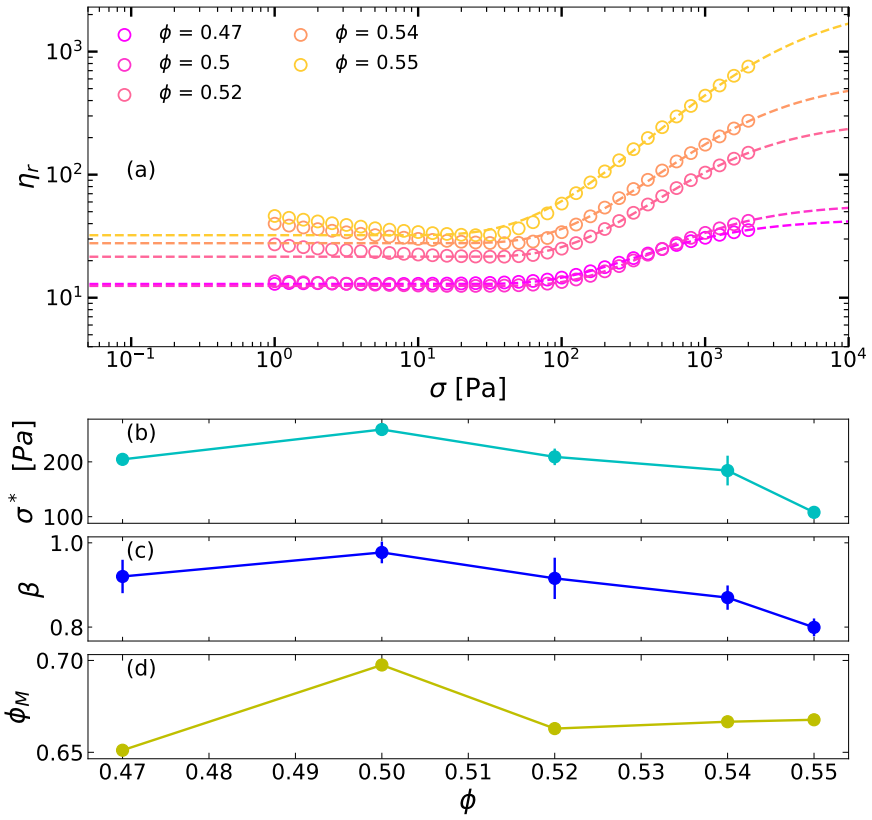

Figure 4.2 (a) WC model (Eqs. 2.11, 2.31, 2.29) fits (dashed lines) to selected flow curves (circles) at indicated ϕ (legend). (b) Variation in $\sigma^*(\phi)$ at fixed I.

4.2), fixing $A = 1$ as done in previous work fitting WC-type models [20, 68, 104]. For this, and subsequent data in this chapter, we fit the four parameters σ^*, β, ϕ_M, and ϕ_0 individually. The expected low shear plateaus are not visible due to shear thinning; we account for this by taking the minimum viscosity as the value for the low shear plateau viscosity. From this viscosity we calculate ϕ_0 using equation 2.11 (with $\phi_J = \phi_0$) so that the minimum stress is matched by the fit, this also avoids any coupling between ϕ_M and ϕ_0 when fitting these two parameters simultaneously. We fit the other three parameters using a least squares minimisation method. There is strong correlation in the fitting between β and ϕ_M ($\mathrm{Corr}(\phi_\mathrm{M}, \beta) \approx 0.9$), and strong correlation between β and σ^* at high ϕ (for $\phi = 0.54$, $\mathrm{Corr}(\sigma^*, \beta) = 0.9$); such correlations make it difficult to speculate over what change in the system caused the change in the parameters. The fits show good agreement with the flow curve data (Fig. 4.2), though the model does not fit the shear thinning at low stresses.

Our theoretical prediction of the DLVO interparticle forces between two spheres

suggests that σ^* is only dependent on the interparticle repulsive force F^*, and therefore should not depend on ϕ. This assumes that particle-particle repulsion at close separation is not affected by the presence of nearby particles, and this would be a reasonable assumption in a steric system where repulsive interactions have a finite range. Unfortunately the system we have considered here is controlled by DLVO forces, and it is possible that the ionic layers of nearby particles will effect the local potential between two particles at high volume fractions. This is especially true for the 0.25 µm radius particles, where the Debye length is similar to the particle radius at low ionic strengths. Our results show σ^* varies with volume fraction peaking at $\phi = 0.50$ and then decreasing at higher volume fractions, before dropping dramatically when $\phi = 0.55$. As we will see later, the variation in σ^* with size and ionic strength is more significant than the variation with volume fraction, therefore we only consider a single volume fraction ($\phi \approx 0.5$) throughout the rest of this chapter. We also limit the strength of the correlation between σ^* and β by using a lower volume fraction.

We note that fitted values of σ^* do not depend on the precise details of how we account for the variation in the high- and low-shear suspension viscosities (e.g. fixing A and allowing ϕ_0 to vary or fixing ϕ_0 and allowing A to vary). As the Wyart-Cates model only acts to describe as long as the model has sufficient freedom to match these high- and low-shear values.

For values where the repulsive force has become weaker than the attractive DLVO force at almost all separations and the suspension has become attractive, we calculate ϕ_M at high stresses using equation 2.11, with $\phi_J = \phi_M$, and the viscosity at the maximum apparent stress.

As noted above, we expect σ^* to depend both on the particle size and the ionic strength, but it is less clear what should be expected for β, ϕ_0, and ϕ_M. As discussed in Ch. 2, a simple exponential $f(\sigma)$ (with $\beta = 1$) would be expected for mono-disperse particles with uniform interactions [20, 69], though stretched distributions (with $\beta < 1$) can be rationalised by variation across the sample in particle size and/or interaction strength, giving a distribution of 'local' onset stresses [70]. Simulations have shown that the frictional jamming point ϕ_M decreases as the effective static friction coefficient μ increases [8, 84, 105]. In simulations of frictional mono-disperse sphere ϕ_M initially remains close to the frictionless value $\phi_{\mathrm{RCP}} \approx 0.64$ for $\mu \lesssim 0.1$, then decreases to ≈ 0.56 in the high friction limit $\mu \gtrsim 1$ [67]. ϕ_0 should be independent of the particle properties, and should be similar to the limit of random close packing $\phi \approx 0.64$ for all suspensions.

Though our silica particles are all synthesised using the same Stöber chemistry in large batches, we might expect that variation in the surface properties will result in some variation in ϕ_M and β between the different sizes. We would not expect ϕ_M and β to depend directly on the magnitude of the interparticle interactions, and so would not expect them to vary with ionic strength.

4.2 From Thickening to Thinning: Exploring the Role of the Ionic Strength for Various Particle Sizes

We begin by examining the rheology of our $R = 0.75\,\mu\text{m}$ silica spheres varying the fluid ionic strength I. While particles of this size are generally considered colloidal, the characteristic Brownian stress is only $k_\text{B}T/R^3 \approx 0.01\,\text{Pa}$ so that Brownian contributions to the rheology are minimal over the range of stresses probed here ($\approx 1\,\text{Pa}$ to a few $1000\,\text{Pa}$). Steady state flow curves $\eta_r(\sigma)$ at low to moderate ionic strengths ($1\,\text{mM} \leq I \leq 300\,\text{mM}$) show typical shear thickening behaviour (Fig. 4.3). Over this range of ionic strengths the Debye-Hückel length of the system varies approximately from 30 nm to 0.6 nm.

We note that we limited the maximum applied stress to $4000\,\text{Pa}$, as beyond this point edge instabilities would fracture and eject the sample from the rheometer geometry, limiting our ability to fully resolve the high stress plateau. While there is no clear trend in the magnitude of either the high or low shear viscosity with increasing I, aside from small variations due to differences in the prepared values of ϕ, there is a clear decrease in the thickening onset as I increases.

Fitting these flow curves as before, we find similar values for $\sigma^*(I)$ and the other Wyart-Cates fitting parameters. Surprisingly, while we might expect stronger screening and a reduction in the interparticle repulsion with the multivalent salt, we instead find a slightly lower value of σ^* at low I in the suspensions with only LiCl. ϕ_M and β are generally similar independent of the addition of sodium fluoroscein salt, though there is a stronger trend in decreasing β with increasing I for the samples with no sodium fluoroscein salt.

Fitting the shear thickening flow curves ($I \leq 159\,\text{mM}$) to the Wyart-Cates type model described in the previous section (Fig. 4.4), we can detail how the four

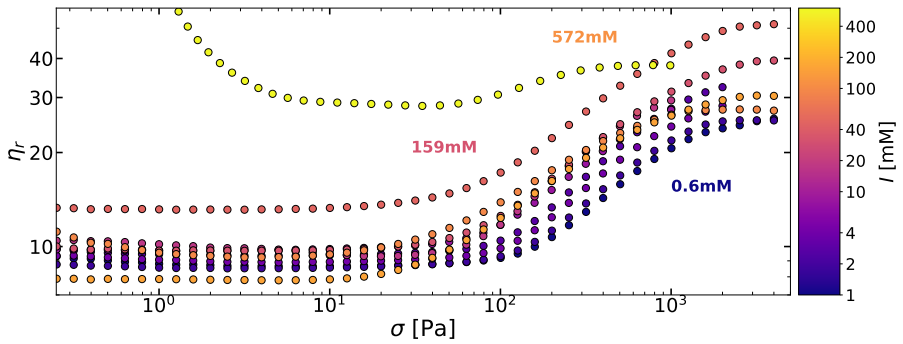

Figure 4.3 Relative viscosity $\eta_r(\sigma)$ for suspensions of $R = 0.75\,\mu$m silica spheres at varying ionic strength I (indicated by the color scale). The volume fraction $\phi \approx 0.5$ varied slightly from sample to sample, reflected in the variations in the low-shear viscosity.

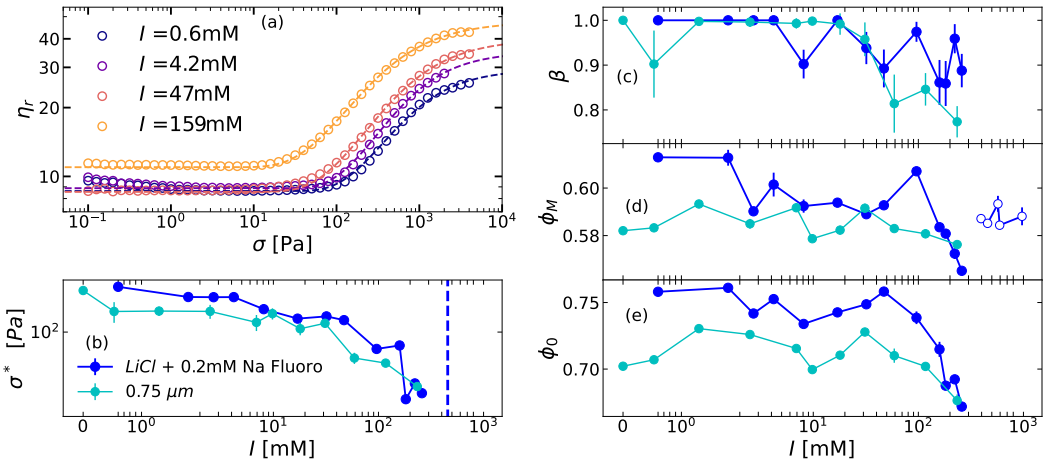

Figure 4.4 (a) WC model (Eqs. 2.31, 2.11, 2.29) fits (dashed lines) to selected flow curves from figure 4.3 (solid circles) at indicated ionic strengths I.(b)-(e) Resulting fitting parameters $\sigma^*(I)$, $\beta(I)$, $\phi_M(I)$, and $\phi_0(I)$ for the full set of shear thickening curves from figure 4.3 (filled dark blue circles), and (d) ϕ_M values calculated for yield stress samples (hollow dark blue circles), and for otherwise identical shear thickening suspensions without fluoroscein sodium salt dye (light blue circles).

fitting parameters (σ^*, β, ϕ_M, and ϕ_0) vary with the ionic strength. These fitting results confirm the qualitative trends in the flow curves. The onset stress σ^* decreases by approximately an order of magnitude, before the low shear plateau eventually gives way to shear thinning or yield stress behaviour. There is no clear trend in ϕ_M suggesting that the effective static friction between particles is independent of the particle repulsion/attraction. There is perhaps a weak decrease in the stretching exponent $\beta(I)$, though this is difficult to resolve clearly. There may be a drop in ϕ_0 at high I, this drop is most clear for the samples containing fluoroscein sodium salt.

We now turn to the rheology of smaller $R = 0.25\,\mu\text{m}$, and larger $R = 2\,\mu\text{m}$ silica spheres. The Brownian stress scale $k_\text{B}T/R^3 \approx 0.3\,\text{Pa}$ for the smaller colloidal particles is now comparable to the stress range accessed in our flow curves $\eta_r(\sigma)$. Comparing flow curves varying ionic strength I (Fig. 4.5(b)), at high stresses we see similar trends in the shear thickening behaviour that we saw with the $R = 0.75\,\mu\text{m}$ spheres, with the thickening onset shifting lower with increasing I until the thickening largely disappears around $I \approx 300\,\text{mM}$, notably lower than the two larger particle sizes.

The shear thickening flow curves for the larger silica sphere suspensions show minimal shear thinning at low stresses, though the high-shear viscosity plateau is lost (Fig. 4.5(a)). Attempts to increase the applied stress beyond 4000 Pa lead to sudden drop in the viscosity, after which the flow curves were no longer reversible upon ascending and descending stress sweeps. This behaviour is highly suggestive of fracture and instabilities at the edge, therefore high stresses were avoided. As with the suspensions of smaller particles there is qualitative trend in decreasing onset stress with increasing ionic strength. There appears to be a consistent decrease in the high-shear viscosity, but this trend does not appear to be robust and it does not continue into the shear thinning/yield stress regime (Fig. 4.5(a)).

A selection of fits from the 0.25 µm radius silica particles are shown in figure 4.6, where the divergence from the low viscosity plateau due to shear thinning can be seen. The model captures the shear thickening region, including the high stress plateau. Parameters of the fitting are shown in figure 4.6, again $\sigma^*(I)$ clearly decreases with increasing I.

At higher ionic strengths ($I \geq 300\,\text{mM}$) there is dramatic change in the rheology for all particle size suspensions, as the low-shear Newtonian plateau disappears and the suspensions instead shear thin at low σ suggesting a finite

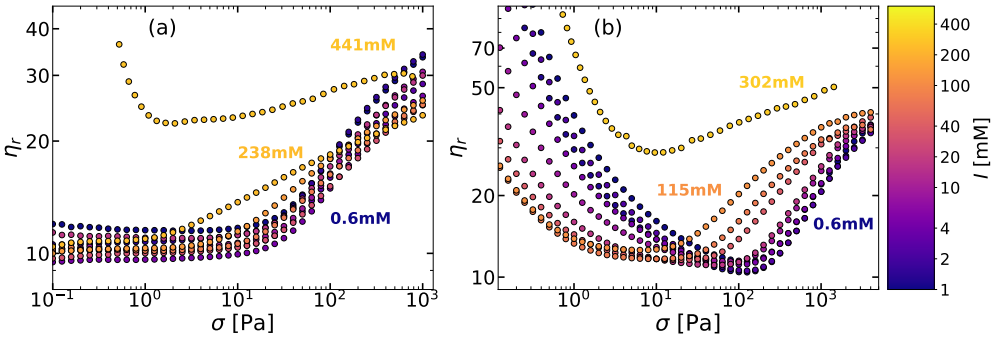

Figure 4.5 Relative viscosity $\eta_r(\sigma)$ for suspensions of (a) $R = 2\,\mu m$ and (b) $R = 0.25\,\mu m$ silica spheres at varying ionic strength I (indicated by the color scale). The volume fraction $\phi \approx 0.5$ varied slightly from sample to sample, reflected in the variations in the low-shear viscosity.

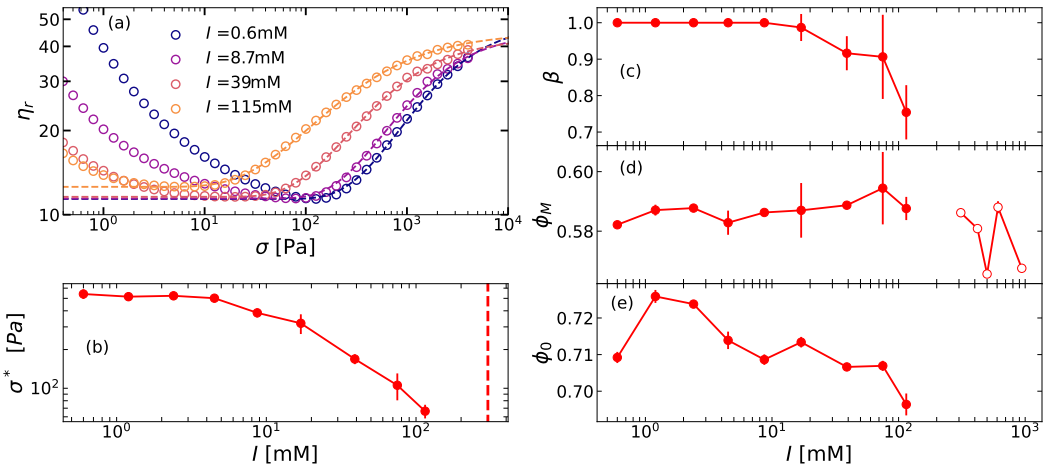

Figure 4.6 (a) WC model (Eqs. 2.11, 2.31, 2.29) fits (dashed lines) to selected flow curves from figure 4.5 (solid circles) at indicated ionic strengths I.(b)-(e) Resulting fitting parameters $\sigma^*(I)$, $\beta(I)$, $\phi_M(I)$, and $\phi_0(I)$ at varying I for the full set of shear thickening curves from figure 4.5(a) (filled red circles), (d) as well as ϕ_M calculated for yield stress samples (hollow red circles).

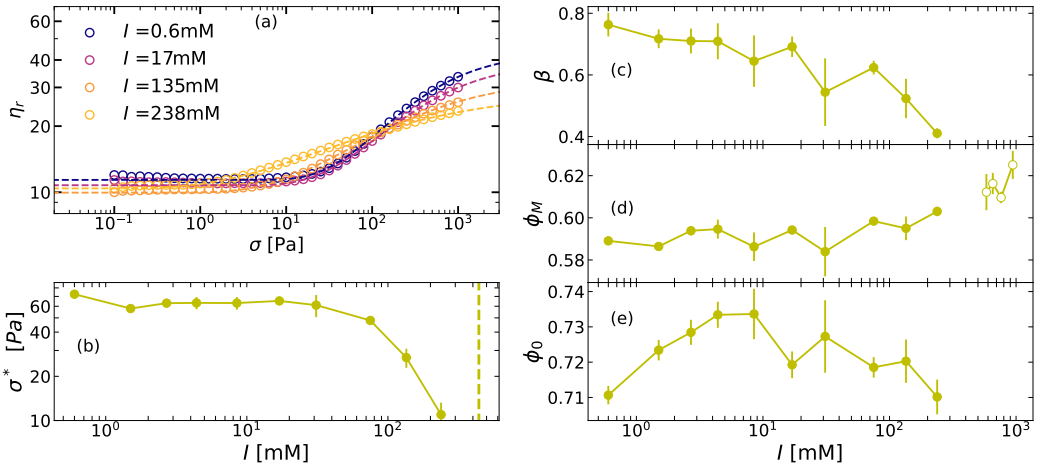

Figure 4.7 (a) WC model (Eqs. 2.11, 2.31, 2.29) fits (dashed lines) to selected flow curves from figure 4.5 (solid circles) at indicated ionic strengths I.(b)-(e) Resulting fitting parameters $\sigma^*(I)$, $\beta(I)$, $\phi_M(I)$, and $\phi_0(I)$ at varying I for the full set of shear thickening curves from figure 4.5(b) (filled yellow circles), (d) as well as ϕ_M calculated for yield stress samples (hollow yellow circles).

yield stress (Figs. 4.3 and 4.5(a,b)). As discussed in Ch. 2, such a change in rheology is consistent with a transition from repulsive to attractive particle interactions. Such a transition is expected in charge stabilised systems, as the ionic screening eventually suppresses the electrostatic repulsion sufficiently leaving only attractive van der Waals forces. We note that it is difficult to differentiate the effects of pure attraction [23] from adhesive contacts which also constrain rolling [25, 90, 91].

Figure 4.7 show a selection of fits for the WC-type model, and the resulting parameters as a function of I. The fits shown in figure 4.7 show two distinct low viscosity plateaus, this is a result of the two higher salt concentrations having lower volume fractions closer to 0.49 (as apposed to 0.5). Both figures again show the trend in decreasing onset stress of shear thickening σ^* with increasing I.

The suspension appears to maintain some shear thickening behaviour even when exhibiting a yield stress (Figs. 4.3 and 4.5(a,b)). Although the persistence of thickening at high stresses is consistent with previous results looking attractive interactions in shear thickening suspensions [23, 89, 106], our results do not show increasing shear thinning at low stresses. This is due to the fact that these previous results considered an increasing attractive force, as opposed to the decreasing repulsive force we see here, which is the effect of increasing the ionic

strength in an electrostatically repulsive suspension.

4.2.1 Connecting Bulk Rheology to Particle Interactions and Surface Properties

Our detailed characterisation of the shear thickening onset in silica suspensions, varying both the particle size and ionic strength, allows us to revisit the connection between particle interactions and the bulk rheological value σ^*, which is part of our friction-driven understanding of shear thickening. For discussion of the variation of parameters with size we include results from suspensions of $R = 0.75\,\mu\text{m}$ silica spheres containing no fluoroscein sodium salt (LiCl only).

Recall from Ch. 2 that the thickening onset σ^* should be determined by some characteristic repulsive force F^* which must be overcome to form frictional contacts, so that dimensional analysis gives

$$\sigma^* \propto \frac{F^*}{R^2}. \tag{4.2}$$

From the Derjaguin approximation, we should expect that any repulsive interactions arising from a potential, such as electrostatic forces, should scale as $F \propto WR$ with W as the surface free energy density for equivalent flat plates. This would imply

$$\sigma^* \propto \frac{W^*}{R} \tag{4.3}$$

with the critical free surface energy $W^* = W^*(I)$ dependant on the particle and fluid composition only.

For all three of our particle sizes the qualitative form of $\sigma^*(I)$ is similar, with $\sigma^*(I)$ nearly constant or only weakly decreasing for $I \lesssim 10\,\text{mM}$, followed by more rapid decrease as I increases further until a transition to shear thinning yield stress behaviour for $I \gtrsim I^\dagger$ (Fig. 4.8(a)). This is consistent with DLVO-like interactions, with electrostatic repulsion giving way to van der Waals attraction as the degree of electrostatic screening increases. We find that our expected $\sigma^* \propto R^{-1}$ scaling reasonably collapses our results for $I \lesssim 10\,\text{mM}$, where σ^* only weakly varies with I, but fails at higher I where $\sigma^*(I)$ is rapidly decreasing (Fig. 4.8(b)). We note that the $\sigma^* \propto R^{-2}$ scaling observed in many sterically stabilised systems [20, 107, 108] fails dramatically here at all values of I (Fig. 4.8(c)).

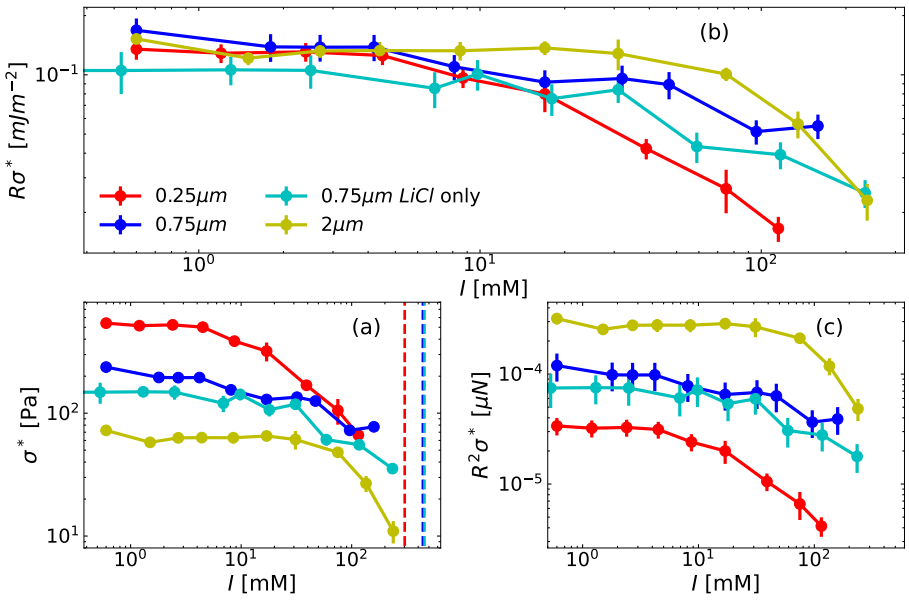

Figure 4.8 Suspensions of particles of three different radii 0.25 µm, 0.75 µm and 2 µm, and were suspended with $\phi \sim 0.5$. (a) The onset stress of shear thickening $\sigma^*(I)$, found by fitting a WC-type model to shear thickening flow curves of silica particles suspensions. The dashed lines represent the lowest ionic strength at which shear thinning/yield stress behaviour was observed. (b) $\sigma^*(I)R$ where R is the particle radius. (c) $\sigma^*(I)R^2$.

The success of the $\sigma^* \propto R^{-1}$ scaling at low I suggests that in this regime the repulsive interactions impeding frictional contact formation can indeed be described by a surface free energy W, which could in principle be directly measured from force spectroscopy using either an atomic force microscope or surface force apparatus. However, the breakdown of this scaling at high I indicates more complex surface-specific effects between different sizes.

The deviation from the $\sigma^* \propto R^{-1}$ scaling is most evident in the smaller $R = 0.25$ µm spheres. With these spheres we also find a lower $I^\dagger$ where the interactions change from repulsive to attractive.

A detailed understanding of this scaling breakdown would require direct measurement of the particle interactions for each of the different sized spheres at varying I, however we can hypothesize a possible explanation. For DLVO-like interactions, the net interaction force is the sum of repulsive and attractive components $F(h) = F_r(h, I) - |F_a(h)|$, with the electrostatic repulsive force varying with I while the van der Waals attraction is independent of I. Assuming static friction initiates at contact ($h = 0$), then $F^* = F_r(0, I) - |F_a(0)|$. The form

of our $\sigma^*(I)$ curves suggest that at low I the repulsive force dominate $F_r \gg |F_a|$ so that $F^* \approx F_r(0, I)$, while F^*, and hence the onset stress, vanishes around $I^\dagger$ as these forces become comparable $F_r(0, I^\dagger) \approx F_a(0)$.

With conventional smooth-sphere DLVO interactions both F_r and F_a are proportional to R, so we should always have $\sigma^* \propto R^{-1}$ provided that the particle surface properties (e.g. charge density, Hamaker constant) are size independent. A reduction in the surface charge density should uniformly reduce the electrostatic forces F_r, giving uniformly lower values of σ^* at all I, but stronger attractive forces could alter the shape of σ^* as $I \to I^\dagger$ while leaving the low I regime where $F^* \approx F_r(0, I)$ is unaffected.

The apparent enhanced attraction between small spheres (Fig. 4.8(b)) suggests a larger effective Hamaker constant. This is difficult to rationalise for smooth spheres where the Hamaker constant is determined solely by the particle and fluid dielectric properties, which should be roughly uniform across the different sizes. However it has been shown that surface roughness can dramatically effect van der Waals forces [16, 109], giving rougher spheres a lower effective Hamaker constant. But AFM measurements suggest that the $R = 2\,\mu\text{m}$ particles are significantly rougher than the other two particle sizes, which would suggest they should have a lower Hamaker constant (Fig. 4.9). Notably the ionic strength for a Debye-Hückel length at 2 nm is approximately 30 mM, which is the ionic strength at which σ^* begins to noticeably decrease, and where σ^* begins to diverge for the different particle sizes. Although if the strength of the attractive force is more dependent on the relative roughness, then relative roughness may explain the observed divergence, as our smallest particles are the roughest relative to their radius.

If differences in roughness is not the reason for the divergence in the onset stress, a possible resolution lies in the Brownian nature of our smallest spheres. Calculations [109], and measurements [16] of van der Waals interactions between rough surfaces generally consider a static surface orientation so that the attraction is limited by the first asperity-asperity contact [109]. However translational and Brownian diffusion should allow particles to effectively sample differing surface orientations and find local attractive minima.

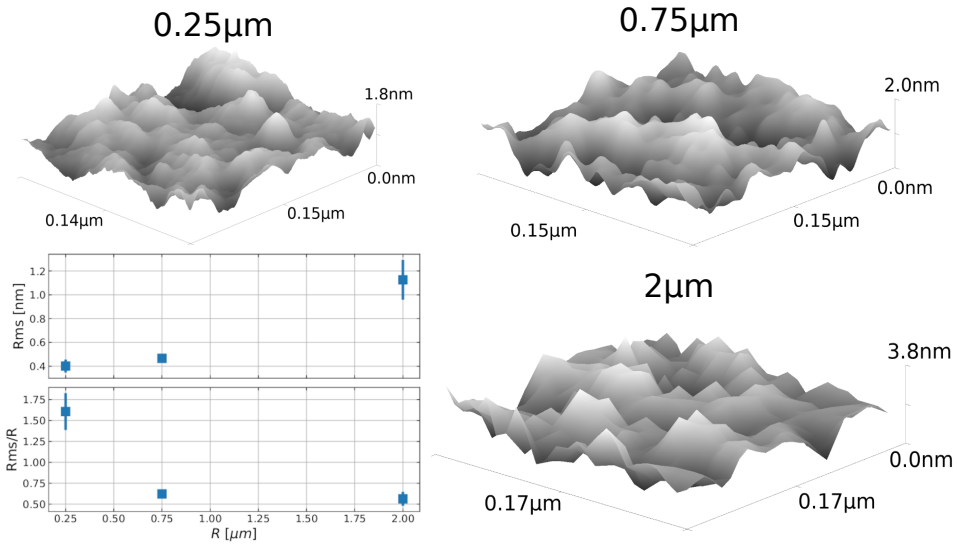

Figure 4.9 Surface profiles, route mean square roughness (Rms) values and relative roughness Rms/R for three different silica sphere sizes. Rms values were taken for similar area sizes of the surface profiles and averaged. Data for the two smallest sizes uses multiple different particles.

Further Effects of Particle Size on Bulk Rheology

In contrast to our expectations, the stretching exponent β appears to vary weakly with I, and differs dramatically for our largest 2 µm spheres (Fig. 4.10(a)). For our smaller 0.25 µm and 0.75 µm spheres $\beta \approx 1$ for low I, as expected for uniform monodisperse spheres, but decreases slightly as $I \to I^{\dagger}$. For the 2 µm spheres we instead have $\beta \approx 0.75$ for low I, further decreasing below 0.5 close to $I^{\dagger}$. As previously described, stretching exponents $\beta < 1$ describing a more gradual thickening transition, can result from variations in particle size or interaction strength that give rise to a distribution. Obtaining such low values of β through polydispersity alone typically requires extremely broad size distributions (orders of magnitude size variations) [70], and so is unlikely here, where we see no evidence of such large variation in the particle size (Ch. 3). This suggests that the lower values of β reflect a distribution of interaction forces, so that the force F^* needed to initiate contact varies from contact to contact. As I increases, the electrostatic screening length decreases, so that one might expect surface heterogeneity to have a more pronounced effect at higher I. The pronounced difference between the 2 µm spheres and the smaller sizes is surprising, but could be related to their increase surface roughness.

As discussed in section 4.1.2, we did not expect the jamming volume fraction

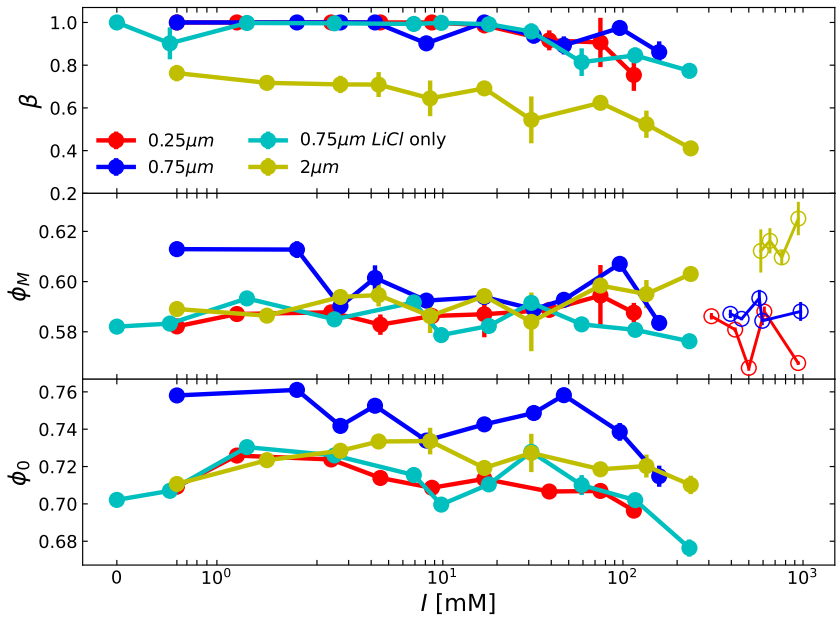

Figure 4.10 Fitting parameters found for the WC-type model for suspensions of silica particles at various sizes (legend) and ionic strengths I with $\phi \approx 0.5$ found for shear thickening suspensions with $I < I^\dagger$ (filled symbols). (a) $\beta(I)$ the scaling exponent, (b) $\phi_M(I)$ the high shear jamming volume fraction, and (c) ϕ_0 the low shear jamming volume fraction. (b) hollow symbols are for samples $I > I^\dagger$ where samples exhibit yield-stresses (in this case ϕ_M is calculated from the high stress viscosity).

ϕ_M or the stretching exponent β to vary with I or R. This generally holds for ϕ_M, which generally varies between 0.58 and 0.6 without any robust trend with varying size or ionic strength even beyond $I^\dagger$ where the particle interactions become attractive (Fig. 4.10(b)). While accurately determining absolute volume fractions is challenging [101], these values are consistent with simulation results for spheres in the high-friction ($\mu \gtrsim 1$) limit [8, 21, 69]. This possibly explains why we do not see a clear difference in ϕ_M with the measurably rougher 2 µm spheres, as further increasing μ in this limit results in only a minor increase in ϕ_M.

There is a clear deviation in the value of ϕ_0 for the $R = 0.75$ µm size particle suspensions, but no clear trend in size beyond that (Fig. 4.10(c)). This could easily be a result of an inaccurate measurement of ϕ for the stock solution used for this data set [101].

4.3 Effect of Ionic Strength on Shear Thinning of Near Brownian Suspensions

The $R = 0.25\,\mu m$ particle suspensions show strong shear thinning at low stresses (Fig. 4.5(a)), which is strongly affected by the increasing ionic strength. The suspensions show weaker shear thinning with increasing ionic strength (Fig. 4.11). At low I the particle interactions are dominated by electrostatic repulsion, the range of which is related to the Debye length, which decreases with increasing ionic strength I.

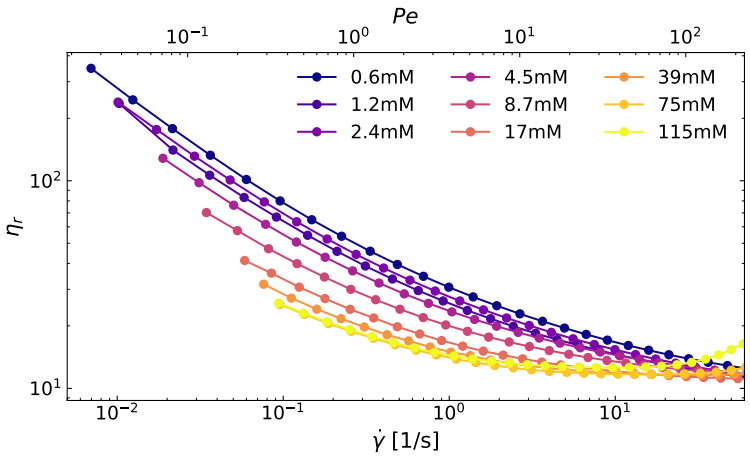

Figure 4.11 Relative viscosity $\eta_r(\dot{\gamma})$ for suspensions of 0.25 µm silica spheres at varying ionic strength I (legend). The graph shows the same flow curves from figure 4.5(a) at low shear-rates.

We can quantify the contribution of Brownian effects, which relate to the shear thinning seen here, by considering the Péclet number (Eq.2.12). Pe is well above 1 when shear thickening begins, suggesting that the shear thickening is not affected by the shear thinning present. As the change in the Péclet number is only dependent on the shear rate and particle size, there must be a contribution to the shear thinning that is affected by the ionic strength.

The decrease in the strength of the shear thinning is a result of the changing range of the electrostatic repulsion [110]. If we consider the particle as having some extended radius due to the range of the electrostatic repulsion $R_{\text{ext}} = R + \lambda_h$ (Eq. 2.25), then a smaller Debye length λ_h means a smaller R_{ext} and therefore a smaller ϕ_{eff}, which will be further below the glass transition leading to a lower low-shear viscosity. Between $I = 75\,\text{mM}$ and $I = 115\,\text{mM}$ the increasing ionic strength does not weaken the thinning further, because the electrostatic repulsion

has become so short ranged that the thinning is dominated by Brownian effects.

4.4 Behaviour of Suspensions Close to the Transition to Attractive Interactions

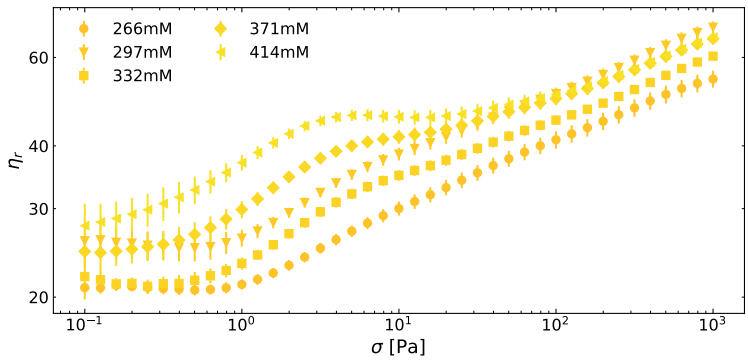

Figure 4.12 Relative viscosity $\eta_r(\sigma)$ for suspensions of $R = 2\,\mu\text{m}$ silica spheres at ionic strengths just below the start of shear thinning behaviour I (indicated by the legend). The volume fraction $\phi \approx 0.5$ varied slightly from sample to sample.

At I close to, but still below below, the transition to yield stress $I^\dagger \approx 500\,\text{mM}$ we see behaviour that is clearly not simple shear thickening (Fig. 4.12). The onset of shear thickening continues to visibly decrease with increasing I and although no samples discussed in this chapter have shown 'pure' shear thickening, the behaviour here deviates beyond explanations considering other colloidal effects (such as shear thinning). The $I = 266\,\text{mM}$ suspension shows shear thickening of the same form as shear thickening suspensions at lower ionic strengths (Fig. 4.5), but the higher ionic strengths show a clear divergence from this. At these higher ionic strengths a shoulder begins to appear in the shear thickening regime, eventually splitting the regime into two regions with an apparent viscosity plateau in between.

If shear thickening in silica were a result of two mechanisms, and only one of them is affected by weakening the repulsive force, then we would see a separation of the flow curve into two shear thickening regimes similar to what is visible at $I = 414\,\text{mM}$ (Fig. 4.12). This has not been observed before in experiments looking at variation of interparticle forces, as they have focused on strengthening the attractive force [23, 89, 106]. By attempting to weaken the repulsive force we

show that the resistance to the formation of frictional contacts is not weakened uniformly, leading to the separation into two regimes.

4.5 The Effect on Suspensions Behaviour while Continuously Varying the Solvent

A further way to study the forces controlling the onset of shear thickening is to change the fluid suspending the particles. We do so by considering $R = 0.75\,\mu\text{m}$ silica particles suspended in mixtures of two fluids, 80 wt.% G/W (with 0.2 mM fluoroscein sodium salt) and polyethylene glycol ($M_w \approx 200$ u) (PEG). These two suspending fluids were chosen as G/W creates a charge stabilised suspension, whereas suspending silica in PEG200 is understood to create a steric suspension [111] and these fluids are miscible with each other. Because the two fluids are miscible we are able to consider a continuous transition between the two 'pure' suspensions, and therefore between the two repulsive mechanisms. Due to the measured difference in the scaling of σ^* with R for electrostatic and steric suspensions there is clearly a difference in the nature of the transition from lubricated to frictional contact. To measure the effect of changing the stabilising mechanism from steric to electrostatic we continuously vary the wt.% of PEG (which we call X_{PEG}) in the fluid.

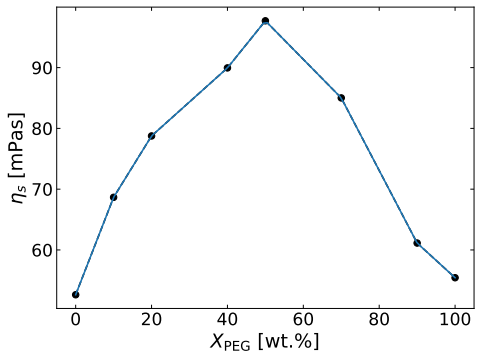

Figure 4.13 Graph of the change in viscosity with increasing polyethylene glycol 200 (PEG200) concentration with 80 wt.% G/W solution. Intermediate values were found by interpolating.

The viscosities of the two suspending fluids and their mixtures are not the same, which is taken into account by measuring the viscosity at various different mix ratios. The viscosity of the suspending fluid does not change monotonically between the two pure suspending fluids. A graph of measurements of the

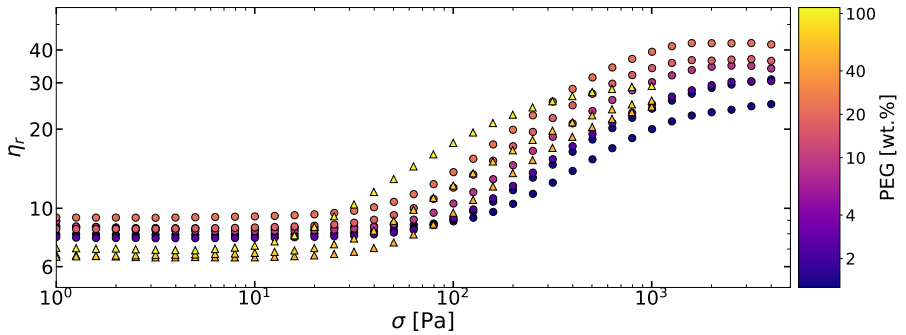

Figure 4.14 Variation of the relative viscosity of $R = 0.75\,\mu m$ with applied stress and PEG concentration. Silica particles were initially suspended in 80 wt.% G/W solution and then PEG was added (○), or were dried and then suspended in the fluid (△). The lower graph shows the same data normalised to the minimum viscosity measured.

viscosities of the suspending fluid mixtures is shown in figure 4.13, where there is a clear increase and then decrease in the viscosity with increasing X_{PEG}. Interpolated values were used to calculate the suspending fluid viscosity at a given X_{PEG}, which was taken to be fluid viscosity (η_f) and used to calculate $\eta_r = \frac{\eta}{\eta_f}$ (Fig. 4.14).

Our flow curves show a qualitative decrease in the onset stress as X_{PEG} increases (Fig. 4.14). The suspensions were prepared in two different ways, which appears to have created a difference in the low-shear viscosity. This could be a result of differences in how well the samples are dispersed, though it is more likely due to a difference in the volume fractions. The high X_{PEG} samples showed shear thinning effects at high stresses, and therefore were not measured at the same high stress as the other samples. There appears to be an increase in the high shear viscosity with increasing X_{PEG} (Fig. 4.14), though this is not consistent for all samples and may be a result of the difference in the volume fractions or dispersion previously discussed.

There is a clear trend in decreasing $\sigma^*(X_{\mathrm{PEG}})$ with increasing X_{PEG} (Fig. 4.15), suggesting that the critical repulsive force F^* preventing frictional contact at low stress is lower for silica suspended in PEG. The decrease in σ^* with increasing X_{PEG} suggests that the addition of PEG weakens the overall DLVO repulsion. Given the high relative dielectric constant of PEG, the weaker DLVO repulsion could be the result of an increase in the Hamaker constant, and therefore the van der Waals attraction. Further experiments with different particle sizes would be able to determine the nature of the transition between charge stabilisation and

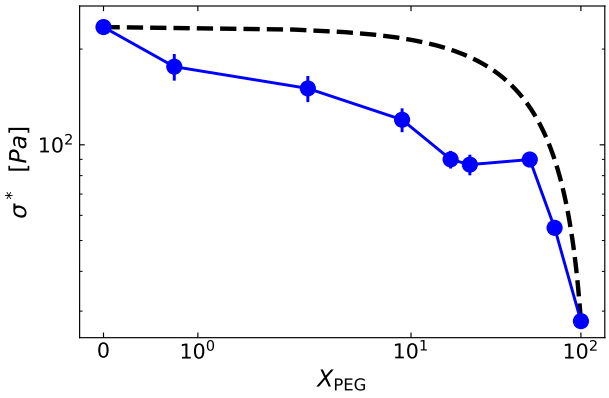

Figure 4.15 (blue circles) $\sigma^*(X_{\mathrm{PEG}})$ from fitting a WC-Type model fit to shear thickening data of $R = 0.75\,\mu\mathrm{m}$ silica suspended in80 wt.% G/W with increasing wt.% PEG (X_{PEG}), $\phi \approx 0.5$. (dashed line) Fit assuming linear interpolation between the two onset stresses $\sigma^* = X_{\mathrm{PEG}}\sigma^*_{\mathrm{PEG}} + (100 - X_{\mathrm{PEG}})\sigma^*_{G/W}/100$

steric stabilisation. The linear interpolation fails to follow the trend, which shows a more rapid decrease in σ^* than the linear interpolation predicts. This suggests that the PEG is having a more significant effect than reducing the repulsive force in proportion to the percentage of the suspending fluid it makes up. One possible explanation for this is that at low X_{PEG} the PEG is going to the surface of the particles and reducing the electrostatic repulsion while only having a small effect as a stabilising polymer.

4.6 Summary and Outlook

In this chapter we have taken our first look at experimental shear thickening rheology, and we have considered in detail the rheology of silica particles suspended in aqueous media. This chapter has allowed us to apply our understanding of the Wyart-Cates model to a physical system and draw subsequent conclusions about the physics of that system.

Our results are the first to measure the scaling of the onset of shear thickening with size using an experimentally verified electrostatically stabilised system, with clear consistency in the sample properties between the particle sizes, and using a physics based measure of the onset of shear thickening. As such we can be confident that the scaling of the onset stress of shear thickening with sizes for electrostatically stabilised shear thickening systems is $\sigma^* \propto 1/R$, a result that

is consistent with our theoretical prediction of an interparticle repulsive force which scales as $F^* \propto R$. We have shown that this repulsive force is purely electrostatic, as its strength can be controlled by the addition of free ions, and the system becomes attractive at high I when the electrostatic repulsion becomes sufficiently screened, meaning no other stabilising force is limiting contact. The sizes scaling strongly suggests that the force is the result of some potential between the surfaces, and from the Derjaguin approximation we know the force will be linearly related to the particle radius R.

Results for the $R = 2\,\mu m$ radius particles at ionic strengths between shear thickening and thinning show the beginning of a separation into two distinct shear thickening regions, which could suggest two shear thickening mechanisms. We have measured the effect of ionic strength on the extended volume of small ($R = 0.25\,\mu m$) electrostatically repulsive shear thinning particles, clearly showing the decrease in the strength of the thinning with decreasing electrostatic screening length λ_h, which is consistent with previous simulation results [110]. Our work has experimentally measured the variation in the onset stress with ionic strength for various sizes and found differences at high I which we attribute to the rotational Brownian motion of smaller particles allowing contact more optimal for attractive forces.

Further work was discussed, which looked at the variation of σ^* between different suspending fluids with different stabilisation mechanisms. The results show a continuous decrease in the onset stress of shear thickening from suspensions in 80 wt.% G/W (electrostatically stabilised) with increasing PEG (sterically stabilised) concentration, reaching a minimum at 100 wt.% PEG. This suggests that the addition of PEG decreases the strength of the electrostatic repulsion between silica particles, possibly due to the presence of PEG at the particle surface reducing the repulsive effect of surface charge.

In subsequent chapters we will use the WC-type model again, and will show the limitations of the model when considering behaviour above ϕ_M in chapter 5 and local shear thickening behaviour in chapter 6.

Chapter 5

Unsteady Flow: A Window into Micro-scale Contact Dynamics

The consideration of time-scales is ubiquitous across soft matter physics because the behaviour of soft materials is heavily dependent on the intrinsic time-scales of their constituent materials. Silly putty is a great example of time-scales in fluids, as it behaves as an elastic solid and can be bounced, but if left will pool and flow like a liquid. The relaxation of the elastic stress of silly putty can even be measured [112]. Dense suspensions exhibit similar time-dependent behaviour.

The Wyart-Cates model currently only describes steady state flow, and there is no established model for time-dependent flow of shear thickening suspensions. Although many methods have been used to probe the time-dependent behaviour of shear thickening suspensions[14, 79, 97, 113, 114], it can often be challenging to separate the behaviour of the suspension from rheometer artefacts.

The work discussed in this chapter builds on that of Richards et al. [26], which considered the strain- and time-scales present in shear thickening cornstarch suspensions. The model describes the interaction between the increasing viscosity caused by the increasing shear rate, and the rheometer tool inertia. The oscillations occur due to an 'overshoot' of the rheometer tool due its rotational momentum. This overshoot causes the system to become more viscous than it would be at equilibrium (as a result of shear thickening), which subsequently slows the tool. The slower tool allows the system to relax lowering the viscosity, at which point the rheometer tool speeds up and overshoots again. By performing similar experiments with shear thickening silica suspensions we are able to extract

the same characteristic parameters and compare them to those of cornstarch.

Although the unsteady flow observed by Richards et al. in cornstarch in glycerol/water [26] had already been observed for multiple shear thickening systems [72, 77, 79, 96, 115], their work demonstrated that the WC model could be extended to analytically capture these dynamics. Thus, fits to the extended time-dependent WC model can be used to extract characteristic time- and strain-scales which control the behaviour of the suspensions. We repeat this procedure using charge-stabilized silica particles to allow for comparison with the results for cornstarch, which should be considerably more deformable than the silica and is sterically stabilised, and thus can probe how the time-dependent dynamics depend on both the stabilisation method and particle properties.

5.1 Methods and Materials

A prediction from the extended WC-type model of Richards et al. [26] is that the occurrence of oscillations is dependent on a key dimensionless parameter ϵ which relates the rheometer tool's inertial time-scale

$$t_i = \rho_A h/\eta_f \tag{5.1}$$

where ρ_A is the areal density of the rheometer tool, and h is the gap height, and the contact network formation time-scale

$$t_c = \gamma_0 \eta_f/\sigma^* \tag{5.2}$$

where γ_0 is a characteristic strain-scale. For oscillations to occur, the contact network formation must be significantly slower than the tool inertia time-scale. We therefore define ϵ as

$$\epsilon = \frac{t_c}{t_i} = \frac{\gamma_0 \eta_f^2}{\rho_A h \sigma^*}, \tag{5.3}$$

where previous work has shown that for oscillations to occur ϵ must be below some critical value ϵ_c [26]. Where ϵ_c is dependent on the applied stress and the volume fraction of the suspension. A more detailed discussion of how these oscillations arise as a result of a limit cycle, and how ϵ_c can be calculated for a given suspensions is given by Richards et al. [26].

To produce shear rate oscillations in silica suspensions, 2 µm radius silica particles

were suspended in 80 wt.% DMSO/water solution. The particles were washed and then dispersed as described in chapter 3. A stock sample was made up of the silica and diluted to the required volume fractions by the addition of DMSO/water mixture. Experiments were performed on an MCR302 rheometer using a 20 mm plate-plate rheometer tool with a 1.5 mm gap height. The particles, suspending fluid, and gap height were chosen to minimise ϵ such that $\epsilon < \epsilon_c$.

5.2 Steady State Behaviour of Silica Systems Above ϕ_{M}

We first consider the steady state behaviour of our system. As noted in Ch. 2, the WC model generally fails to capture the experimentally observed thickening above ϕ_M, where the model predicts backwards bending flow curves $\sigma(\dot{\gamma})$ (or equivalently backwards bending $\eta_r(\dot{\gamma})$ curves). Instead, experiments in this 'backwards bending' regime typically show abrupt jumps in the time-averaged viscosity at a constant (average) shear rate $\dot{\gamma}_c$. As we will detail later, these time averaged quantities miss the rich underlying flow dynamics, but we should still expect that the location of the jump $\dot{\gamma}_c(\phi)$ should correspond with the 'nose' of the backwards bending flow curves predicted by the WC model.

Flow curves were produced for volume fractions in the range $\phi \approx 0.5$ to 0.6. As noted above, although we do not expect the Wyart-Cates model to accurately describe the shear thickening observed above ϕ_M, we should expect it to at least capture the onset of this thickening.

To fit the Wyart-Cates model to the steady state flow curves we first consider the change in the low stress viscosity due to the volume fraction. As discussed in Chapters 2 and 4 the viscosity at stresses below shear thickening is described by an empirical relation, with a divergence at ϕ_0 (Eq. 2.11), which we reiterate here

$$\eta_r = A\left(1 - \frac{\phi}{\phi_0}\right)^{-2}. \tag{2.11}$$

Our flow curves above ϕ_M show shear thinning prior to thickening (Fig. 5.1), which is not present in the standard WC model. We therefore take the minimum viscosity of the flow curves as the low shear viscosity, and fit it to equation 2.11 to find the parameters A and ϕ_0 (Fig. 5.2). For this set of suspensions we found

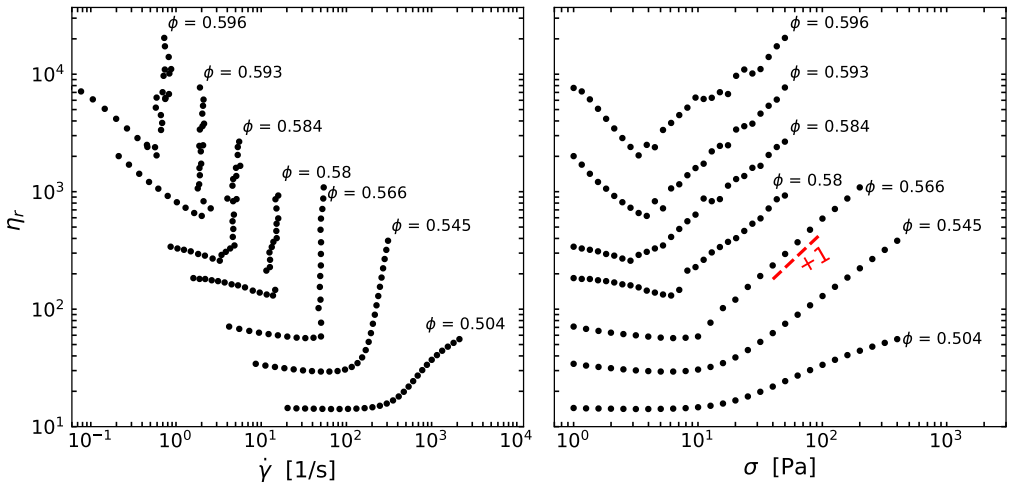

Figure 5.1 Flow curves at indicated volume fractions ϕ showing the time-averaged relative viscosity η_r against both the applied shear stress σ and the time averaged shear rate $\dot{\gamma}$. The time averaging interval was varied to keep the accumulated strain per point roughly fixed ($\gamma \gtrsim 5$). A line of slope 1 on the log-log scale highlights the regime where $\eta = \dot{\gamma}\sigma \propto \sigma$, corresponding to a vertical line when plotted against $\dot{\gamma}$.

$A = 0.27(3)$ and $\phi_0 = 0.608(1)$, which we note is below $\phi_{\text{RCP}} \approx 0.64$. This may be a result of an overlap between the shear thinning and shear thickening observed (Fig. 5.1(b)) meaning we use a value greater than that of the low shear plateau. As most of our suspensions show DST and no real high stress plateaus, we assume ϕ_M cannot be accurately calculated and estimate it as $\phi_M \approx 0.566$. We choose this value as it is the first value at which we observe a gradient of 1 in the shear thickening (Fig. 5.1). As we discussed in Ch. 2 and the previous chapter, shear thinning prior to thickening can arise due to finite ranged repulsive interactions or from weak attractive forces. Given our large particle size ($R = 2\,\mu\text{m}$) and short screening length ($\lambda_D \approx 10^{-2}\,\mu\text{m}$) we might expect finite ranged repulsive forces to have a minimal role, suggesting some amount of weak attraction may be present. However, since the thinning only becomes pronounced very close to ϕ_0 it is difficult to determine its precise origin.

Plots of the relative viscosity η_r against the stress (Fig. 5.1) (σ) and the average shear rate $\dot{\gamma}$, show the expected qualitative transition in the thickening behaviour above $\phi_M \simeq 0.566$. The flow curves show a clear sigmoidal shape well below ϕ_M and transition to a clear abrupt jump in η_r at fixed $\dot{\gamma}_c$ close to and above ϕ_M.

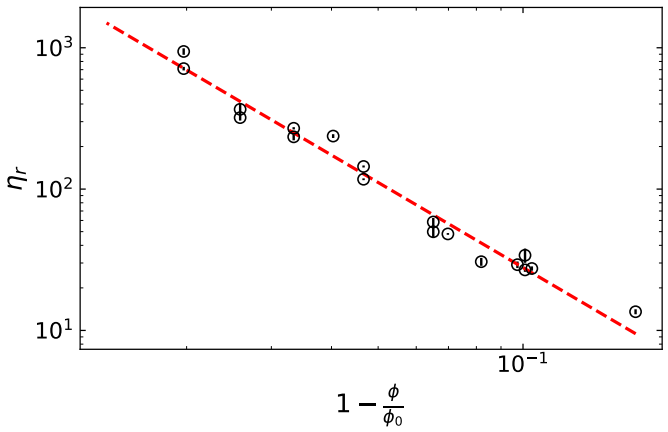

Figure 5.2 Minimum steady state viscosity against volume fraction of silica suspensions. With $0.504 \leq \phi \leq 0.596$. The dashed line is a fit to equation 2.11, with $A = 0.27(3)$ and $\phi_0 = 0.608(1)$.

We reiterate the equations used to describe the Wyart-Cates model here,

$$\phi_J = f\phi_M + (1-f)\phi_0, \tag{2.29}$$

$$f = \exp\left(-\left(\frac{\sigma^*}{\sigma}\right)^{\beta}\right), \tag{2.31}$$

as they will be integral to understanding fits to the steady state data, and the time dependent model discussed later.

The results show a trend in decreasing onset stress of shear thickening above ϕ_M, which is a result not found in the standard Wyart-Cates model, where σ^* is assumed to be the same for all volume fractions. We fitted σ^* individually for each volume fraction above ϕ_M, using equations 2.31, 2.29 and 2.11, by considering the shear rate dependent behaviour and attempting to fit the 'nose' of the curve (Fig. 5.3). The experimental flow curve is at constant shear rate, whereas the model flow curves bend backwards, the point at which the model shows this 'backwards bending' behaviour is when the steady state rheology should exhibit a constant shear rate [62].

By attempting to fit the WC-type model with a variable $\sigma^*(\phi)$ we get much better agreement of the 'nose' (Inset Fig. 5.3) with the data (i.e. we better capture with the model where the discontinuous behaviour suggests a 'backwards bending' flow curve). The WC-type model used does not always quantitatively capture the full steady state flow curves but can, as we will see later in the chapter, be used to model the change in f with time. We also only consider shear rate oscillations

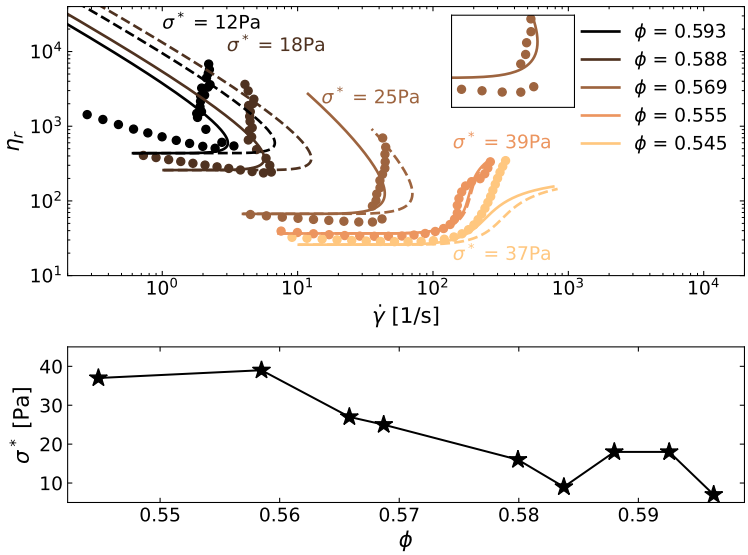

Figure 5.3 (a) Selected time-averaged flow curves $\eta_r(\dot{\gamma})$ from figure 5.1 (circles, ϕ indicated in legend) showing WC model fits with either fixed $\sigma^* = 39\,\text{Pa}$ (dashed lines) or with a variable $\sigma^*(\phi)$ (solid lines). (b) Variation in estimated σ^* with increasing ϕ. The inset shows the 'nose' of the curve.

close to the 'nose' of the flow curves, firstly because we wish to see at what stresses the shear rate oscillations begin to appear, and secondly because this is the region that the steady state WC-model best fits.

We note that the system begins to show discontinuous shear thickening at $\phi = 0.555$ (Fig. 5.3). This suggests ϕ_{DST}, the volume fraction above which the system shows discontinuous shear thickening, is somewhere below this value (i.e. $\phi_{\text{DST}} < 0.555$). As will become clearer when we discuss the model, we only expect shear rate oscillations to occur above this value.

5.3 Shear Rate Oscillations

As previously seen in other shear thickening systems [26, 63, 77], we found that the flow can become unsteady and time-dependent at high concentrations where the thickening becomes discontinuous. For $\phi = 0.55$ (below $\phi_M = 0.566$) we find periodic shear rate oscillations appear near the 'nose' of the flow curve, where the slope of the $\mathrm{d}\sigma/\mathrm{d}\dot{\gamma} \to \infty$ (Fig. 5.4(a)). The frequency of the oscillations increases further with increasing applied stress (Fig. 5.4(b,c)). At stresses below the 'nose' of the flow curves we see no oscillations (Fig. 5.4(a)), though the increasing shear

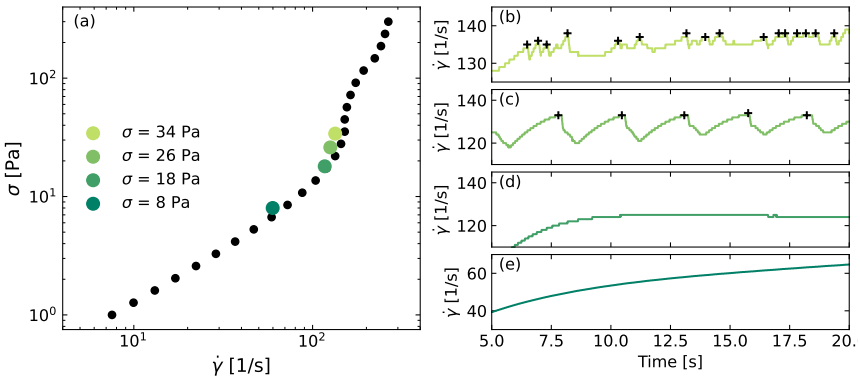

Figure 5.4 (a) Steady state flow curves with time averaged values from (b-e) (legend), alongside time dependent behaviour at stresses (b) 34 Pa, (c) 26 Pa, (d) 18 Pa, (e) 8 Pa. Data is for $\phi = 0.55$. The measured peaks of the oscillations are marked with a '+'.

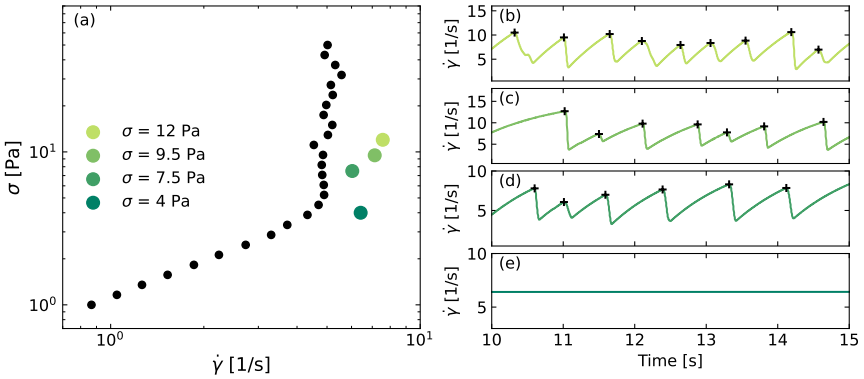

Figure 5.5 (a) Steady state flow curves (black points) with time averaged values from (b-e) (legend), alongside time dependent behaviour at stresses (b) 12 Pa, (c) 9.5 Pa, (d) 7.5 Pa, (e) 4 Pa. Data is for $\phi = 0.584$. The measured peaks of the oscillations are marked with a '+'.

rate is visible, as the system reaches steady state in a shorter time period (Fig. 5.4(d,e)) at higher applied stress. As the applied stress is further increased, the oscillations both increase and begin to become more erratic (Fig. 5.4(b)).

These regular oscillations are also observed above ϕ_M (Figs. 5.5, 5.6), where the system is clearly above ϕ_M. As with our example at $\phi = 0.55$, the flow remains steady prior to the onset of shear thickening. Close to the onset of thickening regular oscillations appear, again the oscillation frequency increasing with both volume fraction and applied stress.

The 'steady state' measurements are simply the viscosity averaged over a given time after the apparent stress is reached. They are therefore subject to variation dependent on the point in the frequency and the number of oscillations observed.

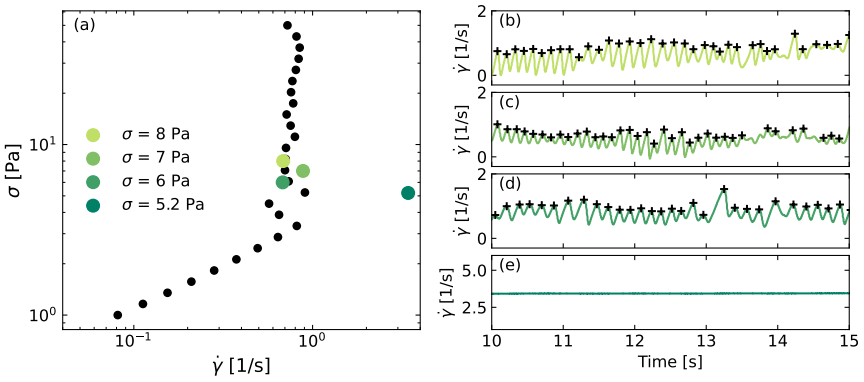

Figure 5.6 (a) Steady state flow curves with time averaged values from (b-e) (legend), alongside time dependent behaviour at stresses (b) 8 Pa, (c) 7 Pa, (d) 6 Pa, (e) 5.2 Pa. Data is for $\phi = 0.596$. The measured peaks of the oscillations are marked with a '+'.

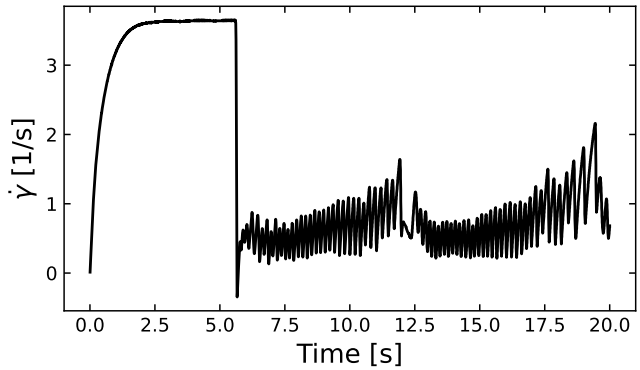

Figure 5.7 Shear rate against time for a silica in DMSO water suspensions with $\phi = 0.596$ and $\sigma = 5.4$ Pa.

This is likely the reason for the difference between the time dependent (colored discs) and steady state (black discs) results (Fig. 5.5), where the startup has a greater effect on the shorter averaging times used to measure the flow curves.

Figure 5.6(a) shows a more pronounced difference between the steady state and time-dependent shear rate for $\sigma = 5.2$ Pa. We attribute this to timing of the transition to the time before the system becomes oscillatory, but it is still under an applied stress. The time dependent results show the system at a significantly higher shear rate before the onset of oscillations (Fig. 5.7). This transition suggests that a meta-stable state exists at high shear rates before the onset of oscillations. There also appears to be a secondary oscillation occurring as the peak shear rate increases with time and then drops.

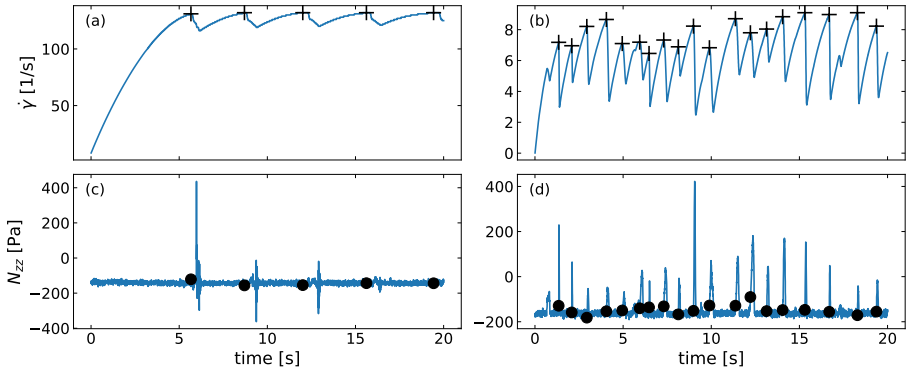

Figure 5.8 Figures showing the variation in the shear rate $\dot{\gamma}$ and normal stress perpendicular to the tool geometry N_{yy} (where y the gradient direction) with time at constant applied stress σ_{App}. (a,c) Graphs for a sample with $\phi = 0.555$, at $\sigma_{\text{App}} = 24\,\text{Pa}$. (b,d) Graphs for a sample with $\phi = 0.584$, at $\sigma_{\text{App}} = 6.5\,\text{Pa}$. The peaks were found for the shear rates and are marked with a '+', these same peaks are superimposed on the normal stress data as $\circ$.

5.3.1 Characterising the Oscillations

To characterise these shear rate oscillations we used a peak finding routine to identify local maxima in the shear rate $\dot{\gamma}(t)$ (Fig. 5.8). The mean oscillations frequency $\nu \equiv \langle 1/\delta t \rangle$ was computed from the time intervals (δt) between successive maxima, with the standard deviation giving a measure of the uncertainty $\Delta\nu$.

It was noted that the spikes in the normal stress measurements coincided closely with the peaks in the shear rate (Fig. 5.8). Values of the frequency of oscillations were measured for both the normal force and the shear rate, and were generally found to be in good agreement. The frequencies later compared to the model were measured from the shear rate only.

The oscillations observed in the shear rate at low volume fractions show a slight plateau and the maxima of the peaks are less clear (Fig. 5.8(a)). At higher volume fractions the oscillations become more erratic leading to larger errors (Fig. 5.8(b).

The peak finding routine for both the normal force and the shear rate measurements used two values, the prominence and separation, which were varied and visually verified as capturing the peaks. The prominence was calculated as a fraction of the difference between the highest and lowest shear rates after oscillations had begun. This was done to try to avoid 'mini' peaks and secondary

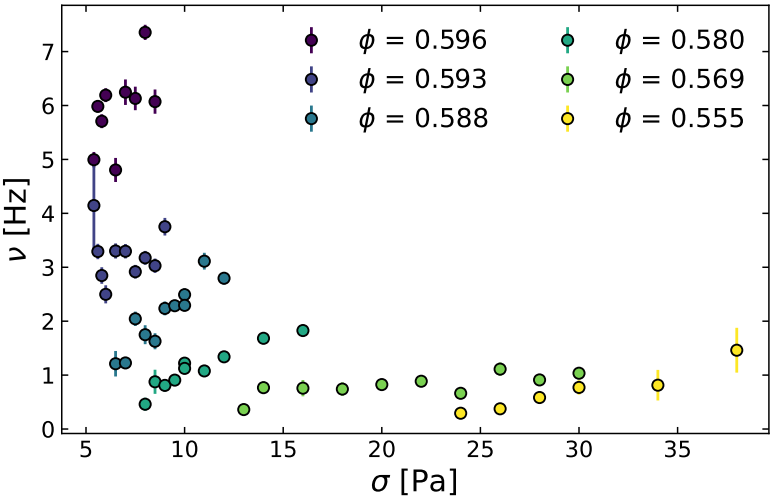

Figure 5.9 Frequency measured $\nu(\sigma)$, measured from the peaks of the shear rate (Fig. 5.8) for silica suspended in DMSO/water at various volume fractions (legend).

peaks. Similarly, by adding a finite separation between peaks ($\delta_{\min} < \langle \delta t \rangle$) we again avoid finding erroneous peaks. As the frequency increases more errors may occur in the peak finding routine due to the more erratic nature of the oscillations, but as there are also more peaks to observe we do not expect this to significantly affect the measured frequency.

The frequency of the shear rate oscillations increases with increasing applied stress and volume fraction (Fig. 5.9). The minimum stress at which oscillations occur was also observed to decrease with increasing ϕ, which is consistent with the decreasing σ^* observed for the steady state data. The oscillations are strongly linked to the shear thickening of the suspensions, and therefore their onset is strongly related to the onset of shear thickening. Higher volume fractions show a more pronounced increase in the frequency of the oscillations with increasing applied stress, and also show more δt shows more variation, which is reflective of the more erratic nature of the oscillations (Fig. 5.6).

5.4 The Model

To describe the behaviour of the shear rate oscillations we use a modified version of the Wyart-Cates model which introduces time-dependence. A qualitative description of the model was given at the start of the chapter, here we cover the

equations necessary to understand how we fit to measured values of the frequency using the fitting parameters γ_0 and t_r. The model is taken from the work of Richards et al. [26], which also gives an in depth study of the limit cycle and the conditions required for the resulting shear rate oscillations to occur. Here we give a brief introduction to the model.

To describe the time-dependent behaviour of shear thickening suspensions in a rheometer we consider two coupled differential equations. The first equation considers the rate of change of the shear rate $\dot{\gamma}$, this is simply a force balance equation given by

$$\rho_A h \frac{d\dot{\gamma}}{dt} = \sigma - \eta(f)\dot{\gamma} \tag{5.4}$$

where ρ_A is the tool areal density, h is the gap height, σ is the external applied stress, and $\eta(f)$ is the viscosity for a given f value. The left hand side of equation 5.4 is the inertia of the rheometer tool which is balanced by the external stress applied by the rheometer itself and the resistance to motion resulting from the fluid viscosity. For most experiments the tool inertia is ignored, but in this case the oscillations are a result of the rheometer inertia. For the experiments discussed in this section a parallel-plate geometry with areal density $\rho_A = 400\,\mathrm{kg\,m^{-2}}$ was used.

Next we consider the rate of change of the fraction of frictional contacts f. The rate of change df/dt is related to the difference between the current fraction of frictional contacts f and the fraction of frictional contacts expected at steady state for an applied stress $\hat{f}(\sigma)$; This is scaled by a characteristic strain γ_0 and the shear rate of the suspensions $\dot{\gamma}$. This gives the relation:

$$\frac{df}{dt} = \frac{\dot{\gamma}}{\gamma_0}[\hat{f}(\sigma) - f], \tag{5.5}$$

where the parameters are as described above. The relation assumes that $\dot{\gamma} \geq 0$. We are left with a system where f always approaches the steady state value of $\hat{f}(\sigma)$.

Although this model predicts shear rate oscillations, the frequency of the oscillations was found by Richards et al. [26] not to coincide with that found in experiment. Therefore an empirical relaxation parameter t_r was added to equation 5.5 giving

$$\frac{df}{dt} = \left(\frac{\dot{\gamma}}{\gamma_0} + \frac{1}{t_r}\right)[\hat{f}(\sigma) - f]. \tag{5.6}$$

5.5 Fitting the Model

In section 5.2 we attempted to fit a WC-type model to the steady state flow curves of several shear thickening suspensions. Here we show how the fitting parameters found, alongside the previously discussed model, can be used to accurately model the frequency of shear rate oscillations in shear thickening suspensions. The resulting fitting parameters give us an insight into the internal time-scales and strain-scales present in silica suspensions.

To fit the model to the frequency data we first measure the value γ_0 by considering an instantaneous jump in the shear rate applied to a shear thickening suspension. We subsequently use this value of γ_0 and vary the parameter t_r to produce accurate fits for the variation of the frequency of the shear rate oscillations with increasing applied stress for various volume fractions.

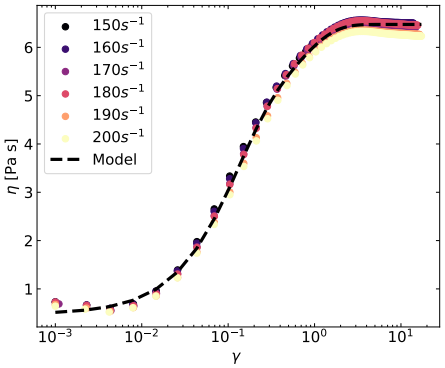

Figure 5.10 Shear rate jumps performed on 2 µm radius silica suspended in 80wt% G/W solution at 10 °C and $\phi = 0.55$. The dashed line shows fits using equation 5.7 using a double exponential of the form in equation 5.7, with fitting parameters $A = 6.47(9)$, $B = 3.7(1)$, $C = 2.27(8)$, $\gamma_0 = 0.110(5)$, and $\gamma_1 = 0.61(1)$. The shear rate jumps were performed beginning from $\dot{\gamma} = 1.02\,\mathrm{s}^{-1}$ to an upper shear rate (legend).

Shear rate jump measurements were taken using an Ares G2 rheometer with a 40 mm roughened plate-plate geometry. The samples were also cooled to 10 °C to lower the solvent viscosity. The larger plate diameter and lower solvent viscosity allowed for the application of a much higher stress, such that the assumption $\sigma \gg \sigma^*$ is satisfied. We find that the curve perfectly fits a double exponential (Fig. 5.10) of the form

$$\eta = A - B\exp\left(-\gamma/\gamma_0\right) - C\exp\left(-\gamma/\gamma_1\right) \tag{5.7}$$

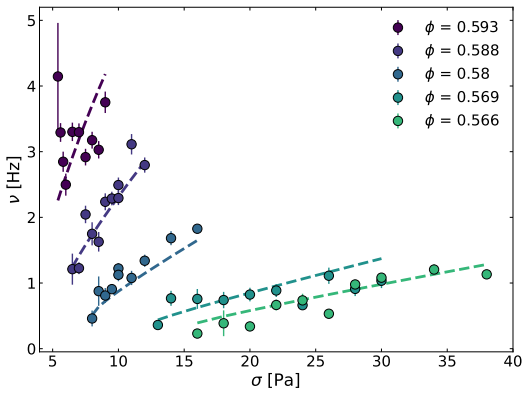

Figure 5.11 Oscillation frequency $\nu(\sigma_{\mathrm{E}})$ with model fits where $\gamma_0 = 0.11$ and $t_r = 0.03\,\mathrm{s}$ for silica suspensions at various volume fractions (legend).

where we find A, B, C, γ_0, and γ_1 are fitting parameters. A is taken as the maximum viscosity, the other parameters are found by fitting each curve individually with different maximum shear rates and averaging the parameters. We find two characterstic strain scales $\gamma_0 = 0.110(5)$ and $\gamma_1 = 0.61(1)$. We use the shorter of the two strain-scales $\gamma_0 = 0.11$ for fits of the frequency. We justify this by considering the increase in f with strain is most important at low strains when considering oscillations at such high frequencies and shear rates (Fig. 5.8).

We now move onto considering fitting the predicted frequencies of the oscillations to the measured frequencies of the oscillations. It is from this fitting that we are able to find a value of t_r using the value of γ_0 found earlier (Fig. 5.10). Theoretical frequency values are found by numerically solving the model and then measuring the frequency using the same peak finding routine used earlier (Sec. 5.3.1). Fits to the frequency show the same trend in increasing frequency with increasing apparent stress, but do not capture the variation in the data perfectly 5.11. The model underestimates some data (Fig. 5.11 $\phi = 0.58$) and does not capture the erratic variation in the frequency.

We are only able to capture the stress onset of the oscillations by varying σ^* for each volume fraction. We find that the values of σ^* found for these fits are lower than those found when attempting to fit steady state curves using the steady state WC model (Sec. 5.2).

The relaxation time t_r can be bound above and below as $5 \times 10^{-3}\,\mathrm{s} < t_r < 10^{-1}\,\mathrm{s}$ (Fig. 5.12). The oscillations at higher volume fractions are more strongly dependent on t_r (Fig. 5.12) because $\phi_J = \phi_M$ at a lower value of f, and therefore

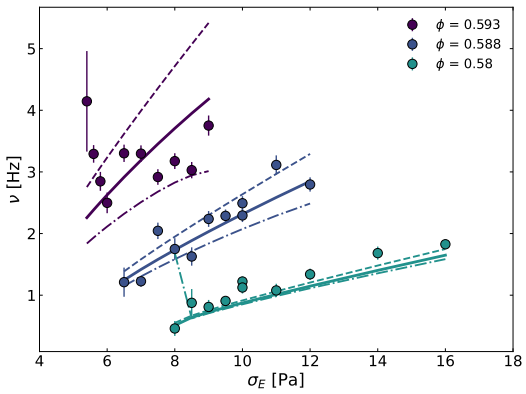

Figure 5.12 Oscillation frequency $\nu(\sigma_{\mathrm{E}})$ with model fits where $\gamma_0 = 0.11$ and $t_r = 0.03\,\mathrm{s}$ (solid lines) at various volume fractions (legend). Results of the model using estiamtes of the lower ($t_r = 0.01\,\mathrm{s}$) (dashed), and upper ($t_r = 0.2\,\mathrm{s}$) (dashed-dotted) limits of the relaxation time are shown.

these suspensions are more strongly affected by an increasing f.

5.6 Limitations of the Model

Although this model captures well the variation in the frequency of oscillations for a wide range of volume fractions of silica suspensions, the model struggles to capture the reality of the time dependent behaviour (Fig. 5.13).

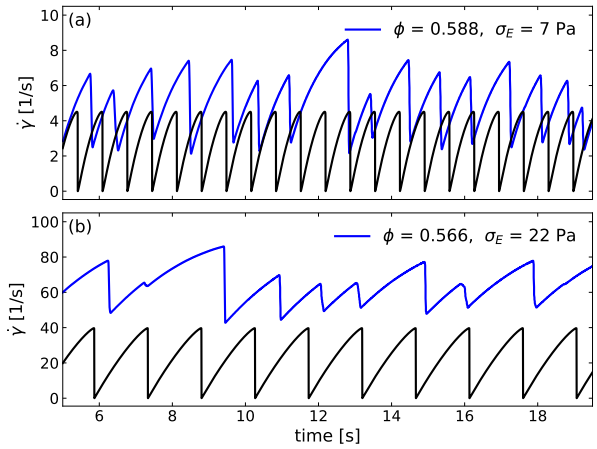

Figure 5.13 Shear rate against time for 2 µm silica particles suspended in DMSO/water solution (blue lines), at different volume fractions as applied stresses (legend), compared with model predictions for the same applied stress and volume fraction (black lines).

From figure 5.13 it is clear that the model does not capture the erratic nature

of the oscillations. Though it is reasonable to assume that the time averaged frequency should match that of the model. This erratic oscillation of the shear rate could be heavily related to inhomogeneities in the suspensions, a region with very high f may be enough to jam the whole system. One could also speculate about random cascading events that cause a sudden increase in f, this may lead to the delayed drop in the shear rate also observed in the oscillations. The second large distinction is the magnitude of the shear rate. The model predicts a much lower shear rate overall than the one measured. This is especially clear at the lower volume fraction shown in figure 5.13(b).

Similar comparisons for cornstarch show generally better agreement, though similarly the model predicts the system to become stationary when it does not do so in experiments. The maximum shear rates reached agree well for cornstarch suspensions [26]. There is a fundamental difference in the model's ability to capture the shear rate accurately between cornstarch and silica suspensions.

The model predicts the shear rate to go to zero at some point in the cycle due to shear jamming. Both samples in were above the jamming volume fraction, but the data clearly does not show the shear rate going to zero (Fig. 5.13). This could be a result of the tool slipping as the system fully jams, which the model does not account for.

The model only predicts a single time-scale for the formation of frictional contacts, which is not what we observe experimentally (Fig. 5.10). This single time-scale captures shear thickening startup well for cornstarch data, as shown in previous work [26]. The two-scale process is indicative of some sort of hierarchical structure in the shear thickening process, within which smaller multi-particle structures must initially form before large-scale (system-spanning) force chains can form. Evidence of such a distinction in silica and not in cornstarch is likely a result of the more uniform size of the silica compared to cornstarch. Further experiments and simualtions are necessary to explore this further.

5.7 Conclusions

In this chapter we have attempted to probe time- and strain-scales in shear thickening silica suspensions using an extended WC-type model.

We began by considering the steady state behaviour of silica suspensions at

volume fractions close to and above ϕ_M. We have shown that the onset stress of shear thickening σ^* generally decreases with increasing volume fraction for $\phi \geq \phi_M$. As we have discussed earlier this behaviour is not observed below ϕ_M in silica (Ch. 4) [68], nor is it observed in cornstarch in water suspensions above ϕ_M [26]. Similarly, simulation results of suspensions with electrostatic-like interactions and volume fractions above ϕ_M do not predict a lower σ^* above ϕ_M when fitted with a WC-type model [21]. This suggests it is a result unique to silica, and likely results from the physical properties of silica, by comparison with cornstarch we can consider the possible physical properties that could be the origin of this behaviour. Silica is electrostatically stabilised meaning there are likely complex multi-particle interactions due to the disassociated ions, which would not be seen in the sterically stabilised cornstarch. Silica is also stiffer, and at high concentrations and stresses a particles ability to deform could change the local volume fraction allowing for more force to be applied before strong thickening occurs.

We have found that the shear thickening startup of silica can be perfectly modelled by an empirical double exponential equation (Eq. 5.7), which we use to extract two strain-scales $\gamma_0 = 0.110(5)$ and $\gamma_1 = 0.61(1)$ the first of which we use in the Wyart-Cates based model for shear rate oscillations. The results showing a double exponential is clearly distinct from shear thickening startup in cornstarch suspensions, which can be captured by a simplification of the shear rate oscillation model in the limit of $\hat{f}(\sigma) = 1$, which uses a single exponential with a strain-scale $\gamma_{0c} = \mathcal{O}(10^{-1})$ [26]. The faster strain-scale for silica is similar to the single strain-scale for cornstarch, which could suggest a similar initial behaviour.

Notably we find that the relaxation times for silica ($t_r \approx 0.03\,\mathrm{s}$) and cornstarch $t_r \approx 0.24\,\mathrm{s}$ [26] are distinctly different. This suggests that this value is not universal to shear thickening suspensions, but is instead related to the material properties; the stiffer silica particles may take longer to relax from contact as they deform less, or because the electrostatic stabilisation present in suspensions of silica shows such a strong repulsive force at very close contact [16].

Other methods have been used to measure time-scales in non-Brownian suspensions [97, 116, 117]. Simulations show that for systems below ϕ_0 the relaxation time-scale of sheared suspensions varies with increasing ϕ as $\tau \propto (\phi_J - \phi)^{-3.3}$ [116, 117]. These simulation results give a relation of increasing t_r with increasing ϕ which was note observed in this work. No direct comparison of the time can be made as the results of the simulations are dimensionless.

Again our results suggest a single value for the relaxation time of shear thickening suspensions, unlike the work of Barik et al. [97], as both systems were considered in the same volume fraction range. It is possible that this method of observing shear rate oscillations only captures the quicker time-scale $\mathcal{O}(10^{-1}\,\mathrm{s})$ (called t_p in [97]). This result, alongside the results of Richards et al. [26], suggests that suspensions which are sterically stabilised [26, 97] show much longer relaxation times than the electrostatically stabilised silica. The slower time-scale observed by Barik et al. [97] is much longer $\mathcal{O}(1\,\mathrm{s})$ than the range within which t_r was found to be.

These results suggest fundamental differences between silica suspensions and cornstarch suspensions which, clearly affect the time-scales and the dynamics of the shear thickening. More fundamentally they may suggest clear differences in the time dependent behaviour of suspensions depending on their respective stabilisation mechanisms.

Chapter 6

Impact of Rheometer Plate Misalignment on Boundary Stress Microscopy Measurements of Silica Suspensions

Boundary stress microscopy has developed out of traction force microscopy, a method used to measure the local stresses (on the order of 1 µm) exerted by objects (such as cells) on a surface by embedding tracer particles in a soft elastic substrate. [118]. Using the same principle, boundary stress microscopy images materials under shear by coating the bottom of a rheometric geometry (either cone-plate or plate-plate) with a thin elastic layer and imaging the local displacements from below [27, 75, 76, 119]. Previous work by others [27, 75, 76] using boundary stress microscopy to study shear thickening suspensions revealed spatio-temporal stress fluctuations even below ϕ_M and the DST onset, where one would expect steady flow. We test the generality of these results using a similar model shear thickening suspension, and find unexpected discrepancies between the measured local and bulk stresses. We show such discrepancies could easily arise from a small degree of plate misalignment, a factor not considered in previous work. Our results demonstrate that boundary stress microscopy can be exquisitely sensitive to these almost unavoidable misalignments, particularly with highly non-Newtonian materials, suggesting the results from such measurements must be interpreted with care and caution.

In this chapter we first discuss the boundary stress microscopy setup and the analysis procedure, highlighting challenges encountered with calibration of the setup. We then introduce a simple analytic model to account for the effects of plate misalignment and compare these model results to measurements with shear thickening silica suspensions. We then compare the structure and dynamics of the local stress fluctuations in our system against prior measurements from other groups.

6.1 Boundary Stress Microscopy Experimental Setup

We carry out boundary stress microscopy by adapting our home-built rheo-confocal setup, in which an Anton-Paar MCR301 rheometer sits above a SP8 confocal microscope to allow viewing of samples under shear from below. In our setup, the bottom plate consists of a large glass coverslip fixed to a metal plate with an open hole for viewing. To enable boundary stress microscopy we coat the glass coverslip with a thin layer of polydimethylsiloxane (PDMS) and attach small fluorescent beads to the top of the PDMS layer. For the plate used in sample set 2 a second, thinner PDMS layer was formed on top of the beads to stop bead removal. The hole must be small enough to limit the effects of the glass deforming due to normal stresses. The PDMS coated glass coverslip has fluorescent beads bonded to the upper surface which were imaged using the confocal microscope with a 10× objective. A diagram of the setup is shown in figure 6.1.

To prepare the boundary stress setup, 50 mm glass coverslips were cleaned by sonication in an acetone-ethanol mixture, rinsed with de-ionised water and then dried under vacuum. The PDMS layer used Sylgard 184 (Dow Corning) which was mixed with curing agent at a ratio of 20:1, then mixed by hand for 15 min, and left on the roller mixer for 1 h. The PDMS mixture was degassed under vacuum for another hour until no bubbles were visible and then spin coated on the surface of the glass coverslip at 1800 rpm for 40 s to produce a layer of PDMS approximately 65 µm thickness.

To functionalise the PDMS the coated glass coverslips were placed within covered glass plates with (3-Aminopropyl)triethoxysilane (APTES). The APTES was allowed to evaporate and functionalise the open surface of the PDMS. To image

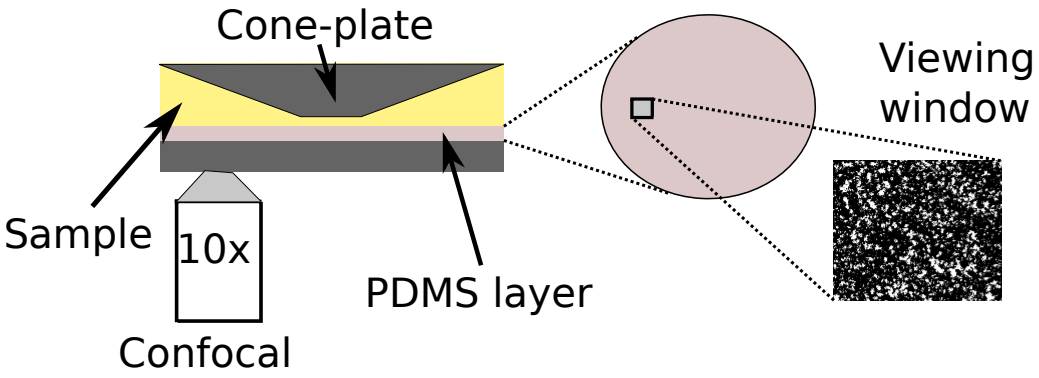

Figure 6.1 Diagram of the boundary stress microscopy setup consisting of fluorescent bead coated PDMS as the bottom plate, and a cone geometry with an angle of 1° (not to scale). The images were viewed with a 10× objective which gave a viewing window of approximately $1 \times 1\text{mm}^2$.

the upper surface carboxylate modified fluorescent spherical beads of radius 0.5 µm were attached to the PDMS surface by immersion in a suspension of the beads. The beads were suspended at 0.006 % solids in a buffer solution consisting of 3.8 mg mL^{-1} sodium tetraborate, 5 mg mL^{-1} boric acid, and 0.1 mg mL^{-1} 1-ehtyl-3-(3-dimethylaminopropyl) carbodiimide. For later measurements a second layer of PDMS approximately 10 µm thick was spin coated above the beads (to avoid beads being removed under shear) and cured at 85 °C for 1.5 h. Suspensions of $R = 0.75$ µm silica in 80 wt.% glycerol/water were prepared as described in chapter 3.

The bottom plate was aligned as described in chapter 3. We then adjusted the confocal scan direction in software to align the flow direction with the horizontal. The sample was then placed in the rheometer and trimmed with the same setup as described in chapter 3, but with the bottom plate replaced by the PDMS coated glass coverslip. For measurements, images were taken at a rate of 7 fps or 14 fps with a resolution of 1024×1024 pixels. The bead height was measured as the difference between the height of the glass-PDMS boundary and the height of the fluorescent beads; these heights were found by finding the height of the peak brightness in these two regions, where the brightness at the glass-PDMS boundary was a result of reflected light. For the case of a second layer of PDMS above the fluorescent beads the top of the second PDMS layer could be viewed from the reflection at the PDMS-air interface. The protocol left 10 s to 20 s gaps at the start and end of the recording where no stress was applied to the sample. Stress was then applied for 30 s and 90 s, depending on the sample.

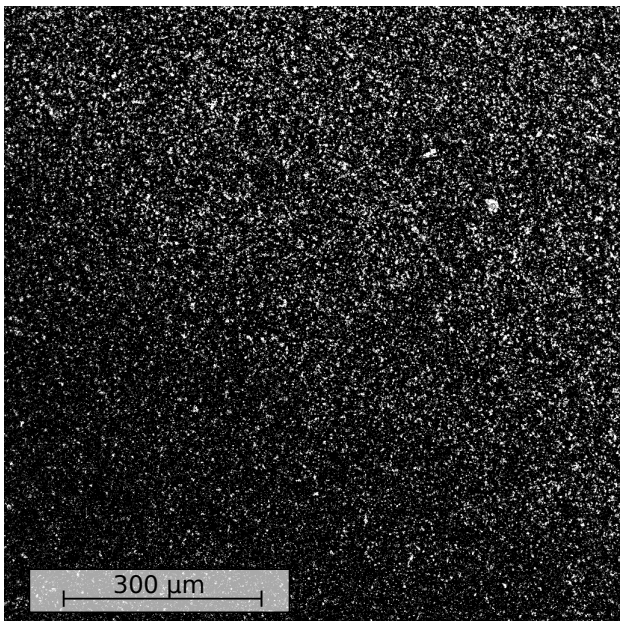

Figure 6.2 Confocal Microscope image of fluorescent beads bonded to the top layer of a thin PDMS substrate.

6.2 Measurement and Calculation of Boundary Stresses

The beads on the PDMS surface (Fig. 6.2) allowed for measurement of the displacement using particle image velocimetry (PIV). A Python package (openPIV [120] was used to measure the displacement by measuring the correlation between 20×20 pixel quadrants of the images, giving a displacement map. Average displacements with different quadrant sizes were compared to check no errors appeared from using smaller quadrants. Displacements were all measured relative to the first frame and subsequently filtered by convolution with a Hann window with a length scale which was called the minimum feature size. The filter was applied to remove high frequency noise resulting from background light, and any electrical noise in the system, an appropriate minimum feature size was chosen based on the data. Before filtering the data was padded with zeros.

Bead displacement is predominantly in the flow direction (x) (Fig. 6.3(a)), although there is some spatial variation along with displacements in the vorticity direction (z) (Fig. 6.3(a)). The boundary stresses measured were not consistent across the viewing window (Fig. 6.3(b)), which was likely a result of the variation in the bead density leading to differences in the accuracy of the displacement measurements. The edges also showed a distinctly lower stress, which was a

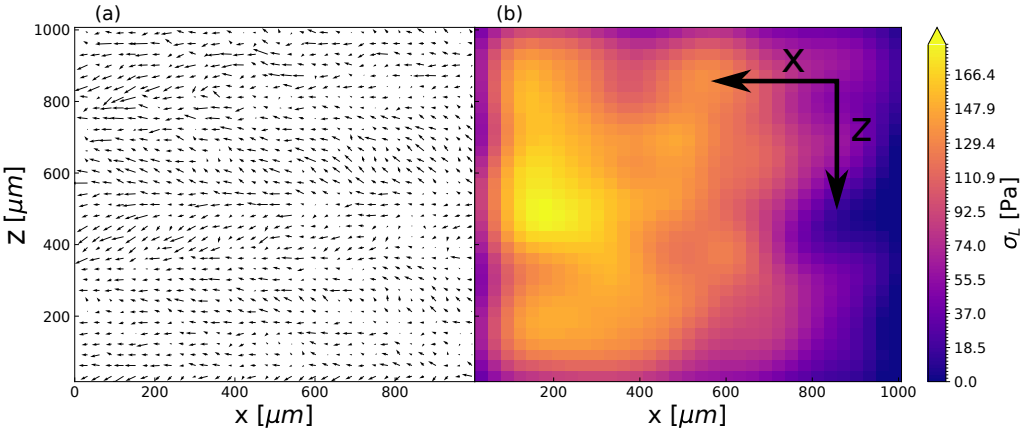

Figure 6.3 (a) Displacement field calculated using particle image velocimetry, (b) the boundary stresses calculated from the displacement field. x denotes the flow direction and z the vorticity direction.

result of the filtering, for spatially averaged measurements of the data we discard these notably lower values [1]. We were able to look qualitatively at local variation in the boundary stress, assuming the variation was large enough to not be lost to the already present spatial variation.

The recordings before and after the application of the shear stress allowed for compensation of the drift using a linear fit to the spatially averaged data. Most drift is seen when the shear stress is applied (Fig. 6.4), and therefore the drift is likely caused by either the glass coverslip or the PDMS layer rotating under stress. A raw data set, and another with drift compensation are shown in figure 6.4. The linear correction is then added to each individual element, under the assumption that the drift is the same across the whole image.

To calculate the stress at the upper surface we first consider the tensorial Hooke's law for an isotropic medium

$$\sigma_{ik} = \frac{E\nu}{(1-2\nu)(1+\nu)} u_{ll}\delta_{ik} + \frac{E}{1+\nu} u_{ik}, \tag{6.1}$$

where δ_{ik} is the Kronecker delta, E is the elastic modulus, ν is the Poisson ratio, σ_{ik} is the stress tensor, and u_{ik} is the strain tensor. We assume our PDMS film is essentially incompressible such that $\nu = 0.499$ [27, 121]. For PDMS, there is variation in the literature with $0.45 < \nu < 0.5$ [122, 123] for small strains $\gamma < 0.45$ it has been found that $\nu \approx 0.5$ (although we take $\nu = 0.499$ to avoid

[1] These lower values are a result of padding the data with zeros, which affects the filtering at the boundary.

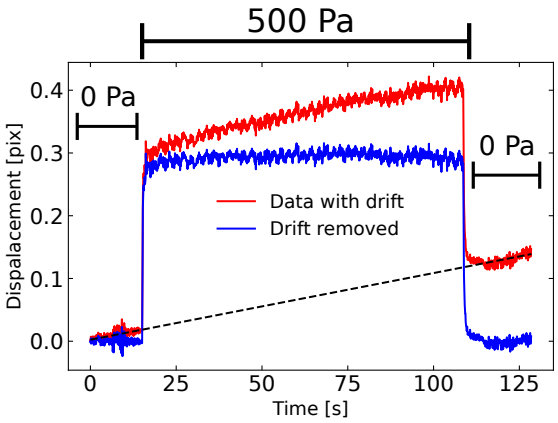

Figure 6.4 Pixel displacements over time measured at the boundary of a sheared suspension of silica suspended in 80 wt.% G/W. The sample shows drift over time, which is corrected using a linear fit (black, dashed) to the two regions under no shear.

divergent stresses) [2][124–126]. The equation for an elastic medium in equilibrium considering only external forces on the medium is

$$\frac{\partial \sigma_{ik}}{\partial x_k} = 0. \tag{6.2}$$

Applying equation 6.2 to equation 6.1 and using the relation $u_{ik} = \frac{1}{2}\left(\frac{\partial u_k}{\partial x_i} + \frac{\partial u_i}{\partial x_k}\right)$, this gives

$$(1 - 2\nu)\nabla^2 \vec{u} + \vec{\nabla}(\vec{\nabla}\vec{u}) = 0. \tag{6.3}$$

The external deformations acting on the medium are considered as boundary conditions. In our case the system is bounded below by the PDMS coated glass coverslip, where there is no displacement, and bounded above by the sheared material, where the displacement is measured from the bead displacement. By considering the boundary conditions and the Fourier transform of the above equation we arrive at;

$$\hat{\sigma}(\vec{k}, h) = \mathbf{Q}(\vec{k}, y_0, h)\hat{u}(\vec{k}, y_0) \tag{6.4}$$

where $\hat{u}$ is the Fourier transform of the displacement vector, $\hat{\sigma}$ is the Fourier transform of stress on the free surface, and $\mathbf{Q}$ is a tensor relating the two vectors, a full derivation of which is given by del Alamo et al. [127]. $\mathbf{Q}$ is of the form $E\mathbf{M}$, where E is the elastic modulus and $\mathbf{M}$ is a matrix. $\vec{k}$ is the wave vector in the x, z plane, h is the height of the PDMS free surface, and y_0 is the height of the

[2]The same value has been used or suggested in previous work on boundary stress microscopy using PDMS [27, 118].

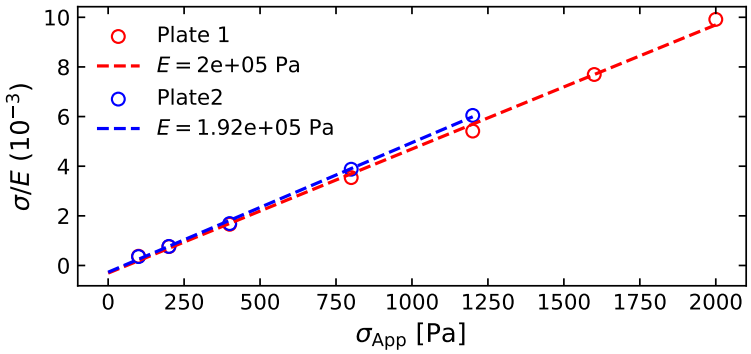

Figure 6.5 Linear fits to the average strain σ/E, (calculated using equation 6.4) used to calculated the elastic modulus of the PDMS layers used in sample set 1 and sample set 2.

beads. To calculate the stress σ, an inverse Fourier transform must be performed on the vector $\hat{\sigma}(\vec{k}, h)$. Although this method calculates both the boundary stress σ_{xy} in the flow direction and σ_{zy} in the vorticity direction, we only consider the stress measurements acting in the flow direction in all subsequent results. The calculation of the boundary stress assumes that the vertical displacement is minimal. Shear thickening dense suspensions show large normal stresses at high volume fractions [68], which could lead to large vertical displacements in the beads and subsequent errors in the stress calculations.

To calculate the boundary stress from the displacement data, the elastic modulus of the substrate needs to be known. To measure the elastic modulus calibration measurements were performed using a Newtonian fluid; pure glycerol was chosen as it has a high viscosity and therefore high stresses can be applied to it. Unlike silicone oils, glycerol has low wetting with the PDMS which makes cleaning easier, and is more similar to the G/W solvent used within the particle suspensions.

The tensor $\mathbf{Q}$ is linearly dependent on the elastic modulus E (such that $\mathbf{Q} = E\tilde{\mathbf{Q}}$), therefore we find E by measuring the displacements for a Newtonian fluid (where we should see uniform stress across the viewing window) at various apparent stresses and calculating how $\langle\sigma_{xy}\rangle/E$ varies with the apparent stress σ_{App}. We then fitted a straight line to the data to calculate E (Fig. 6.5). The linear fits to the measured local stresses show good agreement with the data (Fig. 6.5). We obtain two elastic moduli for the different PDMS plates used (plate 1 was used with sample set 1, plate 2 with sample set 2), which are similar values, with clear overlap in the data at low apparent stresses. To reduce the stiffness of the PDMS a low curing ratio (1:35) was used [27] this allowed for more sensitive measurement of the boundary stress.

6.3 Boundary Stress Microscopy

Firstly we shall look at temporally and spatially averaged boundary stresses. Although the measurement window is a 1×1mm square, we consider the average over the viewing window to be a point-like local stress value on the lower boundary of the material. Simple force balance tells us that the apparent stress at the upper boundary should be the same as the spatial average of the local stresses at the lower boundary, and for the case of a uniformly sheared fluid, the local stresses should be spatially invariant. Similarly, the stress at the lower boundary should increase linearly with the increasing stress at the upper boundary, so the local stress should double if the apparent stress is doubled. We see such a linear relation for the calibration of the Newtonian glycerol fluid in figure 6.5.

6.3.1 Plate Misalignment and Newtonian Fluid Rheometry: A Theoretical Model

The effects of plate misalignment on Newtonian fluids (and fluids of other behaviours) have been studied in depth using the relevant constitutive equations [102]. Plate misalignment is not generally considered in standard rheological measurements, unless measurements are taken at small gap heights and high shear, where it is necessary to account for the misalignment even in conventional (unmodified) rheometer configurations [128–130]. Previous work using boundary stress microscopy did not attempt to account for plate misalignment, as none of the work was performed at such high shear rates [27, 75, 76]. In our rheoimaging setup used for boundary stress microscopy, misalignment issues are likely to be more significant due to the modification to the bottom plate required to facilitate imaging. In this section we will consider a misaligned bottom plate in a cone-plate geometry to test what effects such a misalignment would have on the bulk and local stresses for both Newtonian and shear thickening fluids. Using a WC-type model of a shear thickening fluid with the assumption of a misaligned cone-plate geometry, we will show that a small misalignment angle can lead to large variations in the local stress of the suspension.

In chapter 3 we considered how the torque τ and rotation rate Ω relate to the stress σ and the shear rate $\dot{\gamma}$ for an idealised, perfectly aligned cone plate-geometry, and showed that these quantities are uniform across the material. In this chapter,

where we consider plate misalignment, we now distinguish between the local stress $\sigma(\vec{r})$ and local shear rate $\dot{\gamma}(\vec{r})$ which can vary with position, and the apparent values σ_{App} and $\dot{\gamma}_{\text{App}}$ reported by the rheometer assuming perfect alignment. As discussed in chapter 2, the shear rate is the velocity gradient through the material, which for planar Couette flow can be expressed as

$$\dot{\gamma} = \frac{V}{h} = \frac{\Omega r}{h}$$

where V is the velocity at the top of the material, Ω is the rotation rate in rad/s, and h is the gap height. For an ideal (perfectly aligned) cone geometry with a cone angle α_c the height h_{cone} is given as:

$$h_{\text{cone}} = r\tan(\alpha_c).$$

Combining the above equations we get

$$\dot{\gamma}_{\text{App}} = \frac{\Omega}{\tan(\alpha_c)},$$

giving a local shear rate in the idealised cone-plate geometry that is radially independent (in contrast to a parallel-plate geometry). From here we can derive equation 3.2. The net torque on the tool can be calculated as the integral of the shear stress σ over the plate area

$$\tau = \int_0^R \int_0^{2\pi} \sigma_{\text{App}} r^2 d\beta dr \tag{6.5}$$

where β is the angle around the rheometer tool (Fig. 6.6), and R is the outer radius of the rheometer tool. We can rearrange equation 6.5 to get equation 3.2, which we reiterate here:

$$\sigma_{\text{App}} = \frac{3\tau}{2\pi R^3}.$$

Using these equations we get the apparent viscosity of the sample

$$\eta_{\text{App}} = \frac{\sigma_{\text{App}}}{\dot{\gamma}_{\text{App}}} = \frac{3\tau\tan(\alpha_c)}{2\pi R^3\Omega}. \tag{6.6}$$

Figure 6.6 shows a schematic of a misaligned cone-plate setup, which will be used as a reference to the parameters discussed in the description of the effect of the plate misalignment on the rheology. For a misaligned bottom plate we must consider the variation in the height from the horizontal plane h_{plate}. We consider

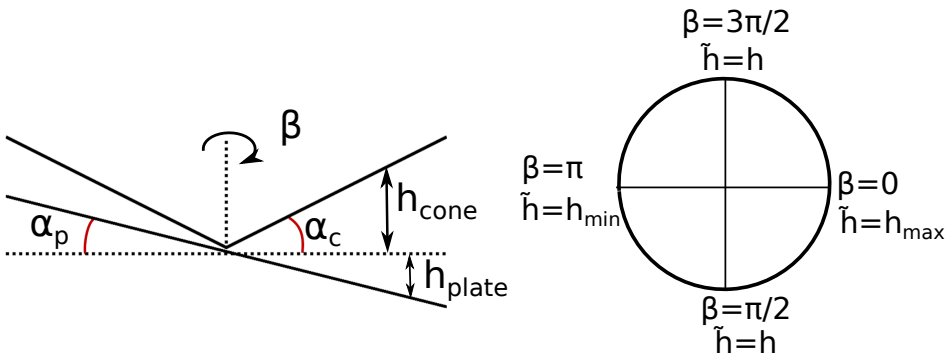

Figure 6.6 Schematic of a cone-plate rheometer geometry with a misaligned bottom plate, it is assumed that the truncation gap is the same as if the bottom plate were aligned. The angles are exaggerated, the dashed line represents the horizontal. For the tool used in this work $\alpha_c = 1^\circ = 0.0175\,\text{rad}$.

a circular disk rotated by an angle α_p from the horizontal, such that the diameter line intersects with the 'tip' of the cone, giving

$$h_{\text{plate}}(\beta) = r\tan(\alpha_p)\cos(\beta) \tag{6.7}$$

where h_{plate} is maximal at $\beta = 0\,\text{rad}$ and minimal at $\beta = \pi\text{rad}$ as described in figure 6.6. Therefore the gap height is the sum of the plate height and the cone height (we simplify $h_{\text{cone}} = h_{\text{c}}$ and $h_{\text{plate}} = h_{\text{p}}$)

$$\tilde{h}(\beta) = h_{\text{c}} + h_{\text{p}} = r[\tan(\alpha_c) + \tan(\alpha_p)\cos(\beta)]. \tag{6.8}$$

Here we assume that the flow can still be approximated as Couette flow. The assumption of Couette flow can be made in the limit of $h_{\text{c}} \ll h_{\text{p}}^{\text{max}}$ (where $h_{\text{p}}^{\text{max}}$ is the maximum value of h_{p}). The limit can also be expressed in terms of the angles α_c and α_p as $\alpha_p >> \alpha_c$. By taking the equation for the velocity profile for the lubrication approximation [131]

$$\frac{\mathrm{d}U_x}{\mathrm{d}y} = \frac{2V}{\tilde{h}(\beta)^2}\left[\frac{3h_{\text{min}}h_{\text{max}}(2y - \tilde{h}(\beta))}{\tilde{h}(\beta)(h_{\text{min}} - h_{\text{max}})} + 2\tilde{h}(\beta) - 3y\right], \tag{6.9}$$

where U_x is the velocity profile across along the gradient direction. We take $h_{\text{min}} = h_{\text{c}} - \delta$, $h_{\text{max}} = h_{\text{c}} + \delta$, and $\delta \ll h_{\text{c}}$ such that $\delta/h_{\text{c}} \ll 1$ can be ignored in

the first order [3]. Equation 6.9 simplifies to

$$\dot{\gamma} = \frac{\mathrm{d}\gamma}{\mathrm{d}t} = \frac{V}{\tilde{h}(\beta)},$$

which is the same as equation 2.2, though with an angular-dependent height.

Although from the lubrication approximation (which assumes small angles, $\alpha_p \ll 1$) we would still expect a spatially dependent shear rate, for shear thickening dense suspensions there is no simple agreed upon constitutive model, therefore to allow for calculation of the effect of misalignment on a shear thickening dense suspension we assume Couette flow. Taking equations 6.8 and 3.1, we get a shear rate that varies with the angle β,

$$\dot{\gamma}(\beta) = \frac{\Omega}{\tan(\alpha_c) + \tan(\alpha_p)\cos(\beta)}. \tag{6.10}$$

Due to the nature of the rheometer setup, Ω is constant across the bulk material. where σ is the stress of that area element. For a perfectly aligned plate the shear rate $\dot{\gamma}$ is constant around the rheometer tool, and therefore the local shear stress $\sigma = \sigma(\dot{\gamma})$ is also constant such that the apparent stress reported by the rheometer reflects the true stress exerted by the sample even for non-Newtonian materials. For a misaligned geometry $\dot{\gamma}$ varies with angular position around the tool $\dot{\gamma} = \dot{\gamma}(\beta)$. If we instead assume that the local stress can be expressed as $\sigma = \eta(\sigma)\dot{\gamma}(\beta)$, with $\eta(\sigma)$ the local stress dependent viscosity, as in the Wyart-Cates model, then we can express the torque balance condition as

$$\tau = 2\int_0^R \int_0^\pi \eta(\sigma)\dot{\gamma}(\beta) r^2 d\beta dr, \tag{6.11}$$

(as the system is symmetric we take the integral through half the geometry and double it) or equivalently express the apparent stress reported by the rheometer as,

$$\sigma_{\mathrm{App}} = \frac{1}{\pi}\int_0^\pi \frac{\eta(\sigma)\Omega}{\tan(\alpha_c) + \tan(\alpha_p)\cos(\beta)} d\beta. \tag{6.12}$$

From equation 6.12, σ_{App} is the angular average of the shear stress σ.

For low angle of misalignment α_p there is vary little variation in the bulk stress measured, which is to be expected. To see a significant increase in the apparent viscosity η_{App} (Fig. 6.7(a)), we have to consider values of α_p which are too large

[3] As $\delta = r\alpha_p$ as a maximum and $h_c = r\alpha_p$ in the small angle limit, which is equivalent to $\alpha_c >> \alpha_p$.

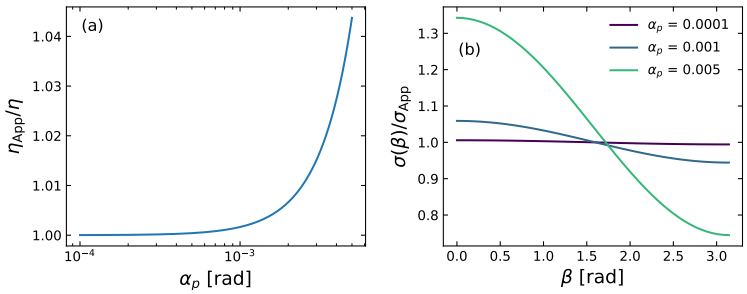

Figure 6.7 Analytical result of equation modelling the effect of misalignment on the rheology of a Newtonian fluid in a cone- plate rheometer with cone angle $\alpha_c = 1° \approx 0.0174\,\text{rad}$. (a) The variation in apparent viscosity relative (measured) η_{rmApp} to the actual viscosity η, (b) the angular variation in the local stress $\sigma(\beta)$ relative to the apparent (bulk) stress σ_{App}.

to satisfy the approximation $\alpha_p \ll \alpha_c \approx 0.017$. Even for a small misalignment ($\alpha_p \approx 10^{-3}\,\text{rad}$), which will have a minimal effect on the measured bulk viscosity, we may still see a notable effect on the BSM calibration procedure. The angular variation in the local stress σ becomes relatively large (Fig. 6.7(b)), which would effect calibration as it involves a local stress measurement at a given angular position.

The Effect of Plate Misalignment on BSM Calibration

The elastic modulus of the PDMS substrate was calculated by performing BSM measurements on a Newtonian fluid; however, as shown in figure 6.8, a Newtonian fluid's local stress is affected significantly by plate misalignment. We used the apparent stress σ_{App} to calculate the substrate elastic modulus, which does not reflect the local stress for a misaligned setup. If the BSM measurement was taken on a misaligned setup, then the elastic modulus would be miscalculated depending on the the radial position (Fig. 6.7(b)) and the misalignment angle (Fig. 6.8).

6.3.2 The Predicted Effect of Plate Misalignment on Bulk Shear Thickening Bulk

In our simplified model of a misaligned cone-plate geometry, the local stress is determined by the local shear rate $\dot{\gamma}(\beta)$ through the local rheology $\sigma(\beta) = \eta\dot{\gamma}$ so that in principle any empirical constitutive relation $\eta(\dot{\gamma})$ could be used to compute

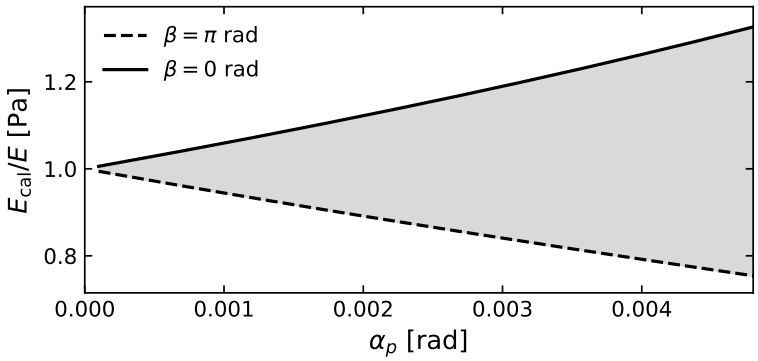

Figure 6.8 Measured elastic modulus from calibration E_{cal} relative to the actual elastic modulus E from the model of a misaligned bottom plate. The maximum and minimum values of the calibrated measurement E_{cal}, which would be measured at $\beta = 0, \pi$ rad.

the stress at a given apparent stress σ_{App}. To investigate the specific case of shear thickening suspensions we use the Wyart-Cates model with parameters taken from fits to our experimental flow curves. As shown in the previous two chapters, the Wyart-Cates model can closely match the observed steady state thickening, and the use of a physics based model gives us some confidence when extrapolating to significantly higher stresses than those measured in our flow curves.

Using the Wyart-Cates model to express the local stress presents a computational problem as the Wyart-Cates viscosity is itself dependant on the stress $\eta = \eta_{\text{WC}}(\sigma)$. We assume we can consider the rheology locally such that the local stress is given by the transcendental relation $\sigma = \eta_{\text{WC}}(\sigma)\dot{\gamma}$ with η_{WC} given by equations 2.31, 2.29, and 2.11 which we reiterate here.

$$f = \exp\left(-\left(\frac{\sigma^*}{\sigma}\right)^{\beta}\right),$$

$$\phi_J = f\phi_M + (1-f)\phi_0,$$

$$\eta = \eta_s A\left(1 - \frac{\phi}{\phi_J}\right)^{-2}.$$

The local stress at an angle β for a material with a stress dependent viscosity would be expressed as

$$\sigma(\beta) = \frac{\eta(\sigma)\Omega}{\tan(\alpha_c) + \tan(\alpha_p)\cos(\beta)}, \tag{6.13}$$

which presents a computational problem if the relation $\eta(\sigma)$ is not simple (like the Wyart-Cates model). To solve these equations simultaneously we use a recursive

method such that

$$\sigma^{i+1}(\beta) = \frac{\eta(\sigma^i(\beta))\Omega}{\tan(\alpha_c) + \tan(\alpha_p)\cos(\beta)}, \tag{6.14}$$

with initial parameters assuming perfect alignment. We then allow the equation to converge for a range of equally spaced β values, and take the average of these values as the apparent stress σ_{App}. Such a result also assumes that the regions are independent; given a relaxation time $t_r = 0.1\,\text{s}$ (Ch. 5) would require an apparent shear rate $\dot{\gamma}_{\text{App}} < 0.17\,\text{s}^{-1}$ for the system to relax between the radial positions considered ($\delta\beta \approx 0.017\,\text{rad}$).

6.3.3 The Effect of Misalignment on Local Shear Thickening Rheology

Misalignment affects bulk rheology as the measured rotation rate, from which the $\dot{\gamma}_{\text{App}}$ is calculated, is lower for a given σ_{App} in a misaligned geometry (Fig. 6.7). However our model does not predict that the misalignment angle will noticeably affect the form of the bulk rheology, with Newtonian fluids still expected to show a constant viscosity with increasing apparent stress/shear rate. Here we consider if the same will be true of shear thickening suspensions. Shear thickening suspensions have been shown to have stress dependent viscosities [62, 65, 80], and therefore the effect of plate misalignment, where the idea that local stress is not constant, is not necessarily intuitive. As with a Newtonian fluid, the model predicts that increasing the misalignment angle increases the apparent viscosity of a shear thickening suspension (Fig. 6.9), and does not noticeably change the form of the shear thickening flow curves. Similarly, our model predicts that increasing the volume fraction (and therefore the degree of thickening) increases the effect of the misalignment on the measured apparent viscosity (Fig. 6.9(b)). Although the model predicts a clear deviation from a model flow curve, assuming perfectly aligned geometry, the variation is not large enough for it to be noticeably distinguishable from a standard shear thickening curve (Fig. 6.9(a,b)). The lack of large change in the bulk behaviour may explain why the effect of misalignment has not been considered in shear thickening dense suspension rheology until this point.

The model predicts that the local rheology will vary with the angle around the rheometer tool β, with a lower local stress at $\beta = \pi$ (where the gap height is

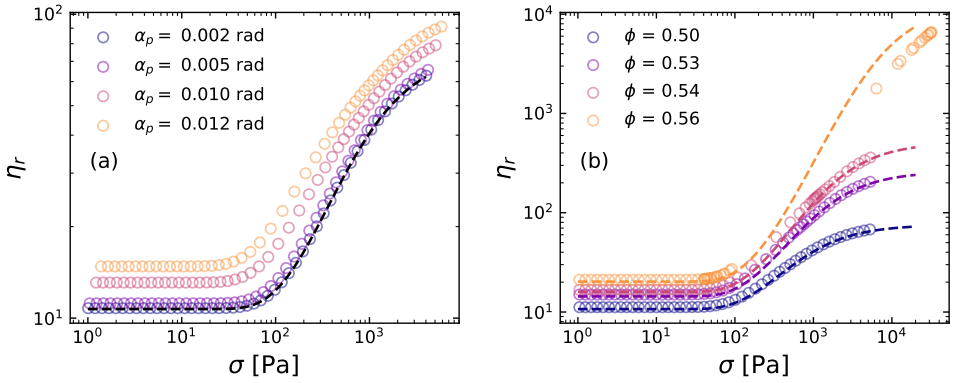

Figure 6.9 Steady state flow curves using the model for plate misalignment. The graphs show the variation of the apparent (relative) viscosity η_r with increasing apparent stress σ_{app}; (a) for increasing misalignment angle α_p, (b) and increasing volume fraction ϕ. (a,b) The dashed lines indicate the resulting Wyart-Cates model prediction assuming no misalignment.

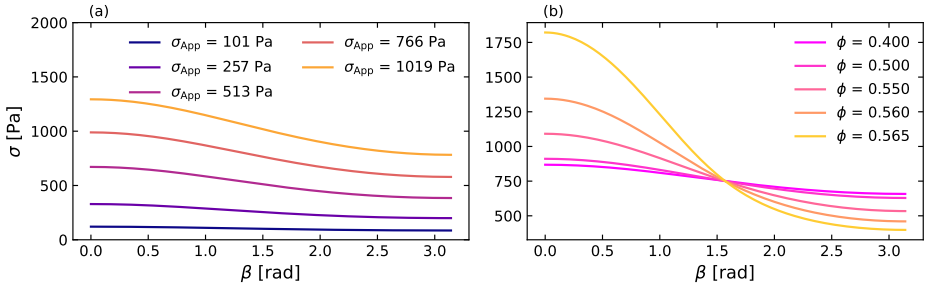

Figure 6.10 Variation of the radially varying average local stress calculated using the model for plate misalignment. The graphs show the variation with of the local stress σ with the angle β round the rheometer tool; (a) for increasing apparent stress σ_{App}, (b) and increasing volume fraction ϕ.

maximal), and a higher local stress at $\beta = 0$ (where the gap height is minimal) (Fig. 6.10(a,b)). Increasing the apparent stress, or the volume fraction of the suspension, increases the extent to which the local stress will be higher or lower than the apparent stress (Fig. 6.10(a, b), respectively).

6.4 The Effect of Plate Misalignment on Measured Local Stress Measurements

Two sets of measurements were taken at two different times using samples diluted from two different stock solutions. Sample set 1 consisted of samples with volume fractions closely spaced in the range $0.55 < \phi < 0.58$, while sample set 2 consisted of samples with $\phi = 0.300,\ 0.400,\ 0.498$ and 0.561. Each set of measurements used a different PDMS-coated glass coverslip with the measurement sets taken approximately 5 months apart; in the intervening period the rheo-confocal setup will have been readjusted multiple times, and switched between rheo-confocal and standard confocal setups and back by other users. The elastic moduli of the PDMS-coated coverslips were both measured using the calibration method discussed previously, which produced similar values for the elastic moduli ($E_1 = 2.0 \times 10^5$ Pa, $E_2 = 1.9 \times 10^5$ Pa). Despite similar bulk rheology and PDMS plate characteristics, we obtain wildly different local stress measurements. We will now show how small changes in the plate misalignment can account for these disparate results.

6.4.1 The Effect of the Boundary Stress Microscopy Setup on Bulk Rheology

A WC-type model was fitted to all flow curves where $\phi < \phi_M$ using the method discussed in chapter 4, although ϕ_M was fixed for sample set 2 because the high stress plateaus are not visible due to the lower maximum apparent stress. Here we fit the WC-type model to our shear thickening curves as done previously (Ch. 4), to extract parameters that we will later be used with the model of plate misalignment (Sec. 6.3.1).

Sample set 1 taken on the metal bottom plate shows no deviation from standard shear thickening behaviour (Fig. 6.11(a)), though there is a clear decrease in σ^*

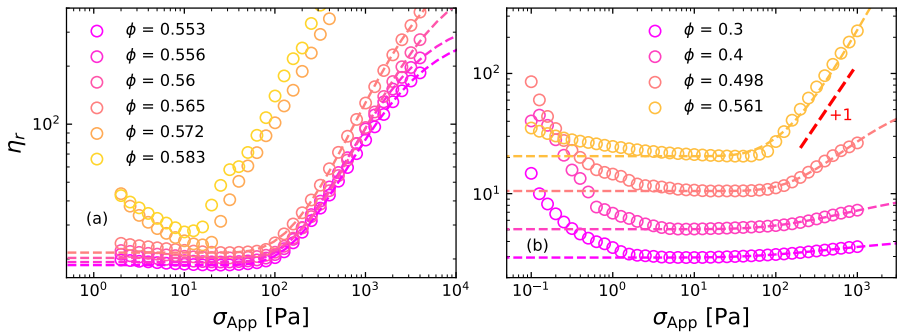

Figure 6.11 Bulk flow curves $\eta_r(\sigma_{App})$ for shear thickening suspensions at indicated volume fractions ϕ. (a) Sample set 1 uses a typical roughened metal bottom plate. (b) Sample set 2 uses a PDMS coated coverslip which was used for BSM measurements. Dashed lines show fits to the Wyart-Cates model.

for samples where $\phi > \phi_{DST}$ similar to results discussed in the previous chapter (Ch. 5). The WC fits to the flow curves show good agreement with the data (Fig. 6.11(a), dashed lines), and even appear to capture the small changes in the volume fraction.

The flow curves for sample set 2 were taken on the PDMS coated coverslip, and show a clearer deviation from standard shear thickening (Fig. 6.11(b)); there is pronounced shear thinning at low apparent stresses, which is considerably stronger at low volume fractions, there is also stronger shear thickening than expected for the low volume fractions [68]. As these results were taken on the PDMS coated coverslip the maximum stress applied was limited to avoid damaging the PDMS, which can lead to more inaccurate values of ϕ_M when fitting. Therefore ϕ_M was fixed $\phi_M = 0.565$ for these samples (Fig. 6.11(b), (dashed lines)).

The shear thinning in sample set 2 (Fig. 6.11(b)) was attributed to another problem with the BSM setup used. The system height is 'zeroed' based on the normal force experienced by the rheometer tool (where 0.1 N is taken as contact). For the standard metal bottom plate the normal force is an accurate measurement of contact, as the metal deforms minimally at 0.1 N normal force. The PDMS substrate will deform noticeably at a normal force of 0.1 N and therefore when the tool is moved to the measurement height (48 µm) there may still be some contact. Any contact will be measured by the tool as a high viscosity. The setup with no sample the system still experiences resistance to motion at low stresses.

The rheology also shows strong hysteresis at high stresses, which becomes less

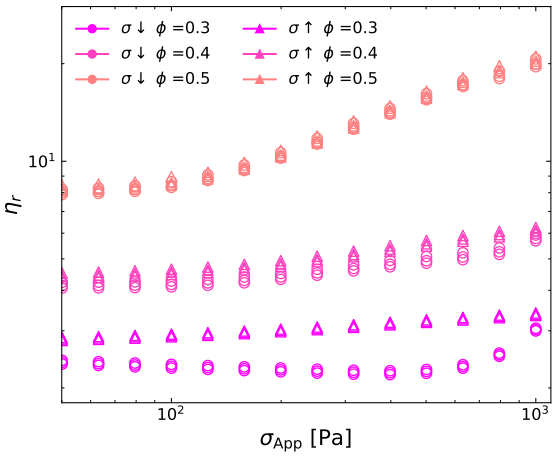

Figure 6.12 High stress regions of the shear thickening rheology of samples of silica in G/W at indicated volume fractions ϕ. The measurements were taken on a PDMS substrate with fluorescent beads bonded to the upper surface for boundary stress measurements. The curves are labelled with $\sigma\uparrow$ to indicate measurements taken with the stress increased between steps and $\sigma\downarrow$ to indicate measurements taken with decreasing stress.

prominent with increasing volume fraction (Fig. 6.12). The data where the stress decreases dramatically on the down sweep was discarded for $\phi = 0.300, 0.400$, as these show clear deviation from standard shear thickening. The hysteresis at low ϕ is very likely related to the use of the elastic substrate, as hysteresis is not usually observed at low ϕ. Such hysteresis could result from slip due to the low roughness of the elastic substrate.

6.4.2 Comparing Local and Bulk Stress Measurements: Measured Effect of Plate Misalignment

To compare the measured results to the above model, we average the local stress when the sample is under shear for different apparent stresses. We assume that the average of the local stress can be modelled as being at some angular position around the rheometer geometry [4] and attempt to fit our model to the data assuming that the angular position is $\beta = 0, \pi$. We are thus limited to a single fitting parameter α_p, which we allow to vary for each sample. We note that the rheometer lower plate had to be removed and cleaned between samples, which could easily allow for variation in the angle between different

[4] In reality the imaging window is of angular extent $\Delta\beta \approx 4.5°$.

ϕ	α_p [mrad]
0.553	0.3
0.556	1.5
0.560	1.2
0.565	1.8

Table 6.1 The volume fraction of the samples, and the misalignment angles α_p found by fitting equation 6.14 to averaged boundary stress data for sample set 1.

sample measurements.

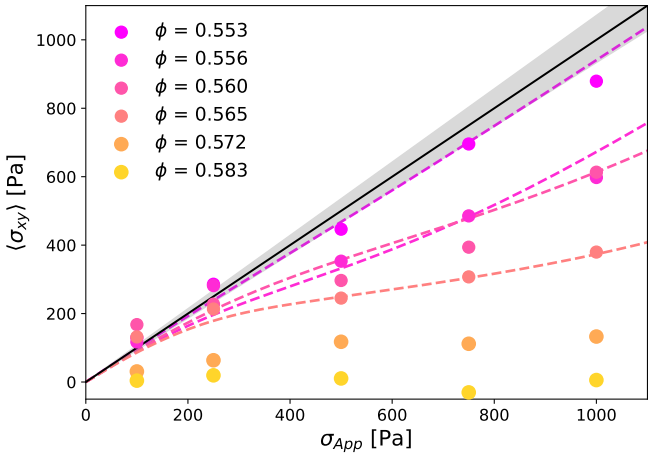

Figure 6.13 Average local stress σ_{BSM}, measured using boundary stress microscopy, against applied bulk stress σ_{App} for shear thickening suspensions at indicated ϕ from sample set 1 (filled circles). Solid black line indicates $\sigma_{\mathrm{BSM}} = \sigma_{\mathrm{App}}$. Dashed lines show fits to the local stress using Eq. 6.14 with $\eta_{\mathrm{WC}}(\sigma, \phi)$ determined from fits to bulk flow curves (Fig. 6.11) assuming $\beta = 0$ (e.g. $h = h_{\mathrm{max}}$). Fitted values of the misalignment α_p are shown in table 6.1. Grey shading indicates uncertainty in the plate elastic modulus calibration computed from the average of our fits $\bar{\alpha}_p = 1.2 \times 10^{-3}$ rad values.

There is a clear increase in the extent of the mismatch between the local and apparent stresses with increasing ϕ, a trend which continues above ϕ_{DST} (Fig. 6.13). The trend is not fully accounted for by the changing volume fraction. To account for the discrepancy in apparent and local stress, the local gap height must be higher than the average gap height. The variation in the calculated misalignment angle is relatively large compared to the values themselves (table 6.1). But the absolute variation is only on the order of 0.1° [5].

[5] A change of about 0.1° would be a difference of 150 µm in the heights at either edge of the home built platform.

The measured average boundary stress is massively overestimated for the $\phi = 0.561$ samples (Fig. 6.14), which is consistent with the deviation getting larger with increasing volume fractions. Such a large, non-linear increase in the measured local stress is consistent with a smaller than expected gap height due to plate misalignment. For the $\phi = 0.561$ sample the numerical solution to the model described previously (Eq. 6.14) breaks down, therefore to actually obtain a fit we use a value of $\phi_M = 0.58$, which is consistent with the measured value of ϕ_M found for sample set 1, though it is not the fixed value of 0.565 used for Wyart-Cates fitting of sample set 2. It is unsurprising that the model breaks down at high volume fractions, because the model will predict discontinuous thickening where small changes in the local shear rate lead to large changes in the local stress.

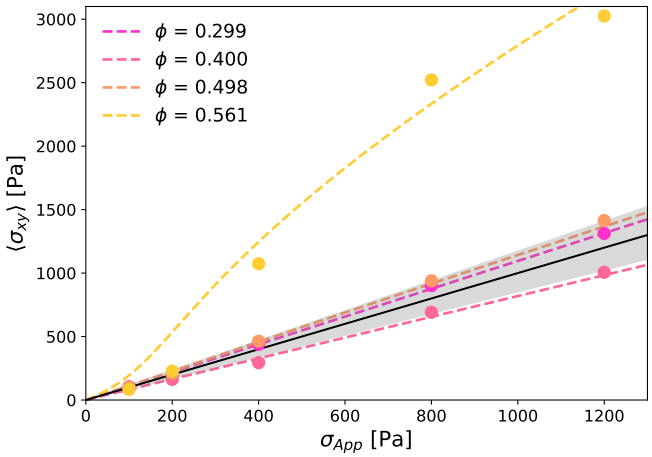

Figure 6.14 Average local stress σ_{BSM}, measured using boundary stress microscopy, against applied bulk stress σ_{App} for shear thickening suspensions at indicated ϕ from sample set 2 (filled circles). Solid black line indicates $\sigma_{\mathrm{BSM}} = \sigma_{\mathrm{App}}$. Dashed lines show fits to the local stress using Eq. 6.14 with $\eta_{\mathrm{WC}}(\sigma, \phi)$ determined from fits to bulk flow curves (Fig. 6.11), except for $\phi = 0.561$ where $\phi_M = 0.58$ was used to allow the model to converge, assuming $\beta = \pi$ (e.g. $h = h_{\mathrm{min}}$). Fitted values of the misalignment α_p are shown in table 6.2. Grey shading indicates uncertainty in the plate elastic modulus calibration computed from the average of our fits $\bar{\alpha}_p = 2.75 \times 10^{-3}$ rad values.

Although the model can account for the small variation in the average boundary stress seen at low volume fractions ($\phi = 0.299,\ 0.400$ and 0.498) (Fig. 6.14), this could also be a result of errors in the elastic modulus. As predicted by the model, the weaker shear thickening due to the lower volume fractions, the lower the extent of the deviation of the local stress from the apparent stress. Notably the

ϕ	α_p [mrad]]
0.30	1.5
0.40	−3.0
0.50	1.5
0.56	6

Table 6.2 The volume fraction of the samples, and the misalignment angles α_p found by fitting equation 6.14 to averaged boundary stress data for sample set 2.

sample with $\phi = 0.4$ appears to show an underestimate of the apparent stress. The trend in the lower deviation is not consistent across the range of volume fractions measured, which is attributed to variation in the misalignment angle.

Table 6.2 gives the plate misalignment found from fitting the local stress data to the misalignment model. The values vary widely, though all these fits assume that we are at the extremes of the misalignment, and therefore are the minimum values of α_p. The variation in the gap height appears to be quite dramatic for the larger angles, but if we consider the 50 mm radius glass coverslips used in the experiment, we only need a difference in height between the two edges of approximately 0.25 mm for the misalignment angle to be 5×10^{-3} rad. Such a small difference would not be visible with the naked eye, or noticeable when loading samples.

6.5 Local Stress Measurements and Transient Fluctuations

In the previous section we have shown that local stress measurements are strongly affected by small plate misalignments. Here we compare our own local stress measurements, for data where the plate misalignment has been shown, to previous results measuring local stress fluctuations in shear thickening suspensions of silica using BSM.

Spatially averaged stress measurements show clear transient stress fluctuations (Fig. 6.15(a)) similar to those previously observed (Fig. 6.15(b)) [27]. Both figures show clear spikes in the local stress which increase in frequency with increasing apparent stress. The peaks of the spatially averaged stresses of the fluctuations are also of similar magnitudes. We reiterate that time averages of our data give

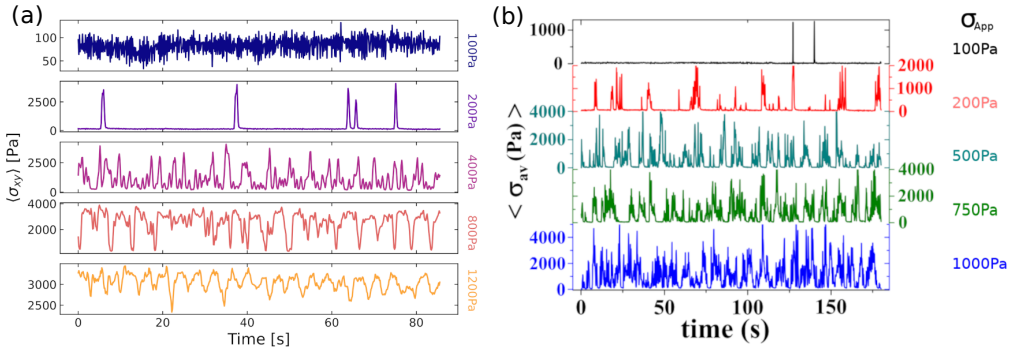

Figure 6.15 Spatially averaged boundary stresses in the flow direction $\langle\sigma_{xy}\rangle(t)$, $\langle\sigma_{\mathrm{av}}\rangle(t)$, (a) for suspensions made in a setup with a likely misaligned bottom rheometer plate, (b) and results from Rathee et al. [27]. Both are measurements for suspensions of silica particles in 80 wt.% G/W with size (a) $R = 0.75\,\mu\mathrm{m}$ and (b) $R = 0.48\,\mu\mathrm{m}$. The time averaged apparent stresses are labelled on the right of each figure.

spatially averaged stresses that are significantly larger than the apparent stresses.

Looking at the boundary stress measurements we see that the shape and motion of the stress fluctuations we observed (Fig. 6.16) are similar to those observed by Rathee et al. [27] (Fig. 6.17). Although our results show a significantly large spatial extent than previous results, a difference that is larger at higher apparent stresses. This difference may be a result of the different particle sizes used, or this could be a result of differences in the alignment of the rheometer tools.

Comparison of cross correlations for the fluctuations observed in figures 6.16 and 6.17 both show similar trends to the left in the flow direction. The speed relative to the rotational speed could not be calculated as the radial position of our measurement is was not known. The larger extent of our fluctuations is clearer in the significantly broader peaks in the cross correlation seen for our data (Fig. 6.18).

Although the fluctuations at low apparent stresses $\sigma < 1200\,\mathrm{Pa}$ for sample set 1 are erratic (Fig. 6.15(a)), for $\sigma = 1200\,\mathrm{Pa}$ we observe clear coupling between the rheometer tool rotation rate and the local stress (Fig. 6.19).

Similarly, there are notable oscillations at low volume fractions for sample set 2. By comparing the Fourier transforms of the shear rate, rotation ($\cos(\theta)$), and the local boundary stress measurements, we see that peaks in the frequency line up firstly at the time-averaged rotation frequency ($\nu_{\cos(\theta)} \approx 0.5\,\mathrm{Hz}$ and $0.56\,\mathrm{Hz}$ respectively), and at the frequency of the shear rate oscillations ($\nu_{\dot{\gamma}} \approx 0.2\,\mathrm{Hz}$),

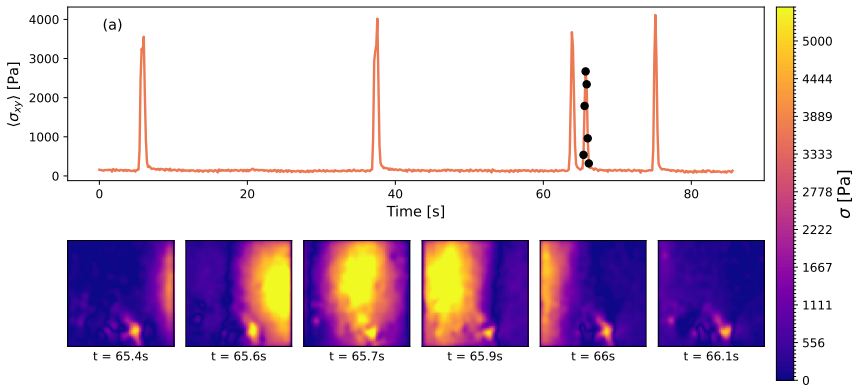

Figure 6.16 Spatially averaged local boundary stress $\langle\sigma_{xy}\rangle$ against time t, with full boundary stress images at given times indicated by black circles. Measurements are for suspensions of silica in glycerol water at volume fraction $\phi = 0.561$, part of sample set 1, with (a) $\sigma_{\mathrm{App}} = 200\,\mathrm{Pa}$, (b) $\sigma_{\mathrm{App}} = 400\,\mathrm{Pa}$. The color bar indicates the local stress in the BSM images.

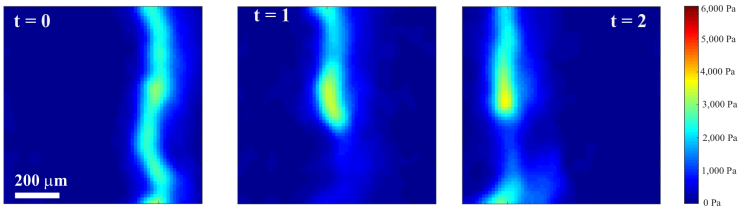

Figure 6.17 Snapshot of boundary stress in the flow direction for three consecutive time points measured by Rathee et al. [27], the stress scale is labelled on the right.

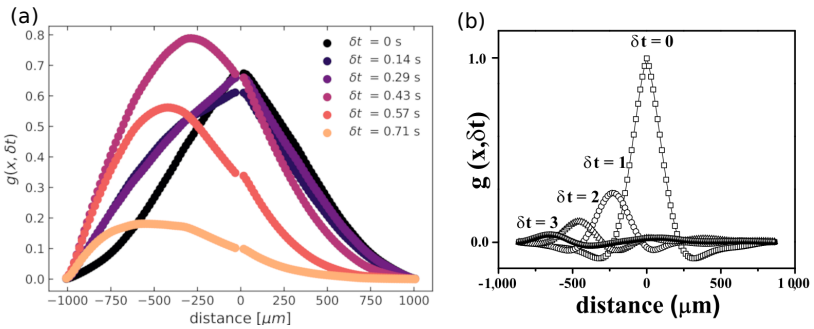

Figure 6.18 Cross correlation between 5 subsequent BSM frames starting with $t = 51.1\,\mathrm{s}$ (Fig. 6.16(a)). The time between the frames indicated in the legend. Data from sample set 2, $\phi = 0.561$ with $\sigma_{\mathrm{App}} = 200\,\mathrm{Pa}$.

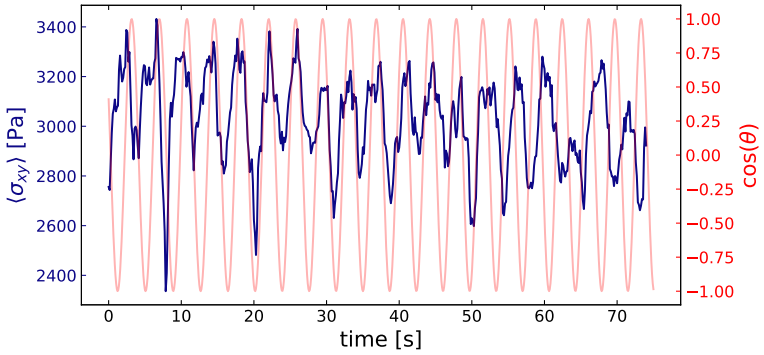

Figure 6.19 Spatially averaged boundary stress measurements for suspensions of silica in glycerol water against $\cos(\theta)$ where $\theta = \sum \delta t \dot{\theta}(t)$ where $\delta(\theta)$ is the time step between measurements, and $\dot{\theta}(t)$ is the rate at the instant t. Data for samples set 2 $\phi = 0.561$, apparent stress $\sigma_{\mathrm{App}} = 1200\,\mathrm{Pa}$.

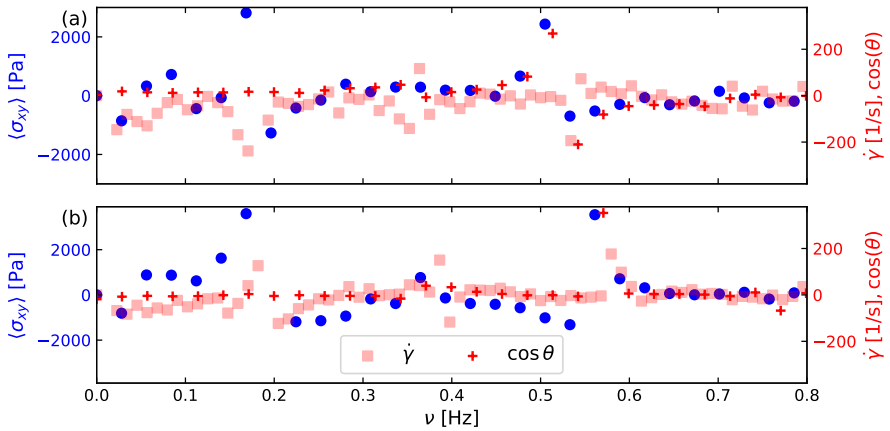

Figure 6.20 Boundary stress (blue, left axis), shear rate $\dot{\gamma}$, and $\cos(\theta)$ (red, right axis, legend) against frequency calculated by fast Fourier transforms of the relevant variable. The data is taken at two different apparent stresses (a) $\sigma_{\mathrm{App}} = 750\,\mathrm{Pa}$ and $\nu_{\mathrm{rheo}} = 0.52\,\mathrm{s}^{-1}$, (b) $\sigma_{\mathrm{App}} = 1000\,\mathrm{Pa}$ and $\nu_{\mathrm{rheo}} = 0.57\,\mathrm{s}^{-1}$.

though with phase differences (Fig. 6.20).

Coupling to the rotation rate of the tool has previously been seen in the motion of large transient bands [27] and in measurements taken with a plate-plate geometry [75]. The coupling of these high stress regions was attributed to the motion of solidlike phases which are attached to the rheometer tools [75]. Here we suggest that similar solidlike phases cause the slowing of the rheometer tool when they reach the constriction, which explains the coupling of our local stress measurements at the constriction (Sec. 6.4.2) with the global shear rate and the rheometer rotation (Fig. 6.20).

6.6 Conclusions and Outlook

Boundary stress measurements have previously been used to try and improve our understanding of shear thickening suspensions by opening a window into local stress variation [27, 75, 76]. We present a simple model, alongside supporting data, to show that local rheological measurements do not necessarily reflect the bulk rheology of the system due to plate misalignment. We show that depending on the local gap height the local stress measurement is either significantly higher or lower than the apparent stress (in effect the average of the local stresses), and that this effect is exaggerated in shear thickening suspensions due to dependence of their viscosity on the stress. To achieve noticeable affects of misalignment, only misalignment of angles of order 10^{-3} rad are necessary at moderate volume fractions $\phi \geq 0.5$, with this value becoming smaller with increasing ϕ. Such misalignments are almost unavoidable in all cone-plate rheometer setups, and therefore any consideration of local behavior in such a setup must record the misalignment, local gap height, and angular position to be of any use.

We subsequently consider our boundary stress measurements of silica suspensions, some of which show transient stresses similar to previous work [27, 75, 76], whilst considering the effect of the local gap height on our measurements. Our measurements suggest that large transient boundary stress fluctuations are not observed at volume fractions far below the DST regime, but these fluctuations may result from the local shear-rate/stress variation, and may not be present in an ideal geometry. We do see clear transient stress fluctuations close to and significantly into the DST regime, and these results are observed for both higher and lower local gap heights. The results also suggest that the higher local stress

has allowed for observation of boundary stresses close to the fully shear thickened state.

Although our results suggest limitations in the measurement of local behaviour in cone-plate geometries, there is certainly more research to be done looking at the coupling of the tool rotation and local stress measured. Furthermore, measurements of either the whole lower boundary, or measurements with known misalignment and angular (and radial) position will help to better understand the behaviour of shear thickening systems in none-couette type flow.

Chapter 7

Conclusions and Outlook

In this final chapter we will bring together the results in the previous three chapters, which consisted of three distinct experiments all of which attempted to probe the small-scale particle dynamics of dense suspensions of silica.

We began the work by considering the repulsive interactions that control the onset of the formation of frictional contacts between suspended particles. We showed that these forces are strongly related to the onset of shear thickening, the point after which the viscosity begins to increase, by experimentally measuring the decrease in the onset stress with weakening electrostatic repulsion. The work discussed in chapter 4 shows experimentally rigorous evidence that a region exists where the onset stress of shear thickening in electrostatically stabilised suspensions scales as $\sigma^* \propto 1/R$. At the edge and beyond the region where we see normal shear thickening we note two different results. The first is a region where we see a strong size dependence on the scaling of σ^* with ionic strength, which we attribute to differences in the manufacturing, and therefore the surface characteristics of the smaller particles. The second result is at the edge of the shear thickening regime, where we see an apparent separation of the shear thickening region into two different shear thickening processes. We suggest that this separation is a result of the two shear thickening processes being controlled by different interparticle forces, those at short range and those at long range. As shown by the variation within our own results, rigor is necessary to extract meaningful data from large sets of shear thickening samples. Further work confirms the effect of the addition of ions on the shear thinning of sub-micron sized particles, due to the extended radius resulting from the interparticle

repulsive forces.

In our second chapter we expanded on previous work by Richards et al. [26], which proposed a model for shear rate oscillations in shear thickening suspensions alongside measurements for suspensions of cornstarch. Our results show that the model is capable of capturing the frequency of the oscillations for increasing apparent stresses and volume fractions in suspensions of silica. We found a characteristic strain $\gamma_0 = 0.110(5)$, measured from shear startup curves, and a relaxation time $t_r \approx 0.03\,\mathrm{s}$, measured by fitting to the frequency of the shear rate oscillations. We found that the thickening startup, where we measured the shear dependent transition between the low and high stress Newtonian plateaus of the $R = 2\,\mu\mathrm{m}$ silica particles suspended in G/W, can be fit by a double exponential with two characteristic strains $\gamma_0 = 0.110(5)$ and $\gamma_1 = 0.61(1)$. This is the first such result showing that the transition to the shear thickened state may be a result of two different shear dependent scales, suggesting that the shear thickening is a result of a two stage process. The two separate timescales may be related to the result of the previous chapter showing the separation of the shear thickening region into two separate shear thickening regions. These results together differ notably from previous work on cornstarch-in-water suspensions [26], suggesting that such timescales are strongly related the the particle properties and are not universal to dense suspensions.

Finally we have shown that boundary stress microscopy (BSM), a novel technique used to measure the local boundary stress of suspensions under shear, is highly sensitive to plate misalignment for rheometer setups using a small gap height $h \lesssim 200\,\mu\mathrm{m}$. We proposed a simple theoretical model of the plate misalignment in a cone-plate geometry for Newtonian and shear thickening suspensions, which can reasonably fit the unexpected divergence between the local and apparent stresses at various volume fractions. We show that measured boundary stress oscillations are often strongly coupled to the rheometer tool rotation, suggesting that the misalignment affects the behaviour of the suspension under shear. These results were found for suspensions which showed transient boundary stress fluctuations that are notably similar to previous results [27], suggesting such large fluctuations could be a result of misalignment of the rheometer tools and are therefore not necessarily found in shear thickening suspensions under simple shear. This final result raises questions about the validity of local stress measurements in shear thickening suspensions. As expected this shows that rigour is necessary when using novel methods to measured things that are hard to verify further.

Bibliography

[1] F. Boyer, É. Guazzelli, and O. Pouliquen, "Unifying suspension and granular rheology," Physical Review Letters, vol. 107, p. 188301, Oct 2011.

[2] C. Bonnoit, J. Lanuza, A. Lindner, and E. Clement, "Mesoscopic length scale controls the rheology of dense suspensions.," Physical review letters, vol. 105, p. 108302, Sep 2010.

[3] S. Dagois-Bohy, S. Hormozi, E. Guazzelli, and O. Pouliquen, "Rheology of dense suspensions of non-colloidal spheres in yield-stress fluids," Journal of Fluid Mechanics, vol. 776, p. R2, 2015.

[4] T. Dbouk, L. Lobry, and E. Lemaire, "Normal stresses in concentrated non-Brownian suspensions," Journal of Fluid Mechanics, vol. 715, p. 239–272, 2013.

[5] G. Ovarlez, F. Bertrand, and S. Rodts, "Local determination of the constitutive law of a dense suspension of noncolloidal particles through magnetic resonance imaging," Journal of Rheology, vol. 50, no. 3, pp. 259–292, 2006.

[6] I. E. Zarraga, D. A. Hill, and D. T. Leighton, "The characterization of the total stress of concentrated suspensions of noncolloidal spheres in Newtonian fluids," Journal of Rheology, vol. 44, no. 2, pp. 185–220, 2000.

[7] S. Gallier, E. Lemaire, F. Peters, and L. Lobry, "Rheology of sheared suspensions of rough frictional particles," Journal of Fluid Mechanics, vol. 757, p. 514–549, 2014.

[8] R. Mari, R. Seto, J. F. Morris, and M. M. Denn, "Shear thickening, frictionless and frictional rheologies in non-Brownian suspensions," Journal of Rheology, vol. 58, pp. 1693–1724, Nov 2014.

[9] A. Sierou and J. F. Brady, "Rheology and microstructure in concentrated noncolloidal suspensions," Journal of Rheology, vol. 46, no. 5, pp. 1031–1056, 2002.

[10] A. Einstein, "Eine neue bestimmung der moleküldimensionen," Annalen der Physik, vol. 324, no. 2, pp. 289–306, 1906.

[11] A. Einstein, "Berichtigung zu meiner arbeit: ,,eine neue bestimmung der moleküldimensionen"," Annalen der Physik, vol. 339, no. 3, pp. 591–592, 1911.

[12] G. K. Batchelor and J. T. Green, "The hydrodynamic interaction of two small freely- moving spheres in a linear flow field," Journal of Fluid Mechanics, vol. 56, no. 2, pp. 375–400, 1972.

[13] D. R. Foss and J. F. Brady, "Structure, diffusion and rheology of Brownian suspensions by Stokesian dynamics simulation," Journal of Fluid Mechanics, vol. 407, pp. 167–200, 2000.

[14] P. D'Haene, J. Mewis, and G. Fuller, "Scattering dichroism measurements of flow-induced structure of a shear thickening suspension," Journal of Colloid and Interface Science, vol. 156, pp. 350–358, Mar 1993.

[15] J. C. van der Werff and C. G. de Kruif, "Hard-sphere colloidal dispersions: The scaling of rheological properties with particle size, volume fraction, and shear rate," Journal of Rheology, vol. 33, pp. 421–454, Apr 1989.

[16] V. Valmacco, M. Elzbieciak-Wodka, D. Herman, G. Trefalt, P. Maroni, and M. Borkovec, "Forces between silica particles in the presence of multivalent cations," Journal of Colloid and Interface Science, vol. 472, pp. 108–115, Jun 2016.

[17] G. Petekidis, D. Vlassopoulos, and P. N. Pusey, "Yielding and flow of sheared colloidal glasses," Journal of Physics: Condensed Matter, vol. 16, pp. S3955–S3963, Sep 2004.

[18] S.-E. Phan, W. B. Russel, Z. Cheng, J. Zhu, P. M. Chaikin, J. H. Dunsmuir, and R. H. Ottewill, "Phase transition, equation of state, and limiting shear viscosities of hard sphere dispersions," Physical Review E, vol. 54, pp. 6633–6645, Dec 1996.

[19] W. J. Frith, P. d'Haene, R. Buscall, and J. Mewis, "Shear thickening in model suspensions of sterically stabilized particles," Journal of Rheology, vol. 40, pp. 531–548, Jul 1996.

[20] B. Guy, M. Hermes, and W. Poon, "Towards a unified description of the rheology of hard-particle suspensions," Physical Review Letters, vol. 115, p. 088304, Aug 2015.

[21] A. Singh, R. Mari, M. M. Denn, and J. F. Morris, "A constitutive model for simple shear of dense frictional suspensions," Journal of Rheology, vol. 62, pp. 457–468, Mar 2018.

[22] B. J. Maranzano and N. J. Wagner, "The effects of interparticle interactions and particle size on reversible shear thickening: Hard-sphere colloidal dispersions," Journal of Rheology, vol. 45, pp. 1205–1222, Sep 2001.

[23] A. Singh, S. Pednekar, J. Chun, M. M. Denn, and J. F. Morris, "From yielding to shear jamming in a cohesive frictional suspension," Physical Review Letters, vol. 122, p. 098004, Mar. 2019.

[24] R. Mari, R. Seto, J. F. Morris, M. M. Denn, J. F. Morris, and M. M. Denn, "Discontinuous shear thickening in Brownian suspensions by dynamic simulation," Proceedings of the National Academy of Sciences., vol. 112, no. 50, pp. 15326–15330, 2015.

[25] J. A. Richards, R. E. O'Neill, and W. C. K. Poon, "Turning a yield-stress calcite suspension into a shear-thickening one by tuning inter-particle friction," Rheologica acta, vol. 60, no. 2-3, pp. 97–106, 2021.

[26] J. Richards, J. Royer, B. Liebchen, B. Guy, and W. Poon, "Competing timescales lead to oscillations in shear-thickening suspensions," Physical Review Letters, vol. 123, p. 038004, Jul 2019.

[27] V. Rathee, D. L. Blair, and J. S. Urbach, "Localized stress fluctuations drive shear thickening in dense suspensions," Proceedings of the National Academy of Sciences, vol. 114, pp. 8740–8745, Aug 2017.

[28] G. Ovarlez, A. V. N. Le, W. J. Smit, A. Fall, R. Mari, G. Chatté, and A. Colin, "Density waves in shear-thickening suspensions," Science Advances, vol. 6, no. 16, p. 5589, 2020.

[29] P. F. G. Banfill, "The rheology of fresh cement and concrete-a review," in Proceedings of the 11th international cement chemistry congress, vol. 1, pp. 50–62, 2003.

[30] H. Van Damme, "Concrete material science: Past, present, and future innovations," Cement and Concrete Research, vol. 112, pp. 5–24, 2018.

[31] E. Blanco, D. J. M. Hodgson, M. Hermes, R. Besseling, G. L. Hunter, P. M. Chaikin, M. E. Cates, I. V. Damme, and W. C. K. Poon, "Conching chocolate is a prototypical transition from frictionally jammed solid to flowable suspension with maximal solid content," Proceedings of the National Academy of Sciences, vol. 116, no. 21, pp. 10303–10308, 2019.

[32] Z. Liu, L. Liu, H. Zhou, J. Wang, and L. Deng, "Toothpaste microstructure and rheological behaviors including aging and partial rejuvenation," Korea-Australia Rheology Journal, vol. 27, no. 3, pp. 207–212, 2015.

[33] H. A. Ardakani, E. Mitsoulis, and S. G. Hatzikiriakos, "Thixotropic flow of toothpaste through extrusion dies," Journal of Non-Newtonian Fluid Mechanics, vol. 166, no. 21, pp. 1262–1271, 2011.

[34] E. Guazzelli, J. F. Morris, and S. Pic, A Physical Introduction to Suspension Dynamics. Cambridge Texts in Applied Mathematics, Cambridge University Press, 2011.

[35] I. M. Krieger, "Rheology of monodisperse latices," Advances in Colloid and Interface Science, vol. 3, no. 2, pp. 111–136, 1972.

[36] V. Vand, "Viscosity of solutions and suspensions. i. theory," Journal of Physical Chemistry, vol. 52, pp. 277–299, Feb. 1948.

[37] S. H. Maron and P. E. Pierce, "Application of Ree-Eyring generalized flow theory to suspensions of spherical particles," Journal of Colloid Science, vol. 11, pp. 80–95, Feb 1956.

[38] W. van Megen, "Crystallisation and the glass transition in suspensions of hard colloidal spheres," Transport Theory and Statistical Physics, vol. 24, no. 6-8, pp. 1017–1051, 1995.

[39] W. van Megen and S. M. Underwood, "Glass transition in colloidal hard spheres: Measurement and mode-coupling-theory analysis of the coherent intermediate scattering function," Physical Review E, vol. 49, pp. 4206–4220, May 1994.

[40] W. van Megen, T. C. Mortensen, S. R. Williams, and J. Müller, "Measurement of the self-intermediate scattering function of suspensions of hard spherical particles near the glass transition," Physical Review E, vol. 58, pp. 6073–6085, Nov 1998.

[41] R. Besseling, E. R. Weeks, A. B. Schofield, and W. C. K. Poon, "Three-dimensional imaging of colloidal glasses under steady shear," Physical Review Letters, vol. 99, p. 028301, Jul 2007.

[42] C. P. Royall, W. C. K. Poon, and E. R. Weeks, "In search of colloidal hard spheres," Soft Matter, vol. 9, pp. 17–27, 2013.

[43] J. Israelachvili, "Intermolecular and surface forces," in Intermolecular and Surface Forces (Third Edition) (J. N. Israelachvili, ed.), p. iii, Boston: Academic Press, third edition ed., 2011.

[44] W. Wang, W. Gu, and K. Liu, "Force chain evolution and force characteristics of shearing granular media in taylor-couette geometry by DEM," Tribology Transactions, vol. 58, pp. 197–206, Dec. 2014.

[45] M. Dishon, O. Zohar, and U. Sivan, "From repulsion to attraction and back to repulsion: The effect of NaCl, KCl, and CsCl on the force between silica surfaces in aqueous solution," Langmuir, vol. 25, pp. 2831–2836, Mar. 2009.

[46] W. B. Russel, D. A. Saville, and W. R. Schowalter, Colloidal Dispersions. Cambridge Monographs on Mechanics, Cambridge University Press, 1989.

[47] N. M. James, E. Han, R. A. L. de la Cruz, J. Jureller, and H. M. Jaeger, "Interparticle hydrogen bonding can elicit shear jamming in dense suspensions," Nature Materials, vol. 17, no. 11, pp. 965–970, 2018.

[48] A. Carré, V. Lacarrière, and W. Birch, "Molecular interactions between DNA and an aminated glass substrate," Journal of Colloid and Interface Science, vol. 260, no. 1, pp. 49–55, 2003.

[49] J.-P. Cloarec, C. Chevalier, J. Genest, J. Beauvais, H. Chamas, Y. Chevolot, T. Baron, and A. Souifi, "pH driven addressing of silicon nanowires onto si_3n_4/sio_2 micro-patterned surfaces," Nanotechnology, vol. 27, p. 295602, Jun 2016.

[50] G. Trefalt, S. H. Behrens, and M. Borkovec, "Charge regulation in the electrical double layer: Ion adsorption and surface interactions," Langmuir, vol. 32, pp. 380–400, Jan. 2016.

[51] R. Pericet-Camara, G. Papastavrou, S. H. Behrens, and M. Borkovec, "Interaction between charged surfaces on the Poisson-Boltzmann level: The constant regulation approximation," Journal of Physical Chemistry B, vol. 108, pp. 19467–19475, Dec. 2004.

[52] G. Trefalt, I. Szilagyi, and M. Borkovec, "Poisson–Boltzmann description of interaction forces and aggregation rates involving charged colloidal particles in asymmetric electrolytes," Journal of Colloid and Interface Science, vol. 406, pp. 111–120, 2013.

[53] S. H. Behrens and M. Borkovec, "Electrostatic interaction of colloidal surfaces with variable charge," Journal of Physical Chemistry B, vol. 103, pp. 2918–2928, Apr. 1999.

[54] W. A. Ducker, T. J. Senden, and R. M. Pashley, "Measurement of forces in liquids using a force microscope," Langmuir, vol. 8, pp. 1831–1836, July 1992.

[55] G. R. Wiese, R. O. James, and T. W. Healy, "Discreteness of charge and solvation effects in cation adsorption at the oxide/water interface," Discussions of The Faraday Society, vol. 52, pp. 302–311, 1971.

[56] R. Horn, D. Smith, and W. Haller, "Surface forces and viscosity of water measured between silica sheets," Chemical Physics Letters, vol. 162, no. 4, pp. 404–408, 1989.

[57] G. Vigil, Z. Xu, S. Steinberg, and J. Israelachvili, "Interactions of silica surfaces," Journal of Colloid and Interface Science, vol. 165, no. 2, pp. 367–385, 1994.

[58] S. M. Acuña and P. G. Toledo, "Nanoscale repulsive forces between mica and silica surfaces in aqueous solutions," Journal of Colloid and Interface Science, vol. 361, no. 1, pp. 397–399, 2011.

[59] J. J. Valle-Delgado, J. A. Molina-Bolívar, F. Galisteo-González, M. J. Gálvez-Ruiz, A. Feiler, and M. W. Rutland, "Hydration forces between silica surfaces: Experimental data and predictions from different theories," The Journal of Chemical Physics, vol. 123, no. 3, p. 034708, 2005.

[60] A. Grabbe and R. G. Horn, "Double-layer and hydration forces measured between silica sheets subjected to various surface treatments," Journal of Colloid and Interface Science, vol. 157, no. 2, pp. 375–383, 1993.

[61] M. Kobayashi, F. Juillerat, P. Galletto, P. Bowen, and M. Borkovec, "Aggregation and charging of colloidal silica particles: Effect of particle size," Langmuir, vol. 21, no. 13, pp. 5761–5769, 2005. PMID: 15952820.

[62] J. F. Morris, "Lubricated-to-frictional shear thickening scenario in dense suspensions," Physical Review Fluids, vol. 3, p. 110508, Nov 2018.

[63] M. Hermes, B. M. Guy, W. C. K. Poon, G. Poy, M. E. Cates, and M. Wyart, "Unsteady flow and particle migration in dense, non-Brownian suspensions," Journal of Rheology, vol. 60, pp. 905–916, Sep 2016.

[64] R. E. O'Neill, J. R. Royer, and W. C. K. Poon, "Liquid migration in shear thickening suspensions flowing through constrictions," Physical Review Letters, vol. 123, p. 128002, Sep 2019.

[65] M. Wyart and M. Cates, "Discontinuous shear thickening without inertia in dense non-Brownian suspensions," Physical Review Letters, vol. 112, p. 098302, Mar 2014.

[66] L. E. Silbert, D. Ertaş, G. S. Grest, T. C. Halsey, and D. Levine, "Geometry of frictionless and frictional sphere packings," Physical Review E, vol. 65, p. 031304, Feb 2002.

[67] L. E. Silbert, "Jamming of frictional spheres and random loose packing," Soft Matter, vol. 6, pp. 2918–2924, 2010.

[68] J. R. Royer, D. L. Blair, and S. D. Hudson, "Rheological signature of frictional interactions in shear thickening suspensions," Physical Review Letters, vol. 116, p. 188301, May 2016.

[69] R. Radhakrishnan, J. R. Royer, W. C. K. Poon, and J. Sun, "Force chains and networks: wet suspensions through dry granular eyes," Granular Matter, vol. 22, no. 1, p. 29, 2020.

[70] D. Hodgson, Particulate Granulation and Rheology: Towards a Unifying Perspective. PhD thesis, University of Edinburgh, 2016.

[71] S. Cao, Y. Wang, H. Pang, J. Zhang, Y. Wu, S. Xuan, and X. Gong, "Shear jamming onset in dense granular suspensions," Journal of Rheology, vol. 65, pp. 419–426, May 2021.

[72] G. Bossis, P. Boustingorry, Y. Grasselli, A. Meunier, R. Morini, A. Zubarev, and O. Volkova, "Discontinuous shear thickening in the presence of polymers adsorbed on the surface of calcium carbonate particles," Rheologica Acta, vol. 56, pp. 415–430, Mar 2017.

[73] A. S. Baumgarten and K. Kamrin, "A general constitutive model for dense, fine-particle suspensions validated in many geometries," Proceedings of the National Academy of Sciences, vol. 116, no. 42, pp. 20828–20836, 2019.

[74] E. Han, N. M. James, and H. M. Jaeger, "Stress controlled rheology of dense suspensions using transient flows," Physical Review Letters, vol. 123, p. 248002, Dec 2019.

[75] V. Rathee, D. L. Blair, and J. S. Urbach, "Localized transient jamming in discontinuous shear thickening," Journal of Rheology, vol. 64, no. 2, pp. 299–308, 2020.

[76] V. Rathee, J. Miller, D. L. Blair, and J. S. Urbach, "Structure of propagating high-stress fronts in a shear-thickening suspension," Proceedings of the National Academy of Sciences, vol. 119, Aug 2022.

[77] R. J. Larsen, J.-W. Kim, C. F. Zukoski, and D. A. Weitz, "Fluctuations in flow produced by competition between apparent wall slip and dilatancy," Rheologica Acta, vol. 53, pp. 333–347, Mar. 2014.

[78] S. Nagahiro, H. Nakanishi, and N. Mitarai, "Experimental observation of shear thickening oscillation," Europhysics Letters (EPL), vol. 104, p. 28002, Oct 2013.

[79] R. Maharjan and E. Brown, "Giant deviation of a relaxation time from generalized Newtonian theory in discontinuous shear thickening suspensions," Physical Review Fluids, vol. 2, p. 123301, Dec 2017.

[80] M. E. Cates and M. Wyart, "Granulation and bistability in non-Brownian suspensions," Rheologica Acta, vol. 53, pp. 755–764, Aug 2014.

[81] S. Jamali and J. Brady, "Alternative frictional model for discontinuous shear thickening of dense suspensions: Hydrodynamics," Physical Review Letters, vol. 123, p. 138002, Sep 2019.

[82] S. Jamali, E. D. Gado, and J. F. Morris, "Rheology discussions: The physics of dense suspensions," Journal of Rheology, vol. 64, pp. 1501–1524, Nov 2020.

[83] M. Wang, S. Jamali, and J. F. Brady, "A hydrodynamic model for discontinuous shear-thickening in dense suspensions," Journal of Rheology, vol. 64, no. 2, pp. 379–394, 2020.

[84] R. Seto, R. Mari, J. F. Morris, and M. M. Denn, "Discontinuous shear thickening of frictional hard-sphere suspensions," Physical Review Letters, vol. 111, p. 218301, Nov 2013.

[85] T. Kawasaki and L. Berthier, "Discontinuous shear thickening in Brownian suspensions," Physical Review E, vol. 98, p. 012609, Jul 2018.

[86] N. Y. Lin, B. M. Guy, M. Hermes, C. Ness, J. Sun, W. C. Poon, and I. Cohen, "Hydrodynamic and contact contributions to continuous shear thickening in colloidal suspensions," Physical Review Letters, vol. 115, p. 228304, Nov 2015.

[87] J. R. Melrose and R. C. Ball, "The pathological behaviour of sheared hard spheres with hydrodynamic interactions," Europhysics Letters (EPL), vol. 32, pp. 535–540, Nov 1995.

[88] M. Wang and J. F. Brady, "Constant stress and pressure rheology of colloidal suspensions," Physical Review Letters, vol. 115, p. 158301, Oct 2015.

[89] E. Brown, N. A. Forman, C. S. Orellana, H. Zhang, B. W. Maynor, D. E. Betts, J. M. DeSimone, and H. M. Jaeger, "Generality of shear thickening in dense suspensions," Nature Materials, vol. 9, pp. 220–224, Jan 2010.

[90] J. A. Richards, B. M. Guy, E. Blanco, M. Hermes, G. Poy, and W. C. K. Poon, "The role of friction in the yielding of adhesive non-Brownian suspensions," Journal of Rheology, vol. 64, pp. 405–412, Mar 2020.

[91] B. Guy, J. Richards, D. Hodgson, E. Blanco, and W. Poon, "Constraint-based approach to granular dispersion rheology," Physical Review Letters, vol. 121, p. 128001, Sep 2018.

[92] G. Chatté, J. Comtet, A. Niguès, L. Bocquet, A. Siria, G. Ducouret, F. Lequeux, N. Lenoir, G. Ovarlez, and A. Colin, "Shear thinning in non-Brownian suspensions," Soft Matter, vol. 14, pp. 879–893, 2018.

[93] A. Papadopoulou, J. J. Gillissen, H. J. Wilson, M. K. Tiwari, and S. Balabani, "On the shear thinning of non-Brownian suspensions: Friction or adhesion?," Journal of Non-Newtonian Fluid Mechanics, vol. 281, Jul 2020. 9th International Meeting of the Hellenic-Society-of-Rheology (HSR), Samos, Greece, Jun 23-27, 2019.

[94] C. Beck, W. Härtl, and R. Hempelmann, "The glass transition of charged and hard sphere silica colloids," The Journal of Chemical Physics, vol. 111, pp. 8209–8213, Nov 1999.

[95] V. Rathee, S. Arora, D. L. Blair, J. S. Urbach, A. K. Sood, and R. Ganapathy, "Role of particle orientational order during shear thickening in suspensions of colloidal rods," Physical Review E, vol. 101, p. 040601(R), Apr 2020.

[96] G. Bossis, Y. Grasselli, A. Meunier, and O. Volkova, "Tunable discontinuous shear thickening with magnetorheological suspensions," Journal of Intelligent Material Systems and Structures, vol. 29, pp. 5–11, Apr 2017.

[97] S. Barik and S. Majumdar, "Origin of two distinct stress relaxation regimes in shear jammed dense suspensions," Physical Review Letters, vol. 128, p. 258002, Jun 2022.

[98] A. Gauthier, M. Pruvost, O. Gamache, and A. Colin, "A new pressure sensor array for normal stress measurement in complex fluids," Journal of Rheology, vol. 65, pp. 583–594, Jul 2021.

[99] M. E. Cates, J. P. Wittmer, J.-P. Bouchaud, and P. Claudin, "Jamming, force chains, and fragile matter," Physical Review Letters, vol. 81, pp. 1841–1844, Aug 1998.

[100] M. A. Bevan and D. C. Prieve, "Hindered diffusion of colloidal particles very near to a wall: Revisited," The Journal of Chemical Physics, vol. 113, pp. 1228–1236, 07 2000.

[101] W. C. K. Poon, E. R. Weeks, and C. P. Royall, "On measuring colloidal volume fractions," Soft Matter, vol. 8, pp. 21–30, 2012.

[102] D. J. Dudgeon and L. E. Wedgewood, "Flow in the misaligned cone-and-plate rheometer," Journal of Non-Newtonian Fluid Mechanics, vol. 48, no. 1, pp. 21–48, 1993.

[103] B. J. Maranzano and N. J. Wagner, "The effects of particle size on reversible shear thickening of concentrated colloidal dispersions," The Journal of Chemical Physics, vol. 114, pp. 10514–10527, Jun 2001.

[104] B. M. Guy, C. Ness, M. Hermes, L. J. Sawiak, J. Sun, and W. C. K. Poon, "Testing the Wyart–Cates model for non-Brownian shear thickening using bidisperse suspensions," Soft Matter, vol. 16, no. 1, pp. 229–237, 2020.

[105] A. Singh, C. Ness, R. Seto, J. J. de Pablo, and H. M. Jaeger, "Shear thickening and jamming of dense suspensions: The "roll" of friction," Physical Review Letters, vol. 124, p. 248005, Jun 18 2020.

[106] V. Gopalakrishnan and C. F. Zukoski, "Effect of attractions on shear thickening in dense suspensions," Journal of Rheology, vol. 48, pp. 1321–1344, Nov 2004.

[107] L.-N. Krishnamurthy, N. J. Wagner, and J. Mewis, "Shear thickening in polymer stabilized colloidal dispersions," Journal of Rheology, vol. 49, pp. 1347–1360, Nov 2005.

[108] J. Kaldasch and B. Senge, "Shear thickening in polymer stabilized colloidal suspensions," Colloid and Polymer Science, vol. 287, pp. 1481–1485, Oct 2009.

[109] J. M. Monti, P. M. McGuiggan, and M. O. Robbins, "Effect of roughness and elasticity on interactions between charged colloidal spheres," Langmuir, vol. 35, pp. 15948–15959, Dec 3 2019.

[110] R. Mari, R. Seto, J. F. Morris, and M. M. Denn, "Nonmonotonic flow curves of shear thickening suspensions," Physical Review E, vol. 91, p. 052302, May 2015.

[111] H. Nakamura, S. Makino, and M. Ishii, "Continuous shear thickening and discontinuous shear thickening of concentrated monodispersed silica slurry," Advanced Powder Technology, vol. 31, no. 4, pp. 1659–1664, 2020.

[112] R. Cross, "Elastic and viscous properties of silly putty," American Journal of Physics, vol. 80, no. 10, pp. 870–875, 2012.

[113] C. Ness and J. Sun, "Two-scale evolution during shear reversal in dense suspensions," Physical Review E, vol. 93, Jan 8 2016.

[114] V. G. Kolli, E. J. Pollauf, and F. Gadala-Maria, "Transient normal stress response in a concentrated suspension of spherical particles," Journal of Rheology, vol. 46, no. 1, pp. 321–334, 2002.

[115] D. Lootens, H. V. Damme, and P. Hébraud, "Giant stress fluctuations at the jamming transition," Physical Review Letters, vol. 90, p. 178301, Apr 2003.

[116] T. Hatano, "Growing length and time scales in a suspension of athermal particles," Physical Review E, vol. 79, p. 050301, May 2009.

[117] A. Ikeda, T. Kawasaki, L. Berthier, K. Saitoh, and T. Hatano, "Universal relaxation dynamics of sphere packings below jamming," Physical Review Letters, vol. 124, p. 058001, Feb 2020.

[118] R. W. Style, R. Boltyanskiy, G. K. German, C. Hyland, C. W. MacMinn, A. F. Mertz, L. A. Wilen, Y. Xu, and E. R. Dufresne, "Traction force microscopy in physics and biology," Soft Matter, vol. 10, no. 23, p. 4047, 2014.

[119] R. C. Arevalo, P. Kumar, J. S. Urbach, and D. L. Blair, "Stress heterogeneities in sheared type-i collagen networks revealed by boundary stress microscopy," Plos One, vol. 10, p. e0118021, Mar 2015.

[120] A. Liberzon, T. Käufer, A. Bauer, P. Vennemann, and E. Zimmer, "Openpiv/openpiv-python: Openpiv-python v0.23.6," 2021.

[121] J. H. Cho, A. H. Griese, I. R. Peters, and I. Bischofberger, "Lasting effects of discontinuous shear thickening in cornstarch suspensions upon flow cessation," Physical Review of Fluids, vol. 7, p. 063302, Jun 2022.

[122] V. Studer, G. Hang, A. Pandolfi, M. Ortiz, W. French Anderson, and S. R. Quake, "Scaling properties of a low-actuation pressure microfluidic valve," Journal of Applied Physics, vol. 95, no. 1, pp. 393–398, 2004.

[123] P. Du, I.-K. Lin, H. Lu, and X. Zhang, "Extension of the beam theory for polymer bio-transducers with low aspect ratios and viscoelastic characteristics," Journal of Micromechanics and Microengineering, vol. 20, no. 9, p. 095016, 2010.

[124] A. Folch, Introduction to BioMEMS. CRC Press, Apr 2016.

[125] J. E. Mark, Polymer data handbook. Oxford University Press, 2009.

[126] D. W. Inglis, "A method for reducing pressure-induced deformation in silicone microfluidics," Biomicrofluidics, vol. 4, no. 2, p. 026504, 2010.

[127] J. C. del Álamo, R. Meili, B. Alonso-Latorre, J. Rodríguez-Rodríguez, A. Aliseda, R. A. Firtel, and J. C. Lasheras, "Spatio-temporal analysis of eukaryotic cell motility by improved force cytometry," Proceedings of the National Academy of Sciences, vol. 104, no. 33, pp. 13343–13348, 2007.

[128] C. J. Pipe, T. S. Majmudar, and G. H. McKinley, "High shear rate viscometry," Rheologica Acta, vol. 47, no. 5, pp. 621–642, 2008.

[129] B. Zhou, S. Drusch, and S. A. Hogan, "Confined flow behavior under high shear rates and stability of oil/water high internal phase emulsions (hipes) stabilized by whey protein isolate: Role of protein concentration and ph," Food Research International, vol. 160, Oct 2022.

[130] S. S. Vadodaria, A. J. Onyianta, and D. Sun, "High-shear rate rheometry of micro-nanofibrillated cellulose (cmf/cnf) suspensions using rotational rheometer," Cellulose, vol. 25, pp. 5535–5552, Oct 2018.

[131] E. Guyon, J.-P. Hulin, L. Petit, and C. D. Mitescu, Physical Hydrodynamics. Oxford University Press, 01 2015.